

UNIVERSITY OF CALIFORNIA
RIVERSIDE

Search for Ultrahigh-Energy Gamma Rays
from Fast Pulsars

A Dissertation submitted in partial satisfaction
of the requirements for the degree of

Doctor of Philosophy

in

Physics

by

Jui-Pin Wu

December, 1995

Dissertation Committee:

Allen D. Zych, Chairperson

Benjamin C. Shen

O. Tümay Tümer

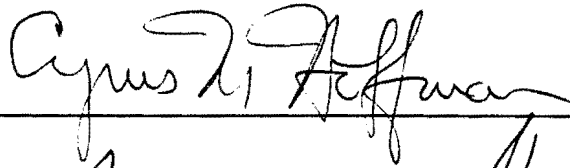
Cyrus M. Hoffman

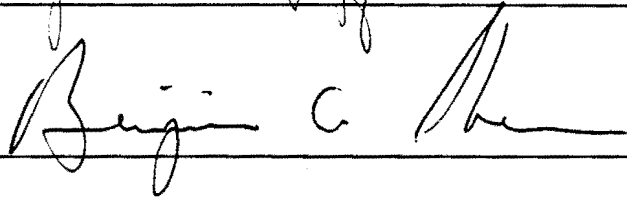
©Copyright by

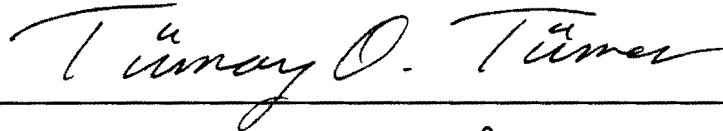
Jui-Pin Wu

1995

The Dissertation of Jui-Pin Wu is approved:


Cyrus H. Hoffman


Benjamin C. Chen


Tümay O. Tümer


Allen Zych

Committee Chairperson

University of California, Riverside

Dedicated
to
My Parents
Ta-Lu and Chang-Huan Wu
and
My Wife
Ching-Chiang Mai

Acknowledgement

I have enjoyed being a graduate student in the Physics Department of the University of California at Riverside for these years. I am so grateful to have Professor Allen D. Zych be my dissertation advisor. His enthusiastic guidance, encouragement and support make my life working in IGPP a great one.

I would also like to express my thanks to Dr. O. Tümay Tümer. He gave me the opportunity to go to Los Alamos National Laboratory and to collaborate with excellent people there, and he is constantly showing his concern to me.

I thank Dr. White for being part of the oral committee of presenting my thesis title.

I would also like to thank Dr. Shen for being part of my oral defense committee.

Many thanks go to Dr. Cyrus Hoffman. His kind, caring and humorous attitude makes me feel joyful at the work and after the work. He is also like a father to me, especially under the condition of that my families are half of the earth away from me.

Over nearly four years staying in Los Alamos, the people there are not only working colleagues but also great friends. They helped and taught me the things in the experiment that I had never touched. The assistance from Todd Haines, Gus Sinnis, Gerry Dion, Dimitris Alexandreas, Steve Biller and Dave Williams is a continuous source to know about the experiment and Astrophysics. Thank you all.

The graduate students, including Tom Yang, Glenn Allen, Cindy Dion, Pam Chumney, and Richard Schnee are great companions for the lonely life in Los

Alamos. I will always remember the party time at Glenn's or Pam's home and the pool-shooting with Tom in the bar.

I would like to express my gratitude to Scott DeLay who brought me into the Indian culture and help me understand New Mexico. He always gives me a hand when I have problem of trouble-shooting the hardware. I will also miss his colorful Halloween party.

I have enjoyed working with all the CYGNUS people from the first day I went to Los Alamos. Thank you all for the opportunity for me to learn the Astrophysics from you.

Kuan-Wen Chuang, Gung Yur, Wayne Lo, Tom Tu, and all other old Chinese friends have made UCR a pleasant place to stay. It has always been delightful to talk and be with you.

I would like to express my special thanks to Professor Nai-Li Liu. She has always been concerning and helping the Chinese students in all respects in the Physics Department.

Although I have not been with the IGPP researchers, post doctors and graduate students, including, but not limit to, Terry, Zak, Dipen, Dave, Aysün, Jim, Gary and Scott, for a long time, but it has been my pleasure to be working with you for these months.

Special thanks go to the IGPP staff Leslie, Bernice, Patti and Nancy for their continuous help, even when I was in Los Alamos.

I thank Linda O'Neill for her academic assistance over these years I have been in UCR.

The last, but not the least, I would like to thank my parents for their

continuing support and concern and my wife for her forgiving that I can't always stay by her side. Without you, I would not have been possible to finish my study in a foreign country. I love you.

ABSTRACT OF THE DISSERTATION

Search for Ultrahigh-Energy Gamma Rays from Fast Pulsars

by

Jui-Pin Wu

Doctor of Philosophy, Graduate Program in Physics

University of California, Riverside, December, 1995

Professor Allen D. Zych, Chairperson

The data collected from the CYGNUS-I scintillator array and from the JASA water-Cherenkov array of the CYGNUS extensive air-shower experiment are searched for the emission of ultrahigh-energy gamma rays from the directions of the Crab, PSR 137+21, PSR 151+32, PSR 153+29 and PSR 157+20. For the unpulsed searches, the CYGNUS-I data spans the period from 1986 April 2 to 1994 March 7, and the JASA data covers the period from 1992 October 23 through 1993 October 23. For the pulsed searches, the CYGNUS-I data spans the period from 1991 February 27 to 1994 March 7, while the JASA data cover the same period of time as that for the unpulsed search. Each dataset is divided into two categories; one of them contains all events without any cuts and the other only contains events without observed muons. Both datasets are examined for long-term steady and pulsed emissions and single-day unpulsed and pulsed emissions.

No evidence of statistically significant excesses above the expected cosmic-

ray background for unpulsed emissions are found from any of the sources examined. Upper limits for the steady flux are quoted at the 90% confidence level above 100 TeV. The steady flux upper limits from the CYGNUS-I all-event (muon-poor) results are 3.0 (2.2), 2.6 (1.5), 1.3 (1.2), 1.4 (0.9), and $3.2 (2.4) \times 10^{-14}$ photons $\text{cm}^{-2} \text{s}^{-1}$ for the Crab, PSR 1937+21, PSR 1951+32, PSR 1953+29, and PSR 1957+20, respectively. Also, no sporadic single-day emissions are found from any of the sources.

The Z_5^2 test is used for the Crab to test the uniformity of the data against periodic signals, while the others are tested by the Z_{10}^2 test. Long-term pulsed emissions are not seen in any of the data searched. Pulsed analysis on single source days with 2σ or more excess observed in the unpulsed daily search also shows no compelling results.

Contents

Dedication	iv
Acknowledgement	v
Abstract	viii
List of Tables	xiii
List of Figures	xv
1 Introduction	1
1.1 Very High-Energy/Ultrahigh-Energy Astrophysics	1
1.2 Detection Techniques for VHE/UHE Cosmic Rays and Gamma Rays	2
1.3 Historical VHE/UHE Surveys	6
2 Pulsar Physics	10
2.1 Overview	10
2.2 Neutron Stars	12
2.3 Periods of Pulsars	13
2.4 Binary Pulsars and Millisecond Pulsars	15
2.4.1 The Crab Nebula and Pulsar PSR 0531+21	17

2.4.2	PSR 1937+21	21
2.4.3	PSR 1951+32	24
2.4.4	PSR 1953+29	27
2.4.5	PSR 1957+20	30
2.5	Theoretical Models	34
2.5.1	Outer Magnetospheric Gap Model	35
3	The CYGNUS Experiment	39
3.1	Introduction	39
3.2	The Scintillation EAS Array	41
3.3	Data Acquisition System	43
3.4	Calibration	47
3.5	Muon Detectors	49
3.6	Shower Reconstruction	51
4	JASA Water-Čerenkov Array	55
4.1	Installation	56
4.2	Water Purification	56
4.3	Detection of Shower Particles	59
4.4	Electronics	62
4.5	Calibration	62
4.6	Curvature and Sampling Corrections	64
4.7	Shower Reconstruction	65
4.8	Angular Resolution	65
4.9	Pool Simulation	65

5	Techniques of Searching for Directional Excess	69
5.1	Optimal Bin Size	69
5.2	Background Estimation	70
5.3	Significance Assessment	71
5.4	Flux Upper Limit	72
5.5	Timing Analyses	73
5.5.1	Solar-System Barycentering Correction	74
5.5.2	Pulse Arrival-Time Correction for Binaries	75
5.6	Epoch Folding	76
5.6.1	Phase Calculation	76
5.6.2	Rayleigh Test	76
5.6.3	Z_n^2 Test	77
5.7	Combination of Probabilities	78
6	Searches and Results	80
6.1	Data Selection	80
6.2	Analysis	81
6.3	Search for Unpulsed Emission	82
6.4	Search for Pulsed Emission	111
6.5	Summary	129
	Bibliography	134
A	Čerenkov Radiation	142
A.1	Čerenkov Effect	142
A.2	Characteristics	145

List of Tables

2.1	Summary of the steady flux from the Crab.	18
2.2	Results on pulsed emission of VHE/UHE γ -rays from the Crab pulsar.	20
2.3	Parameters of the Crab pulsar.	21
2.4	Timing parameters of PSR 1937+21.	23
2.5	Timing parameters of PSR 1951+32.	25
2.6	Timing parameters of the binary pulsar PSR 1953+29.	29
2.7	Timing parameters of the eclipsing binary PSR 1957+20.	32
3.1	Summary of the CYGNUS experiment.	44
3.2	Parameterizations of the showerfront curvature correction.	53
3.3	Parameterizations of the showerfront thickness.	54
5.1	Optimal bin radii for various tests.	70
6.1	Results of searching for long-term unpulsed emission in the CYGNUS-I data.	84
6.2	Results of searching for long-term unpulsed emission in the JASA data.	85

6.3	Results of searching for episodic emission over a time scale of one source day using the CYGNUS-I dataset.	89
6.4	Results of searching for episodic emission over a time scale of one source day using the JASA dataset.	90
6.5	Results of searching for long-term pulsed emission using the CYGNUS-I dataset.	115
6.6	Results of searching for long-term pulsed emission using the JASA dataset.	116
6.7	Results of searching for the single-day pulsed emission for the most significant day using the CYGNUS-I dataset.	127
6.8	Results of searching for the single-day pulsed emission for the most significant day using the JASA dataset.	128

List of Figures

1.1	Illustration of a proton-induced extensive air shower.	4
1.2	Typical ultrahigh-energy detector and extensive air shower.	7
1.3	Observations of Hercules X-1 at a blue-shifted frequency by 4 groups in 1986	9
2.1	A model of a radio pulsar as a strong magnetized neutron star, showing regions of radio emission generation.	11
2.2	Typical cross section of a neutron star.	12
2.3	Distribution of periods and period derivatives for 468 pulsars. . . .	14
2.4	Pulse profiles for PSR 1937+21.	22
2.5	The integrated profiles from PSR 1951+32.	26
2.6	Average pulse profiles of PSR 1953+29.	28
2.7	Orbital velocity curve of PSR 1957+20.	31
2.8	Integrated Profile of PSR 1957+20 at 430 MHz.	33
2.9	Schematic representation of the TeV emission region for γ -rays. . .	37
2.10	Magnetospheres of a spinning neutron star with an aligned magnetic dipole field and a more rapidly spinning conducting disk.	38
3.1	Current configuration of the CYGNUS experiment.	40

3.2	Schematic view of a CYGNUS scintillation counter.	42
3.3	Simplified diagram of the data acquisition system.	45
3.4	Sample ADC and TDC histograms.	48
3.5	A side view of the CYGNUS E-225 muon detector.	50
4.1	Schematic diagram of a water-Čerenkov detector and the arrange- ment of the PMTs.	57
4.2	A sample test result of the attenuation length vs. photon wavelength for the water of the Center pool.	60
4.3	PMT multiplicity spectrum for pools.	61
4.4	Simplified layout of the pool electronics system.	63
4.5	The PE lateral distributions from Monte Carlo simulations and the real data, after the performance of each PMT is lowered by about half.	68
5.1	Range of probabilities bounded by the product of two probabilities P_1 and P_2	79
6.1	Measured steady fluxes and upper limits for the Crab.	87
6.2	Distributions of (a) daily sigmas and (b) daily background counts from the Crab using all events in the CYGNUS-I dataset.	91
6.3	Distributions of (a) daily sigmas and (b) daily background counts from the Crab using μ -poor events in the CYGNUS-I dataset. . . .	92
6.4	Distributions of (a) daily sigmas and (b) daily background counts from the Crab using all events in the JASA dataset.	93

6.5	Distributions of (a) daily sigmas and (b) daily background counts from the Crab using μ -poor events in the JASA dataset.	94
6.6	Distributions of (a) daily sigmas and (b) daily background counts from PSR 1937+21 using all events in the CYGNUS-I dataset.	95
6.7	Distributions of (a) daily sigmas and (b) daily background counts from PSR 1937+21 using μ -poor events in the CYGNUS-I dataset.	96
6.8	Distributions of (a) daily sigmas and (b) daily background counts from PSR 1937+21 using all events in the JASA dataset.	97
6.9	Distributions of (a) daily sigmas and (b) daily background counts from PSR 1937+21 using μ -poor events in the JASA dataset.	98
6.10	Distributions of (a) daily sigmas and (b) daily background counts from PSR 1951+32 using all events in the CYGNUS-I dataset.	99
6.11	Distributions of (a) daily sigmas and (b) daily background counts from PSR 1951+32 using μ -poor events in the CYGNUS-I dataset.	100
6.12	Distributions of (a) daily sigmas and (b) daily background counts from PSR 1951+32 using all events in the JASA dataset.	101
6.13	Distributions of (a) daily sigmas and (b) daily background counts from PSR 1951+32 using μ -poor events in the JASA dataset.	102
6.14	Distributions of (a) daily sigmas and (b) daily background counts from PSR 1953+29 using all events in the CYGNUS-I dataset.	103
6.15	Distributions of (a) daily sigmas and (b) daily background counts from PSR 1953+29 using μ -poor events in the CYGNUS-I dataset.	104
6.16	Distributions of (a) daily sigmas and (b) daily background counts from PSR 1953+29 using all events in the JASA dataset.	105

6.17	Distributions of (a) daily sigmas and (b) daily background counts from PSR 1953+29 using μ -poor events in the JASA dataset.	106
6.18	Distributions of daily sigmas and daily background counts from PSR 1957+20 using all events in the CYGNUS-I dataset.	107
6.19	Distributions of (a) daily sigmas and (b) daily background counts from PSR 1957+20 using μ -poor events in the CYGNUS-I dataset.	108
6.20	Distributions of (a) daily sigmas and (b) daily background counts from PSR 1957+20 using all events in the JASA dataset.	109
6.21	Distributions of (a) daily sigmas and (b) daily background counts from PSR 1957+20 using μ -poor events in the JASA dataset.	110
6.22	The Crab pulsar phasograms for long-term pulsed emission search using the CYGNUS-I dataset.	117
6.23	The Crab pulsar phasograms for long-term pulsed emission search using the JASA dataset.	118
6.24	PSR 1937+21 phasograms for long-term pulsed emission search us- ing the CYGNUS-I dataset.	119
6.25	PSR 1937+21 phasograms for long-term pulsed emission search us- ing the JASA dataset.	120
6.26	PSR 1951+32 phasograms for long-term pulsed emission search us- ing the CYGNUS-I dataset.	121
6.27	PSR 1951+32 phasograms for long-term pulsed emission search us- ing the JASA dataset.	122
6.28	PSR 1953+29 phasograms for long-term pulsed emission search us- ing the CYGNUS-I dataset.	123

6.29 PSR 1953+29 phasograms for long-term pulsed emission search using the JASA dataset.	124
6.30 PSR 1957+20 phasograms for long-term pulsed emission search using the CYGNUS-I dataset.	125
6.31 PSR 1957+20 phasograms for long-term pulsed emission search using the JASA dataset.	126
A.1 The polarization induced by the passage of a charged particle. . . .	143
A.2 Čerenkov radiation.	144

Chapter 1

Introduction

1.1 Very High-Energy/Ultrahigh-Energy Astrophysics

The world's highest particle beam energy of ~ 1 TeV ($1 \text{ TeV} = 10^{12} \text{ eV}$) was recently achieved by high-energy physicists in the laboratory. Cosmic-ray physicists have long been using the abundant very high-energy (VHE, $E = 10^{11}$ – 10^{14} eV), ultrahigh-energy (UHE, $E = 10^{14}$ – 10^{17} eV) and higher energy cosmic-ray particles produced by nature as a tool to study the interactions of particles at these extreme energies and to probe the secrets of the universe. The production mechanisms of these cosmic rays at such high energies are still not well known, but cosmic rays provide an excellent test bed for both experimental and theoretical astrophysicists.

It has been known that the composition of cosmic rays is predominantly protons and heavier nuclei, but only neutral particles can retain the directional information from celestial point sources, unaltered by the interstellar magnetic fields. Neutrons, neutrinos and γ -rays are the candidates for such an information carrier. Due to their short lifetime (~ 15 minutes in the rest frame), neutrons are

excluded from the list when searching for point sources at astrophysical distances. For example, a 10^{15} eV neutron will decay at a distance of ~ 10 parsec (pc, 1 pc = 3.26 light years) while the expected sources are usually thousands of parsec away. Neutrinos are extremely difficult to use because of their very small interaction cross section. Therefore, γ -rays become the most probable candidates to look for the directional excesses from point sources. Gamma rays do not only point back to their source, but also reveal the nature of the cosmic accelerators. The massive charged cosmic rays, losing their original directions in the interstellar fields, constitute the isotropic background at earth. Signals are buried in such a large background. Therefore, methods that reject the background and make the signal stand out are a valuable area of investigation.

At present, the energy range of VHE/UHE γ -ray astrophysics has been extended to 10^{20} eV. Since the γ -ray flux from a source generally decreases rapidly with increasing energy (usually a power-law spectrum), different detection techniques are employed to search for γ -rays in different energy regimes.

1.2 Detection Techniques for VHE/UHE Cosmic Rays and Gamma Rays

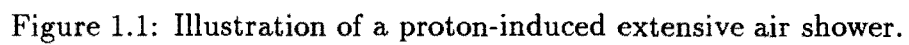
As the VHE/UHE particle flux at the top of the atmosphere is very low, space-based experiments for direct measurements of these primary particles (or primaries) are not suitable because of the large detector areas needed. For example, the updated

Crab integral γ -ray energy spectrum¹ measured by the Whipple Observatory [1, 2] is

$$N(>E) = 0.87 \left(\frac{E}{1\text{TeV}} \right)^{-1.69} \times 10^{-11} \text{ photons cm}^{-2} \text{ s}^{-1}, \quad (1.1)$$

which corresponds to a flux of only ~ 3 photons per m^2 per year at 1 TeV, so that a balloon or satellite experiment becomes impractical. Therefore, large ground-based arrays using the atmosphere as part of their detection medium are used instead. When a primary interacts with an atmospheric nucleus near the top of the atmosphere, a secondary particle cascade, or extensive air shower (EAS), develops. The interaction of a charged cosmic ray produces secondary nucleons and mesons. The neutral pions quickly decay into photons and the photons produce electrons and positrons via pair production which radiate photons through bremsstrahlung. This photon and electron cascade in turn generates more secondary photons and electrons and hence creates an electromagnetic cascade. The charged pions either interact with air nuclei or decay into muons and neutrinos. Since muons and neutrinos are the more penetrating part of the shower, they can reach the ground without further interactions. Gamma-induced showers mostly have the electromagnetic component of the shower development. Fig. 1.1 shows a diagram of the development of an EAS [3]. Showers initiated by γ -ray primaries are expected to have fewer muons (by at least a factor of 20) than those initiated by hadrons [4, 5, 6, 7].

¹The Whipple collaboration has changed the flux several times in the past few years. Here the most recent published value is given.



Atmospheric-Čerenkov Technique

VHE telescopes typically employ the atmospheric Čerenkov technique. This technique is based on the fact that the charged component in the EAS generates cones of Čerenkov radiation (mostly in the wavelength interval 4300–5500Å) about the particle direction. This occurs when the charged particle’s speed exceeds the local speed of light, with a characteristic angle described by

$$\theta_c = \cos^{-1} \left(\frac{1}{\beta n} \right), \quad (1.2)$$

where β is the velocity of the charged particle in units of c (the speed of light in vacuum), and n is the refractive index of the medium (atmosphere, in this case) through which the charged particle passes. The Čerenkov light is highly collimated with respect to the original particle direction and can be detected by photomultiplier tubes (PMTs) mounted at the focal plane of a mirror. The energy range of this technique is from a few hundred GeV (1 GeV is 10^9 eV) to perhaps 10 TeV. The detection threshold is limited by the sky background (e.g., diffuse starlight, air glow, etc.). These experiments work best during moonless, cloudless nights, so that their relative live time is short, about 5%–10%. The aperture of the detectors is also small. These telescopes usually track one source at a time.

Air-Shower Technique

Another way to measure the primary particle indirectly is to detect the secondary particles (or secondaries) in the EAS using radiation detectors on the ground. These surface arrays are typically composed of scintillation counters (usually of dimensions $\sim 1 \text{ m}^2$) or water-Čerenkov detectors distributed over an area of 10,000

to 100,000 m². The secondaries form a slightly curved *pancake*-shaped air-shower front (~ 200 m wide and ~ 1 m thick) propagating down to the surface of the earth (see Fig. 1.2). Ground arrays measure the relative arrival times between counters when the showerfront hits them in sequence and determine the incoming direction of the EAS. These experiments operate at energies above ~ 100 TeV. Unlike the air-Čerenkov experiments, experiments with particle detector arrays can be carried out day and night, and they can observe the entire overhead sky.

Air-Fluorescence Technique

This technique is useful at energies > 100 PeV (10^{17} eV). It relies on the scintillation light produced by nitrogen molecules (in the atmosphere) excited by the EAS. Such N₂ molecules de-excite by emitting near-ultraviolet fluorescence photons isotropically. The air-fluorescence technique allows a large collection area because the fluorescence is isotropic which makes it useful for studying the highest energy cosmic rays. Like the air-Čerenkov telescopes, the air-fluorescence detectors works best on dark moonless nights; however, a large fraction of the whole night sky is under view.

1.3 Historical VHE/UHE Surveys

Over the last two decades, more than 20 sources have been claimed as VHE/UHE emitters. A source list has been compiled by several authors (see, e.g., Fegan [8], Chadwick [9], and Weekes [10]) in their review articles.

For over 20 years, the Crab pulsar and nebula have been identified as sources of both pulsed and unpulsed radiation from radio wavelengths to VHE γ -rays.

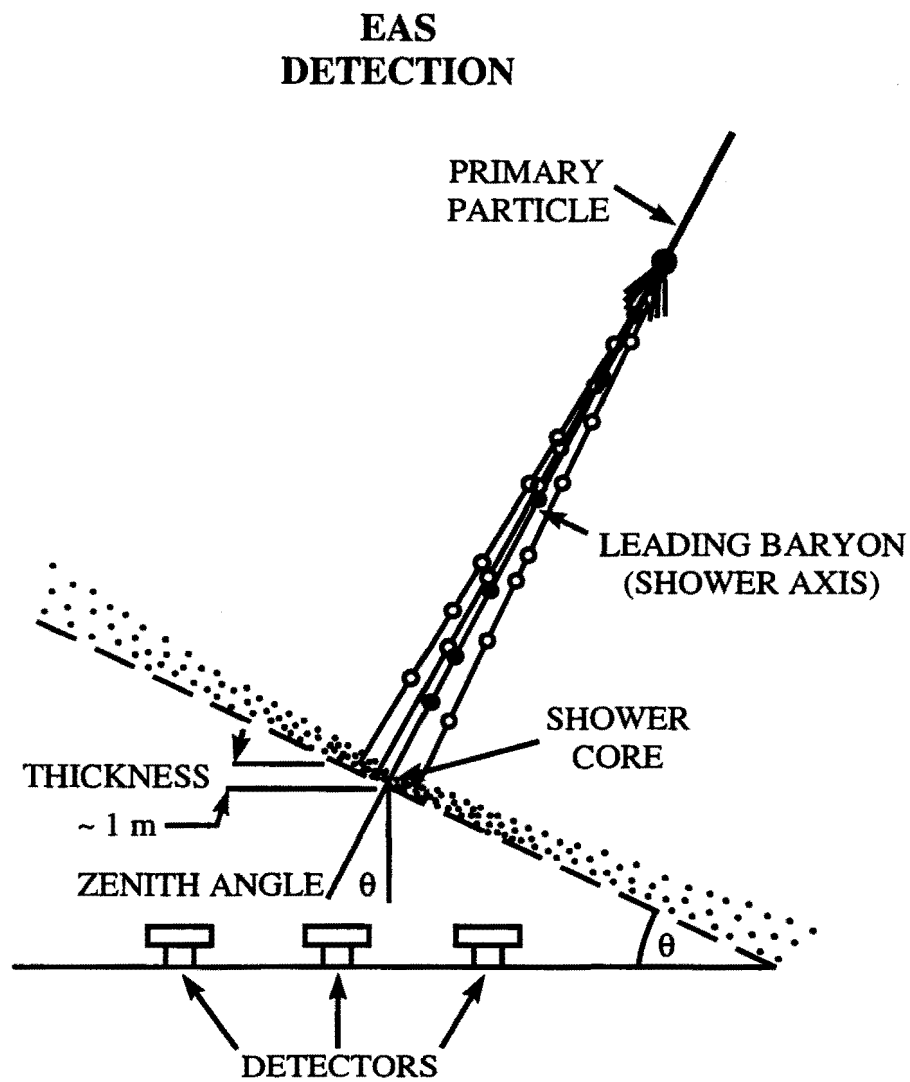


Figure 1.2: Typical ultrahigh-energy detector and extensive air shower.

Unpulsed emission from the Crab has been observed in the PeV regime [11, 12, 13]. It is now considered as the “standard candle” for gamma-ray sources and is one of the intriguing sources constantly observed by many groups. VHE γ -ray fluxes from the Crab have been measured both by the Whipple group [1] and by the THEMISTOCLE group [14].

Special attention should be given to the pulsating X-ray source Hercules X-1. In 1986, episodic activity from the direction of Hercules X-1 was observed by four different groups (CYGNUS [15], Whipple [16], Haleakala [17] and Ooty [18]) at VHE/UHE energies. All four groups reported pulsed emission at a similar blue-shifted (relative to the known X-ray pulsar frequency) frequency (Fig. 1.3). The cause of the shift is not understood, but implies a different production mechanism from the X-ray emission. The Whipple collaboration was able to use their selection technique (“AZWIDTH”) to distinguish the hadronic showers from the photonic showers. This is the same technique they applied to make a significantly improved result when observing the Crab nebula [19, 20, 21]. The CYGNUS experiment can measure the muon content of showers to separate the hadronic and photonic showers. Both observations indicated a cosmic-ray like (muon-rich) event, and hence failed to confirm the gamma-ray origin of the signal. No other detections have been observed from Hercules X-1 since then, while detector sensitivities have been significantly improved. This muon puzzle, if it is true, indicates that a new unknown neutral particle is involved or that γ -ray behaves differently at higher energies or that the result is a statistical fluke.

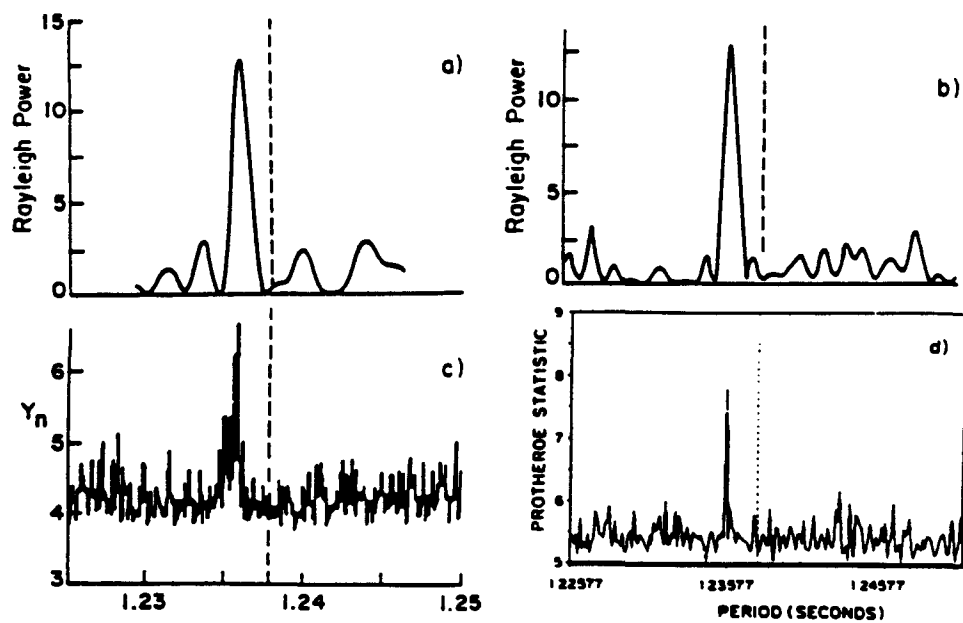


Figure 1.3: Observations of Hercules X-1 at a blue-shifted frequency by 4 groups in 1986: (a) CYGNUS [15]; (b) Whipple [16]; (c) Haleakala [17]; (d) Ooty [18].

Chapter 2

Pulsar Physics

2.1 Overview

Since the first discovery of pulsating radio signals from pulsars more than 26 years ago [22], pulsars have become an intriguing class of objects to study, and considerable progress in understanding them has been made. Almost all the pulsars emit radio pulses, and some of them have higher-energy emissions in the X-ray and γ -ray ranges. They have been identified conclusively as fast spinning, strongly magnetized neutron stars. At least 558 pulsars have been found by 1993 [23], and most of them reside in our galaxy and populate the galactic plane. Most pulsars are not in binary systems; only about four percent are now known to be in binaries.

The high coherence and directionality of radio emission from pulsars is naturally assumed to be due to the presence of a strong magnetic field and plasma in the vicinity of the neutron stars, i.e. the pulsar magnetosphere in which the radiation is generated (see Fig. 2.1). The magnetic dipole axis and the rotation axis are not necessarily aligned, thus different types of pulse profiles (e.g., single peak or double peaks) can be produced.

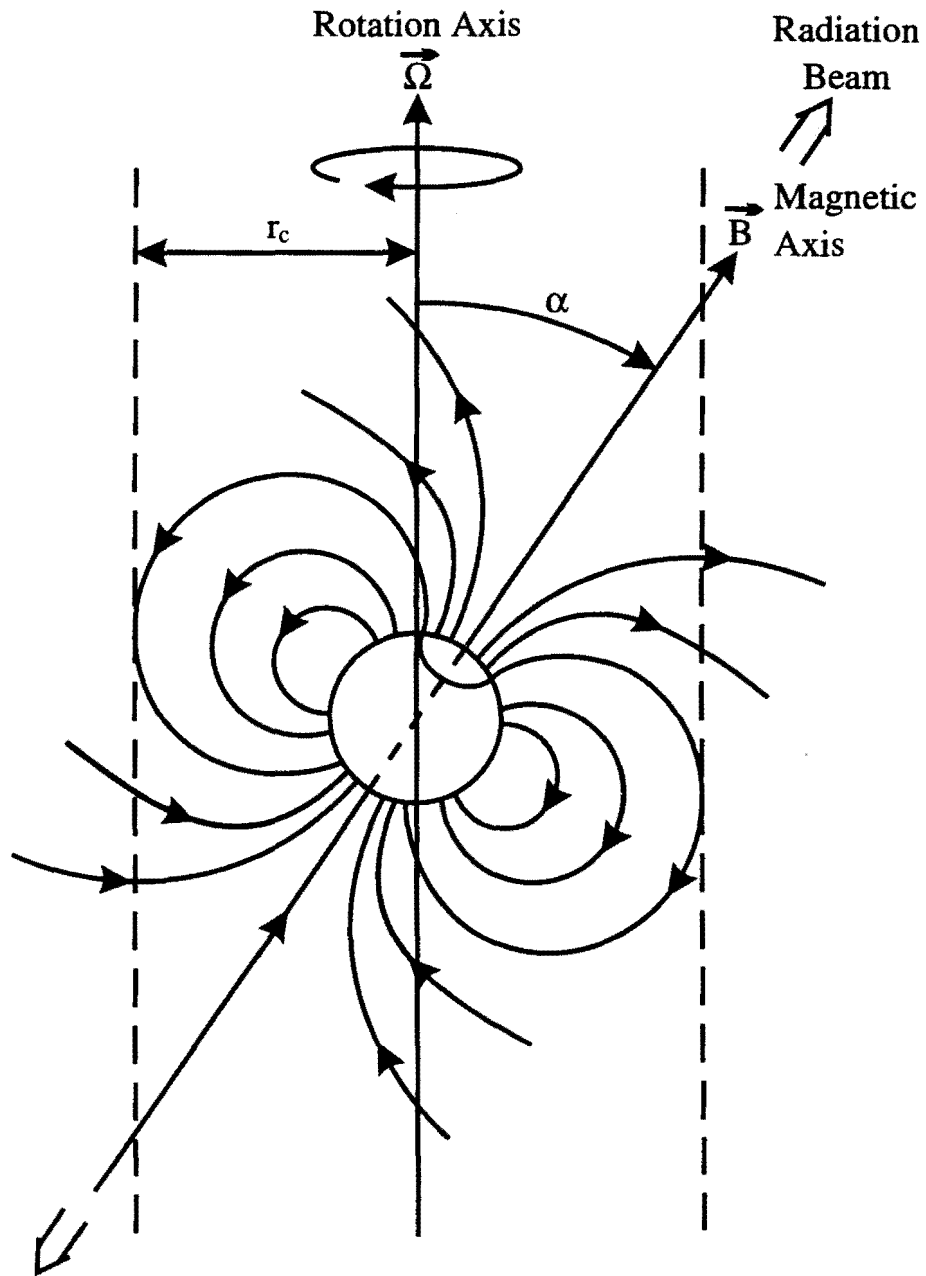


Figure 2.1: A model of a radio pulsar as a strong magnetized neutron star, showing regions of radio emission generation.

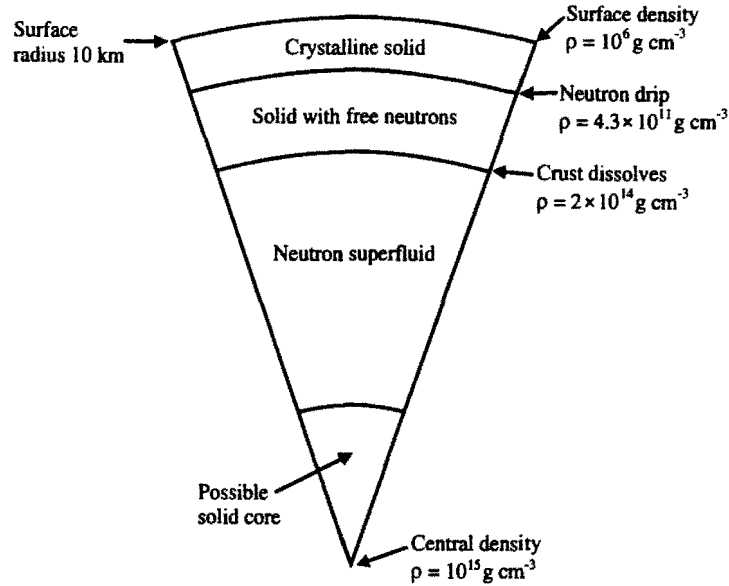


Figure 2.2: Typical cross section of a neutron star [25].

2.2 Neutron Stars

The Galaxy contains at least $10^{9\pm1}$ neutron stars which are thought to be born in supernova explosions of massive stars, and which one observes as radio pulsars if isolated and as X-ray binaries if attached to a close companion [24]. Neutrons stars are compact objects, but their mass densities are enormous (from $\sim 10^6$ g/cm³ at the crust to $\sim 10^{15}$ g/cm³ at the core). Fig. 2.2 shows a cross sectional view of a typical neutron star [25].

A typical neutron star possesses the following properties:

- Radius $R \simeq 10^6$ cm.
- Magnetic field $B \simeq 10^{12}$ Gauss.

- Mass $M \gtrsim 1.4 M_{\odot}$.
- Moment of inertia $I \simeq 10^{45} \text{ g cm}^2$.

2.3 Periods of Pulsars

The fundamental quantities to be observed are the pulsars' period (P) and their spin-down rate (dP/dt). The pulsating signals from a rotating neutron star are derived from a lighthouse beam, as it sweeps along the line of sight. The distribution of pulsar periods ranges from 1.5 ms to 4 s, with most having periods of 0.2 s to 2 s. The periods are gradually increasing as they slowly lose their rotational energy via radiation. The period increase rate $\dot{P} = dP/dt$ is stable and for the majority of pulsars ranges between 10^{-14} and $10^{-16} \text{ s s}^{-1}$. Fig. 2.3 [23] shows the distribution of pulsars on the P - \dot{P} diagram. The symbol size increases with the distance $|z|$ from the galactic plane. Minus signs through three of the points denote negative values of \dot{P} , plotted as absolute values. Large circles surrounding dots represent binary pulsars. A number of pulsars shows jump-like discontinuities, or “glitches,” in their periods. The sharp decrease of the period is believed to result from the inner activities of the neutron stars [26, 27, 28].

The rate of change of the angular frequency, Ω , is assumed to be

$$\dot{\Omega} = -k\Omega^n, \quad (2.1)$$

or, equivalently,

$$\dot{P} = (2\pi)^{n-1} k P^{2-n}, \quad (2.2)$$

where the parameter n is known as the braking index, and k is a positive constant. If the braking torque stems only from the magnetic dipole radiation, in which case

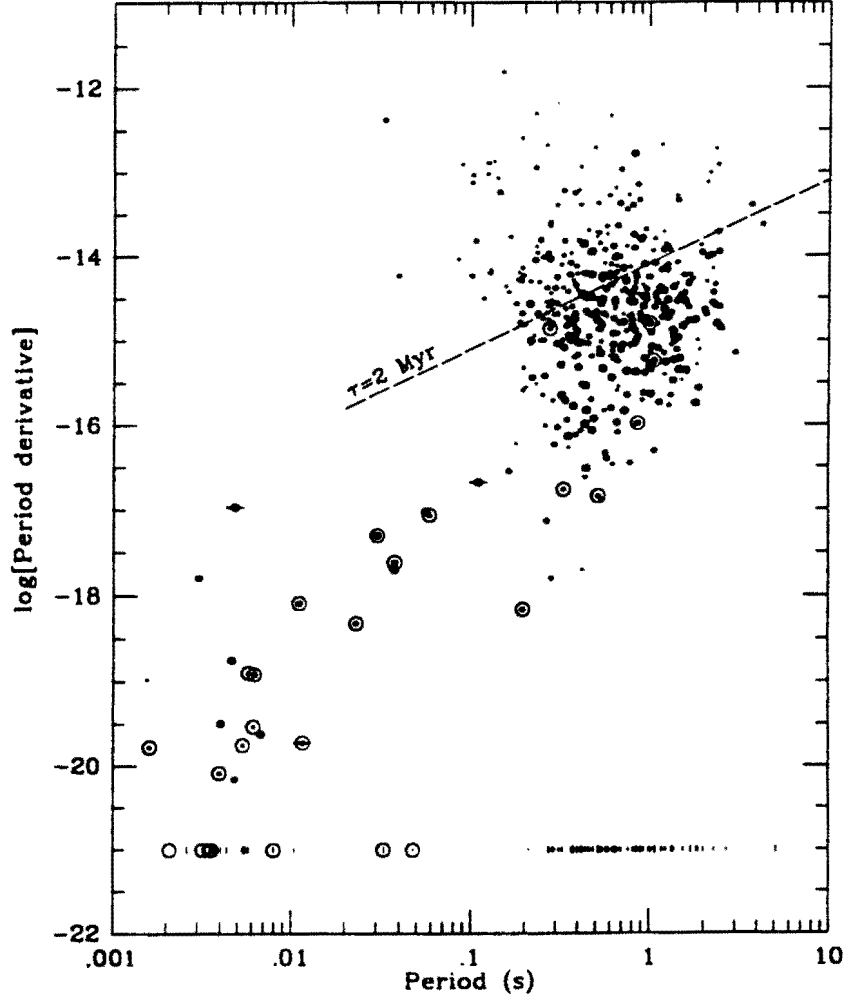


Figure 2.3: Distribution of periods and period derivatives for 468 pulsars (extragalactic pulsars are omitted). Symbol size increases with distance $|z|$ from the galactic plane. The dashed line corresponds to spin-down age $\tau = 2 \text{ Myr}$; pulsars older than about this limit have significantly larger z -dispersions than do younger ones. Minus signs through three of the points denote orbiting pulsars. Another 85 pulsars with unmeasured \dot{P} are aligned near the bottom of the figure, using vertical strokes for their symbols [23].

$n = 3$, then the “characteristic age” of the pulsar is shown to be [29]

$$t_c = \frac{P}{2\dot{P}}. \quad (2.3)$$

Some other quantities can also be derived from the observed data, including the “spin-down luminosity” (the loss rate of rotational energy)

$$\dot{E} = -I_{45}\Omega\dot{\Omega} = -4\pi^2 I_{45}\nu\dot{\nu} = 4\pi^2 I_{45}\dot{P}P^{-3} \quad (2.4)$$

and the neutron star’s surface magnetic field strength, taken to be

$$B = \left(\frac{3I_{45}c^3 P \dot{P}}{8\pi^2 R_6^6} \right)^{1/2} \approx 3.2 \times 10^{19} (P \dot{P})^{1/2} \quad (2.5)$$

(see, e.g., Manchester and Taylor [30]). In the above expressions, the frequencies $\nu = 1/P$ and $\Omega = 2\pi\nu = 2\pi/P$, R and I are the neutron star’s radius and moment of inertia, taken to be 10^6 cm and 10^{45} g cm², respectively, and c is the speed of light.

2.4 Binary Pulsars and Millisecond Pulsars

As mentioned in the beginning of this chapter, the overwhelming majority of radio pulsars are isolated neutron stars. Only a few pulsars are members of binary systems. Most of the high-mass stars thought to be pulsar progenitors evolve in binary systems [31], yet only a small portion of known pulsars exhibits the periodic Doppler shift caused by the orbital motion about a companion [32, 33, 34, 35, 36].

The orbiting systems containing pulsars are rather diverse. Their orbital periods range from $P_b \simeq 1.4$ hr to $P_b > 3$ yr, with circular or strongly eccentric ($e \sim 0.6$) orbits. The mass function [37], found directly from observations,

$$f(M_c, M_p, i) = \frac{M_c^3 \sin^3 i}{(M_p + M_c)^2} \quad (2.6)$$

also varies widely, where i is the inclination angle of the plane of the orbit with respect to the line of sight, M_p is the mass of the pulsar, and M_c is the mass of its companion.

The discovery of the first millisecond pulsar PSR 1937+21 defines a separate class of objects and opens a new era in pulsar physics. Millisecond pulsars in binaries are thought to be old neutron stars spun up by accreting matter and acquiring additional angular momentum from their respective companion [38]. Under certain circumstances a dead pulsar may be resurrected by the accretion; this is the so-called “recycled” pulsar. Low-mass X-ray binaries (LMXBs) are believed to be the progenitors of millisecond pulsars. The interest in millisecond pulsars is also explained by the fact that the periods of known young pulsars are anomalously small. Therefore, some authors [39, 40] argue that many pulsars must be born with small periods. Millisecond pulsars have some properties that deviate from ordinary radio pulsars. They have weak surface magnetic fields ($\sim 10^8$ G) and much older ages (apparent ages greater than $\sim 10^9$ years). Some of the millisecond pulsars have been reported to emit TeV γ -rays (see, e.g., Weekes [10] for a review), such as PSR 1937+21, PSR 1953+29, and PSR 1957+20, in addition to the famous Crab pulsar (PSR 0531+21).

The fast pulsars selected in this work are mainly based on the γ -ray observations claimed by other experiments. Five of them are examined for TeV emission. They are close to the zenith so that the CYGNUS experiment can have longer observation time. They are also within a few kpc of the sun so that they have better chance to be detected, because the more distant the source is, the smaller the flux observed. Except for the Crab pulsar, they have never been searched by

the CYGNUS experiment for pulsed emissions. They are described below in more detail.

2.4.1 The Crab Nebula and Pulsar PSR 0531+21

The Crab Nebula and pulsar are the most well-studied and prominent celestial objects at all wavelengths from radio to γ -rays. The pulsar is located at the center of the Nebula formed by a supernova explosion. The Crab Nebula is the brightest X-ray supernova remnant in the Galaxy. Numerous detections have been reported from the direction of the Crab. It was first seen in the VHE energy regime by the Smithsonian Astrophysical Observatory [41]. Over the years a number of experiments have confirmed its existence. See Table 2.1 for a summary [42].

Both the Whipple and THEMISTOCLE collaborations measured the Crab energy spectrum. To determine the spectrum it requires conversion of the observed number of γ -rays into the flux. This needs the knowledge about the telescope’s response to the γ -rays with a given energy. The telescope’s collection area, which includes the effects of atmospheric absorption, the instrumental effects and the effects of any cuts that are applied to the data, can be derived from measurements and Monte Carlo simulations. A previous measurement of the spectrum by Whipple [19] gave

$$\frac{dN(E)}{dE} = 2.5 \times 10^{-10} \left(\frac{E}{0.4 \text{ TeV}} \right)^{-2.4 \pm 0.3} \text{ photons cm}^{-2} \text{ s}^{-1} \text{ TeV}^{-1} \quad (2.7)$$

for the VHE differential γ -ray flux between 0.4 and 4.0 TeV. The Whipple collaboration applied their “extended supercuts” technique, which made the determination of the spectral slope less energy-dependent, to the same data [1] and obtained a

Group	Epoch	Energy ($> E$, TeV)	Flux	Ref.
Sandia	1987-8	0.2	17	[43]
Moscow	1960-2	5	< 5	[44]
Mount Hopkins	1969-72	0.25	4.4	[41]
Tien Shan	1981-2	2	5.8	[45]
Sandia	1987	0.4	6.3	[46]
Whipple	1986-8	0.7	1.8	[19]
Whipple (old)	1988-9	0.4	7.0	[20]
Whipple (new)	1988-9	0.4	4.1	[1]
Lodz	1968-82	2×10^4	0.02	[47]
Fly's Eye	1980	1000	0.21	[48]
	1989	70	< 0.099	[49]
Whipple (EAS)	1989	45	< 0.39	[50]
Ooty	1984-7	200	< 0.077	[51]
Utah-Michigan	1988-9	270	< 0.023	[52]
			$< 0.001^*$	[52]
KGF	1989 Feb. 23	100	1.3	[53]
THEMISTOCLE	1991-2	3	0.7	[14]
	1991-4	2	0.43	[54]
HEGRA	1992-3	2	1.5	[55]
HEGRA (EAS)	1989-92	48	< 0.012	[56]
	1989-92**	39	< 0.0066	[56]
	1992-3	49	< 0.024	[57]
CASA-MIA	1990-1	190	< 0.0026	[58]
			$< 0.0021^*$	[58]
	1990-4	138	$< 0.0009^*$	[59]
Durham	1989-90	3	< 0.3	[60]
GREX	1986-90	840	$< 0.001^*$	[61]
EAS-TOP	1989-94	25	< 0.033	[62]
Tibet	1990-2	10	< 0.12	[63]
ASGAT	1991-2	0.6	< 2.7	[64]
Crimean	1993 Oct.	1	1.3	[65]
CYGNUS	1986-91	40	< 0.029	[66]
			$< 0.066^*$	[66]

* When μ -poor showers are selected.

** When subsamples of showers are selected.

Table 2.1: Summary of the steady flux from the Crab. The unit of the flux is $(\text{photons cm}^{-2} \text{ s}^{-1}) \times 10^{-11}$. Adapted from Ramana Murthy and Wolfendale [42].

new differential spectrum¹:

$$\frac{dN(E)}{dE} = (1.48 \pm 0.42) \times 10^{-11} \left(\frac{E}{1\text{TeV}}\right)^{-2.69 \pm 0.31} \text{ photons cm}^{-2} \text{ s}^{-1} \text{ TeV}^{-1}. \quad (2.8)$$

The THEMISTOCLE collaboration also measured the integral energy spectrum in the interval from 3 to 15 TeV which gave

$$N(> E) = (3.7 \pm 0.5) \times 10^{-12} \left(\frac{E}{5\text{TeV}}\right)^{-1.5 \pm 0.2} \text{ photons cm}^{-2} \text{ s}^{-1} \quad (2.9)$$

for the integral flux from the Crab. Their analysis does not depend on the shape of the image but on the reconstruction of shower direction from the arrival time of the Čerenkov light wave front [68]. The THEMISTOCLE group can therefore make cuts on the air showers, such as the core location, to reduce the energy uncertainty to about 20%. This result is in apparent disagreement with the Whipple measurement. A comparison at 5 TeV, for example, gives a THEMISTOCLE result that is more than 6 times higher than the Whipple result. Therefore, the VHE γ -ray flux from the Crab is still not determined with a high degree of certainty.

The Crab pulsar is the youngest known pulsar. Over the past twenty-five years there have been many claims that the 33-ms signature was observed at TeV energies (reviewed in, e.g., Weekes [69] and Ramana Murthy and Wolfendale [42]). Table 2.2 lists the results of pulsed emission from the Crab pulsar. Irregularities in the pulse timing have been seen several times. The glitches in period amount to only one part in 10^8 of the period. They have been observed in 1969, 1975, 1986, and 1989. The ephemeris of the Crab pulsar, obtained from radio observations, is provided by Jodrell Bank [78]. The pulsar parameters are given in Table 2.3. The

¹This flux may be changed by the Whipple collaboration. However, no official result has yet been published [67].

Group	Epoch	Energy ($> E$, TeV)	Flux	Ref.
Ooty	1977 Feb.	4.5	0.4	[70, 71]
			0.29	[70, 71]
	1978	2.5	< 0.2	[71]
	1979	1.9	< 0.2	[71]
	1980	1.5	< 0.27	[71]
Durham	1985	1.2	25	[72]
	1981 Oct.	3	20	[73]
			0.15	[73]
	1982	1.0	0.79	[74]
Edwards	1982	0.2	2.5	[75]
Whipple	1986–8	0.7	< 0.45	[19]
	1988–9	0.4	< 0.7	[20]
	1993–4	0.4	< 0.019	[50]
Sandia	1987–8	0.2	< 1.3	[43]
Pachmarhi	1987–8	1.1	< 0.6	[76]
	1988–9	1.8	< 0.2	[76]
	1989 Jan.	2.8	14	[77]
Ooty (PeV)	1984–7	200	0.041	[51]
Durham	1981–3	1	$0.8, 20^\dagger$	[60]
	1988–9	0.4	< 5	[60]
	1990–1	3	< 0.1	[60]
EAS-TOP	1989–94	25	< 0.006	[62]
CYGNUS	1986–91	40	< 0.09	[66]
			$< 0.034^*$	[66]

† Peak pulsed flux.

* When μ -poor showers are selected.

Table 2.2: Results on pulsed emission of VHE/UHE γ -rays from the Crab pulsar. The unit of the flux is $(\text{photons cm}^{-2} \text{ s}^{-1}) \times 10^{-11}$. Adapted from Ramana Murthy and Wolfendale [42].

Parameter	PSR 0531+21
Right Ascension α (B1950)	05 ^h 31 ^m 31 ^s .406
Declination δ (B1950)	21°58′54″.391
Right Ascension α (J2000)	05 ^h 34 ^m 31 ^s .949
Declination δ (J2000)	22°00′52″.057
Frequency ν (Hz)	29.9286798941 (1993 Jan 15)
Frequency derivative $\dot{\nu}$ (10^{-15} s^{-2})	−377003.97 (1993 Jan 15)
Distance d (kpc)	2.0

Table 2.3: Parameters of the Crab pulsar. The observed frequency ν and its first derivative $\dot{\nu}$ are given at the quoted date. Monthly ephemerides are listed in Ref. [78].

light curves of the Crab pulsar at radio to γ -ray wavelengths show a double-peak structure [79], with the peaks all aligned at the same phases. The separation of the main peak from the interpulse is 13 ms, or 0.4 in phase.

2.4.2 PSR 1937+21

Of the known pulsars, the millisecond pulsar PSR 1937+21 has the shortest period and an exceptionally slow spin-down rate. No associated star is found for PSR 1937+21. However, Ruderman and Shaham [80, 81] suggest that the progenitor of PSR 1937+21 is a close binary system containing a neutron star and a very-low-mass ($\lesssim 0.02 M_{\odot}$) degenerate dwarf helium star, while Jeffrey [82] argues that PSR 1937+21 cannot originate from the disruption of such a system. Blondin and Freese [83] therefore propose that PSR 1937+21 could be a young neutron star spun up

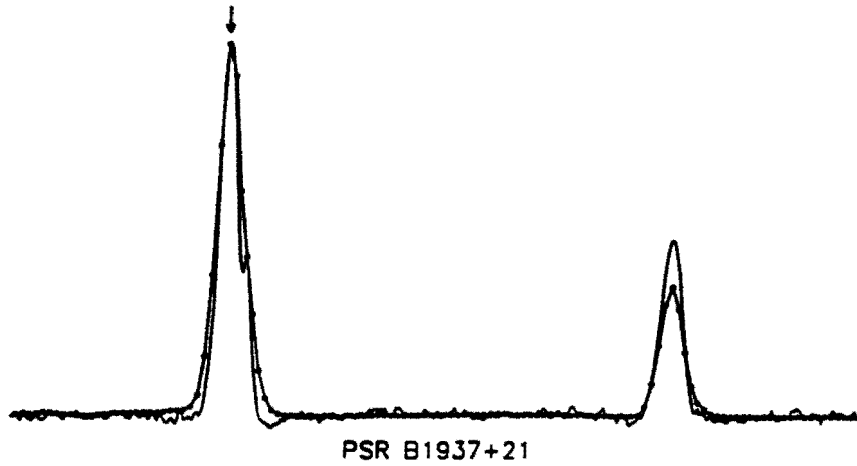


Figure 2.4: Pulse profiles for PSR 1937+21 [87], obtained with observation systems at 1408 MHz (solid line) and 2380 MHz (line with dots). The arrow marks the phase of the nominal pulse arrival time.

by accreting mass from a high-mass partner in a close binary system and then left isolated when the companion underwent a supernova explosion. Radio observations of the pulse profile show an interpulse about 172° apart from the main pulse [84]. This separation appears to be nearly independent of frequency [84, 85, 86], just as in the case of the Crab pulsar. A “notch” pulse following the main pulse with a separation of 8.6° [84] is also found at frequencies between 1330 MHz and 3 GHz. Pulse profiles for PSR 1937+21 [87] are given in Fig. 2.4. Timing parameters of PSR 1937+21 from radio measurement [87, 88] are shown in Table 2.4.

The Durham group reported a marginal detection of pulsed emission from

Parameter	PSR 1937+21
Right Ascension α (B1950)	19 ^h 37 ^m 28 ^s .74601(2)
Declination δ (B1950)	21°28′01″.4588(3)
Right Ascension α (J2000)	19 ^h 39 ^m 38 ^s .560210(2)
Declination δ (J2000)	21°34′59″.14166(6)
Pulse period P (ms)	1.557806468819794(2)
Period derivative \dot{P} (10^{-20} s s ⁻¹)	10.51193(2)
Frequency ν (Hz)	641.9282626022265(8)
Frequency derivative $\dot{\nu}$ (10^{-16} s ⁻²)	-433.1671(8)
Frequency second derivative $\ddot{\nu}$ (10^{-27} s ⁻³)	13.2(3)
Epoch t_0 (JD - 2,440,000)	7500.000000015133
Distance d (kpc)	3.6

Table 2.4: Timing parameters of PSR 1937+21 [87, 88]. Figures in parentheses are uncertainties in the last digit quoted.

PSR 1937+21 in 85 hours of observation during 1984 July, August and September with 10^{-4} chance probability level above 1 TeV [89]. The pulsed emission did not show up in their 1983–4 data [90]. The period found was consistent with the expected period from the radio ephemeris. However, no positive detections from other groups have been reported. It is better that the TeV emission can be confirmed by another independently operated experiment. This is the major reason why this pulsar is put on the search list in this work.

PSR 1937+21 was not seen by the EAS-TOP collaboration in their 1988–9 observation period [91]. They derived an upper limit to the steady flux at the 95% confidence level (CL) to be 2.2×10^{-13} photons $\text{cm}^{-2} \text{s}^{-1}$ at $E > 150$ TeV. Morello et al. [92] also reported a null result in their 1982–7 data from the Plateau Rosa Station at primary energy $E > 30$ TeV. The steady flux upper limit given was 6.3×10^{-12} photons $\text{cm}^{-2} \text{s}^{-1}$ at the 95% CL. Other steady flux upper limits (90% CL) reported are 1.9×10^{-13} photons $\text{cm}^{-2} \text{s}^{-1}$ above 70 TeV by HEGRA during their 1989–92 observation [93], 4.2×10^{-13} photons $\text{cm}^{-2} \text{s}^{-1}$ above 50 TeV by HEGRA during their 1992–3 observation [57], 1.5×10^{-13} photons $\text{cm}^{-2} \text{s}^{-1}$ above 0.2 PeV by BASA during their 1985–92 observation [94], and 3.3×10^{-14} photons $\text{cm}^{-2} \text{s}^{-1}$ above 120 TeV by EAS-TOP during their 1989–94 observation [62].

2.4.3 PSR 1951+32

The recently discovered 39.5 ms radio pulsar PSR 1951+32 [95, 96] is located at the center of the supernova remnant (SNR) CTB 80. Radio observations at Arecibo gives the timing properties of PSR 1951+32 [97] (see Table 2.5). Although this pulsar has not been observed at the VHE energies, it is found to emit X-rays [98]

Parameter	PSR 1951+32
Right Ascension α (B1950)	19 ^h 51 ^m 02 ^s .52(5)
Declination δ (B1950)	32°44′50″.4(2)
Right Ascension α (J2000)	19 ^h 52 ^m 58 ^s .308
Declination δ (J2000)	32°52′40″.569
Pulse period P (s)	0.039529758092(1)
Period derivative \dot{P} (10^{-15} s s ⁻¹)	5.8494(1)
Epoch t_0 (JD – 2,440,000)	7005.688
Distance d (kpc)	2.5

Table 2.5: Timing parameters of PSR 1951+32 [97]. Figures in parentheses are uncertainties in the last digit quoted.

and γ -rays [99]. PSR 1951+32 has a broad main pulse, and may be followed by a weak interpulse ($< 2\%$ of the integrated flux density of the main pulse) 180° from the main pulse. The integrated profiles are shown in Fig. 2.5 [97].

CTB 80 has a Crab-like nebula (the “plerion”). The discovery of PSR 1951+32 identifies the source of energy injection at the center as the rotational energy loss of the pulsar [100]:

$$\dot{E} = I\Omega\dot{\Omega} = 3.7 \times 10^{36} \text{ ergs s}^{-1},$$

which is about two orders of magnitude smaller than that of the Crab Nebula. Recently, γ -ray emission from this source has been detected by the Energetic Gamma Ray Experiment Telescope (EGRET) [101] onboard the Compton Gamma Ray Observatory (CGRO), pulsating in γ -rays at energy > 100 MeV with the same

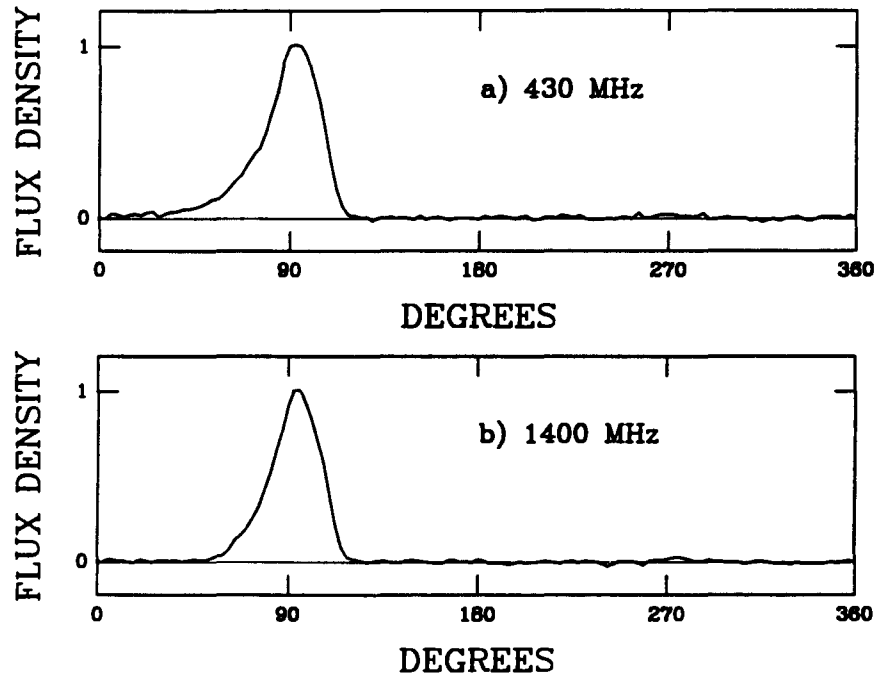


Figure 2.5: The integrated profiles from PSR 1951+32 are shown at two observing frequencies (a) 430 MHz and (b) 1400 MHz. A very weak interpulse ($< 2\%$ of the main pulse) may be present 180° from the main pulse [97].

39.5-ms periodicity as detected at radio wavelengths. However, no unpulsed emission from this object (i.e. the SNR) is observed by EGRET. Although there are no well-developed models for TeV emission from plerions, these are probably the best candidates for detection as steady TeV γ -ray sources [10].

2.4.4 PSR 1953+29

PSR 1953+29, a LMXB, has an orbital period of 117.3 days, a period $P = 6.1$ ms, a very small spin-down rate $\dot{P} = 2.95 \times 10^{-20}$ and a nearly circular orbit ($e \approx 0$) (see Table 2.6). This system is of great interest because it can reveal the evolution history of pulsars and close binary stars. Its integrated pulse profile fluctuate widely at different frequencies [102] (see Fig. 2.6).

Chadwick et al. [90] reported a detection of pulsed TeV γ -rays consistent with the radio period. The observations were made between July and October 1983 and during July 1984. The significance is at the 5.4σ (chance probability = 4×10^{-8}) level, corresponding to a time-averaged flux (> 2 TeV) of $(3 \pm 0.8) \times 10^{-11}$ photons $\text{cm}^{-2} \text{s}^{-1}$.

The EAS-TOP collaboration did not see PSR 1953+29 during their 1988–9 observation [91]. They gave a steady flux upper limit (at the 95% CL) of 2.2×10^{-13} photons $\text{cm}^{-2} \text{s}^{-1}$ at $E > 150$ TeV. Morello et al. [92] also claimed no detection in their 1982–7 observation period and gave an flux upper limit (95% CL) of 4.8×10^{-12} photons $\text{cm}^{-2} \text{s}^{-1}$ at $E > 30$ TeV for a steady emission. Other upper limits (90% CL) to the steady flux reported are 4.4×10^{-14} photons $\text{cm}^{-2} \text{s}^{-1}$ above 100 TeV by EAS-TOP during their 1989–94 observation [62], 2.2×10^{-13} photons $\text{cm}^{-2} \text{s}^{-1}$ above 60 TeV by HEGRA during their 1989–92 observation [93], 2.3×10^{-13}

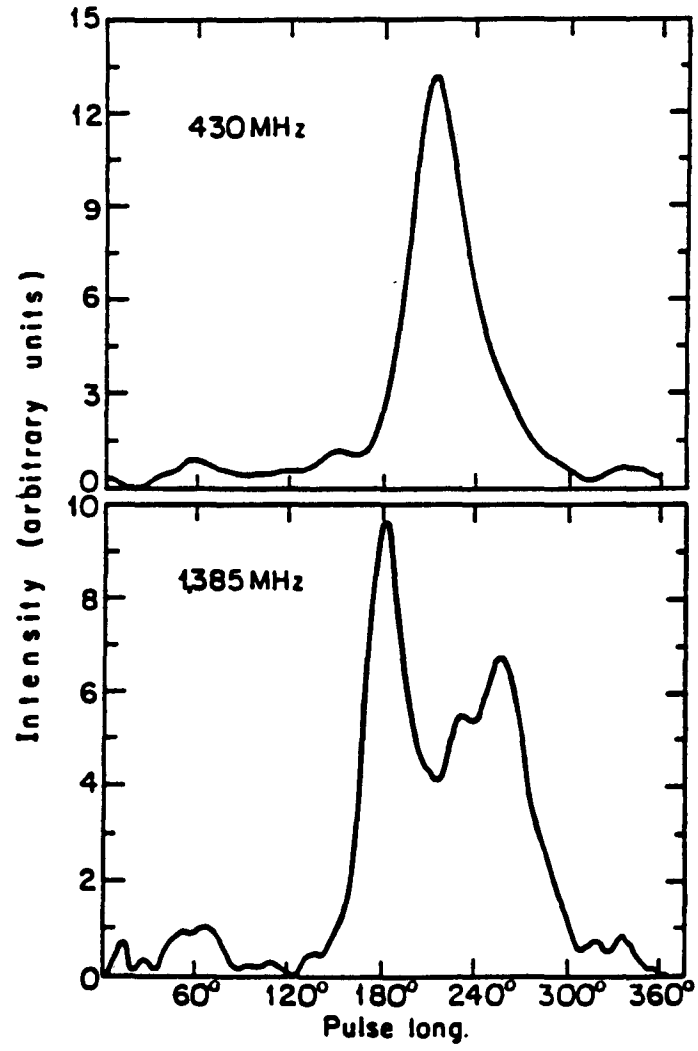


Figure 2.6: Average pulse profiles of PSR 1953+29 at 1385.125 MHz and 430.325 MHz. [102].

Parameter	PSR 1953+29
Right Ascension α (B1950)	19 ^h 53 ^m 26 ^s .7311(3)
Declination δ (B1950)	29°00′43″.734(4)
Right Ascension α (J2000)	19 ^h 55 ^m 27 ^s .8825
Declination δ (J2000)	29°08′43″.646
Pulse period P (ms)	6.133166488729(9)
Period derivative \dot{P} (10^{-20} s s ⁻¹)	2.95(3)
Epoch t_0 (JD − 2,440,000)	6113.1435
Distance d (kpc)	0.8
Orbital period P_b (s)	10138962.0(3)
Orbital eccentricity e (10^{-6})	330.4(3)
Projected semimajor axis x (lt-s)	31.412686(5)
Longitude of periastron ω	29.51°(9)
Periastron time T_0 (JD − 2,440,000)	6112.99(3)

Table 2.6: Timing parameters of the binary pulsar PSR 1953+29 [87]. Figures in parentheses are uncertainties in the last digit quoted.

photons $\text{cm}^{-2} \text{s}^{-1}$ above 47 TeV by HEGRA during their 1992–3 observation [57], and 1.2×10^{-13} photons $\text{cm}^{-2} \text{s}^{-1}$ above 0.2 PeV by BASA [94].

2.4.5 PSR 1957+20

Among the known pulsars, PSR 1957+20 has the second shortest period and the smallest magnetic field. It is an eclipsing binary system consisting of a 1.6 ms radio pulsar and a very light ($0.025 M_{\odot}$) white dwarf companion. Even if the companion star filled its Roche lobe, its extent would be too small to explain the eclipse duration (nearly twice the size of the companion’s Roche lobe). It strongly suggests that the companion is in a process of being ablated by a plasma wind from the pulsar [103]. Therefore, it gets the name of “black widow” pulsar as its partner is being “eaten up” by the pulsar. This LMXB system strongly supports the connection of the millisecond pulsar to the isolated pulsar, as the pulsar’s radiation vaporizes off the companion and will eventually leave behind a single, rapidly rotating pulsar like PSR 1937+21 [104]. The eclipse region is about 9% of the 9.17 hr orbital period during the orbital phase ~ 0.2 – 0.3 , approximately centered at the phase 0.25 (see Fig. 2.7). The pulsar shows an interpulse at radio frequencies, which is strong and centered almost exactly half a period away from the peak of the main pulse (shown in Fig. 2.8). Timing data provided by Ryba and Taylor [105] is presented in Table 2.7.

It has been suggested by Shapiro and Teukolsky [106] that γ -rays could emerge from the orbital phases around the Lagrangian points L4 and L5. If q is the white dwarf–neutron star mass ratio, then the orbital phases of L4 and L5 are at $0.25 \pm \theta/2\pi$, where $\theta = \tan^{-1}\{[3(1+q)/(1-q)]^{1/2}\}$ [107]. In the PSR 1957+20

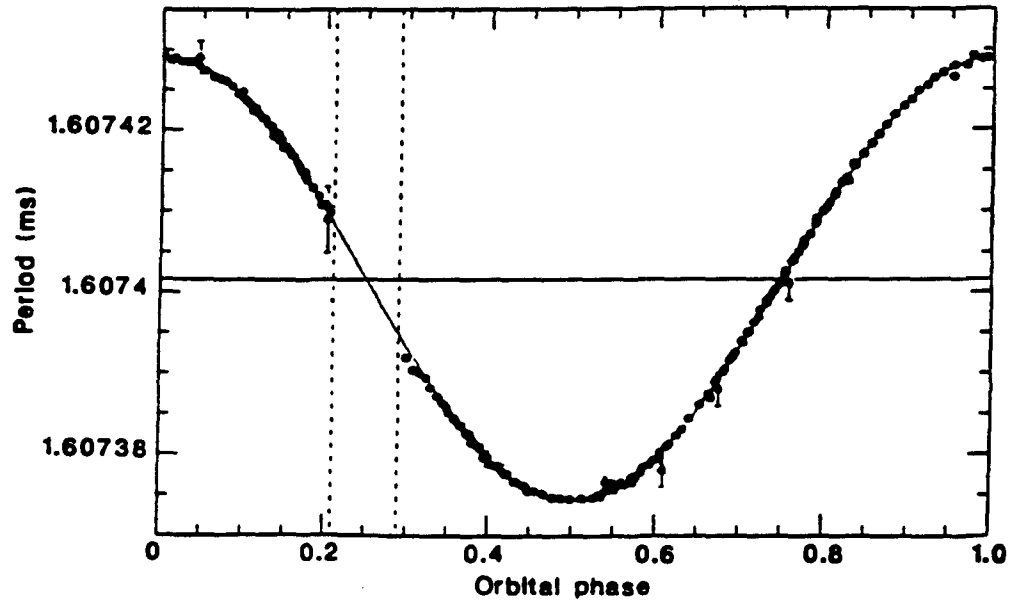


Figure 2.7: Orbital velocity curve of PSR 1957+20. The pulsar is eclipsed by its companion between phases 0.21–0.29 [103].

Parameter	PSR 1957+20
Right Ascension α (B1950)	19 ^h 57 ^m 24 ^s .99101(10)
Declination (B1950) δ	20°39′59″.8106(18)
Right Ascension α (J2000)	19 ^h 59 ^m 36 ^s .77148(10)
Declination δ (J2000)	20°48′15″.1562(18)
Pulse period P (ms)	1.607401684083(2)
Period derivative \dot{P} (10^{-20} s s ⁻¹)	1.683(5)
Period second derivative $ \ddot{P} $ (10^{-30} s ⁻¹)	< 6
Frequency ν (s ⁻¹)	622.1220307920(6)
Frequency derivative $\dot{\nu}$ (10^{-15} s ⁻²)	-6.51(2)
Frequency second derivative $ \ddot{\nu} $ (10^{-24} s ⁻³)	< 3
Epoch t_0 (JD - 2,440,000)	7700.0000000118(4)
Distance d (kpc)	1.5
Orbital period P_b (s)	33001.91579(9)
Orbital period derivative \dot{P}_b (10^{-11} s s ⁻¹)	-3.9(9)
Orbital eccentricity e	< 4×10^{-5}
Projected semimajor axis x (lt-s)	0.0892262(6)
Reference time of ascending node T_0 (JD - 2,440,000)	7700.0069327(6)

Table 2.7: Timing parameters of the eclipsing binary PSR 1957+20 [105]. Figures in parentheses are uncertainties in the last digits quoted.

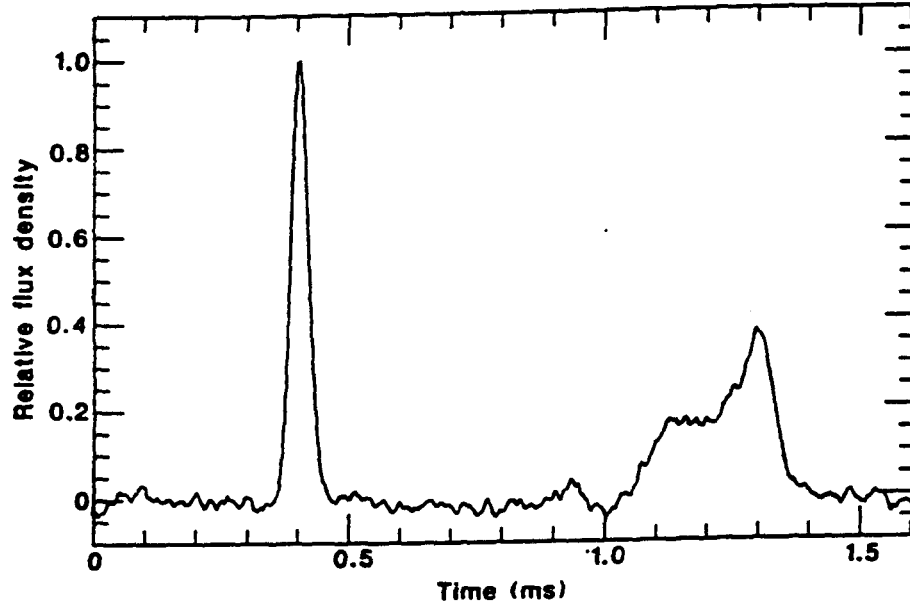


Figure 2.8: Integrated Profile of PSR 1957+20 at 430 MHz [103].

system, these values correspond to phase positions 0.083 and 0.417, respectively. Steady VHE emission from the Lagrangian point L4 has been seen by the Potchefstroom group [107] in their 1988 and 1989 data at energies above 2.7 TeV at the 99.98% CL with a flux of 1.6×10^{-10} photons $\text{cm}^{-2} \text{s}^{-1}$. Evidence of episodic emission of UHE radiation from the pulsar has also been found at the fourth Lagrangian point (L4) by Ooty [108] at $E > 100$ TeV. It occurred on January 30, 1987 at a chance probability level of 1.8×10^{-3} , with a corresponding transient flux of 8×10^{-11} photons $\text{cm}^{-2} \text{s}^{-1}$.

It is suggested that if the cosmic rays are accelerated to PeV energies at or near the pulsar surface then the γ -ray production is expected during the orbital phase 0.2–0.3. Sinha et al. [109] reported a 3.3σ excess (chance probability =

5×10^{-4}) with a flux $= (3.5 \pm 0.8) \times 10^{-13}$ photons $\text{cm}^{-2} \text{s}^{-1}$ above 0.5 PeV during the eclipse in the period 1984–6.

Possible periodic VHE γ -rays, pulsed at the radio period, were found by Brazier [110] during 13 hr of observation in 1988 July. The overall chance probability is 4.1×10^{-3} , not firm enough to assure the detection. Thus there is no compelling evidence that PSR 1557+20 is a pulsating TeV γ -ray source. Further observations are needed to investigate the possible pulsation in the VHE range.

No detection of the steady flux from PSR 1557+20 was observed by HEGRA in their 1989–92 data [93] and 1992–3 data [57]. A flux upper limit at the 90% CL was given to be 8.4×10^{-14} photons $\text{cm}^{-2} \text{s}^{-1}$ above 70 TeV and 3.3×10^{-13} photons $\text{cm}^{-2} \text{s}^{-1}$ above 51 TeV, respectively. The data analysis for steady flux by the Ooty group also showed no indication of significant excess from PSR 1557+20 [108]. They placed a 99% CL upper limit of 4×10^{-13} photons $\text{cm}^{-2} \text{s}^{-1}$ at $E > 100$ TeV. The GREX experiment found no evidence of steady emission during 1986–90 and gave a 95% CL upper limit of 1.73×10^{-14} photons $\text{cm}^{-2} \text{s}^{-1}$ at $E > 920$ TeV [61].

2.5 Theoretical Models

Although there is strong evidence for emissions of VHE/UHE γ -rays from several pulsars, the γ -ray production mechanism is still a mystery. The experimental results can be used to support or reject the theoretical models and their predictions. A brief introduction of current pulsar theory is illustrated as follows.

2.5.1 Outer Magnetospheric Gap Model

The widely considered model of pulsed VHE radiation from fast spinning pulsars is proposed by Cheng, Ho and Ruderman [111, 112]. They use outer magnetospheric gaps to explain the production of VHE γ -rays. In this model, they assume the global current flow patterns through the outer magnetosphere of spinning magnetized neutron stars result in charge-depleted magnetospheric regions (“gaps”) which are expected to exist far from the neutron star. This creates a large electric field \mathbf{E} along the magnetic field lines \mathbf{B} in the gaps. Because $\mathbf{E} \cdot \hat{\mathbf{B}} \neq 0$, such electric field may be able to accelerate charged particles to ultrarelativistic energies. The gap sustains the electron pair production and accelerates e^- and e^+ in opposite directions. The potential drop across the open field lines of the magnetosphere is

$$\Delta V \approx 10^{16} \left(\frac{\Omega}{10^2 \text{ s}^{-1}} \right)^2 \left(\frac{B_s}{3 \times 10^{12} \text{ G}} \right) \left(\frac{R}{10^6 \text{ cm}} \right)^3 \text{ V}, \quad (2.10)$$

where Ω is the rotational frequency, R is the star’s radius and B_s is the surface magnetic field. For the Crab pulsar the potential drop along \mathbf{B} in the outer gap is of order 10^{15} V.

In the gap, e^\pm are oppositely accelerated to extreme relativistic energies by the large electric field until limited by the loss to γ -ray emission by curvature radiation (in the Crab case) or inverse Compton scattering (with the soft synchrotron photons). These energetic photons will partly convert to secondary electron pairs. Synchrotron radiation by these energetic pairs gives rise to the VHE γ -rays and X-rays. The secondary photons will create another generation of electron pairs (tertiary e^\pm). The tertiary pairs mainly lose their energies to soft synchrotron photons. These soft photons are Compton scattered by the primary e^\pm to produce the primary VHE γ -rays.

For the Crab, inverse Compton scattering of secondary e^\pm on the X-rays from the synchrotron (secondary) radiation boosts a significant fraction of X-rays to γ -rays (gap secondary photons). These gap secondary photons, as proposed by Kwok, Cheng and Lau [113], will be boosted by the gap primary positrons from the opposite gap to 10 TeV photons through inverse Compton scattering beyond the light cylinder to produce the unpulsed VHE γ -rays (see Fig. 2.9).

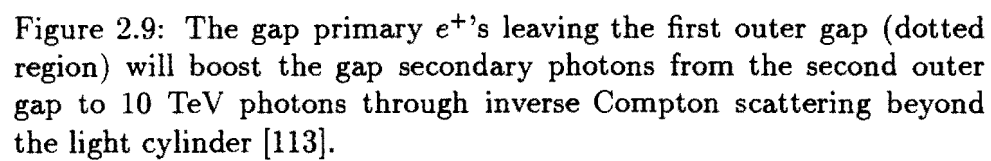
In accreting X-ray pulsars, when the inner part the conducting disk rotates more rapidly than the star, the magnetosphere is charge-separated [114] (see Fig. 2.10). Cheng and Ruderman [114] estimate the maximum potential drop along the magnetic field through the gap is given by

$$\Delta V_{\max} \sim 4 \times 10^{14} \beta^{-5/2} \left(\frac{M}{M_\odot} \right)^{1/7} R_6^{-4/7} L_{37}^{5/7} B_{12}^{-3/7} \text{ V}, \quad (2.11)$$

where M is the stellar mass, R_6 is its radius in units of 10^6 cm, L_{37} is its accretion-powered X-ray luminosity in units of 10^{37} ergs s^{-1} , B_{12} is its surface dipole magnetic field in units of 10^{12} G, and $\beta \equiv 2r_0/r_A$ is twice the ratio of the disk inner radius (r_0) to the Alfvén radius

$$r_A = 3 \times 10^8 L_{37}^{-2/7} B_{12}^{4/7} \left(\frac{M}{M_\odot} \right)^{1/7} R_6^{10/7} \text{ cm}. \quad (2.12)$$

Typical values of β are of order unity. The accelerator gaps above the inner part of the accretion disk can boost positively charged particles to ultrarelativistic energies into the disk. The particles in collisions with the disk material can generate VHE primary γ -rays via photopion production [114, 115, 116]. These primary γ -rays are converted to secondary e^\pm pairs by the local magnetic field and then radiate secondary VHE photons through synchrotron radiation. The combined primary and secondary VHE γ -rays give the observed VHE γ -ray spectrum.



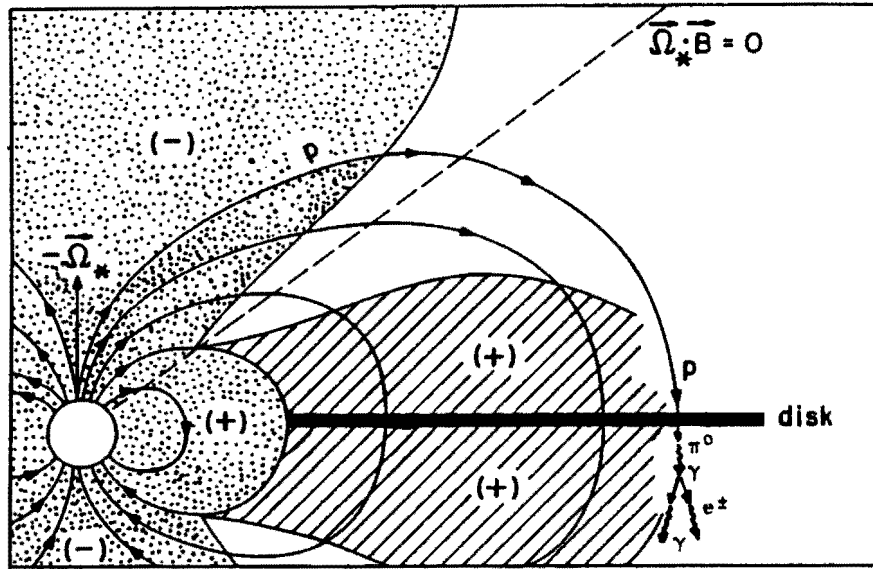


Figure 2.10: Magnetospheres of a spinning neutron star with an aligned magnetic dipole field and a more rapidly spinning conducting disk [116].

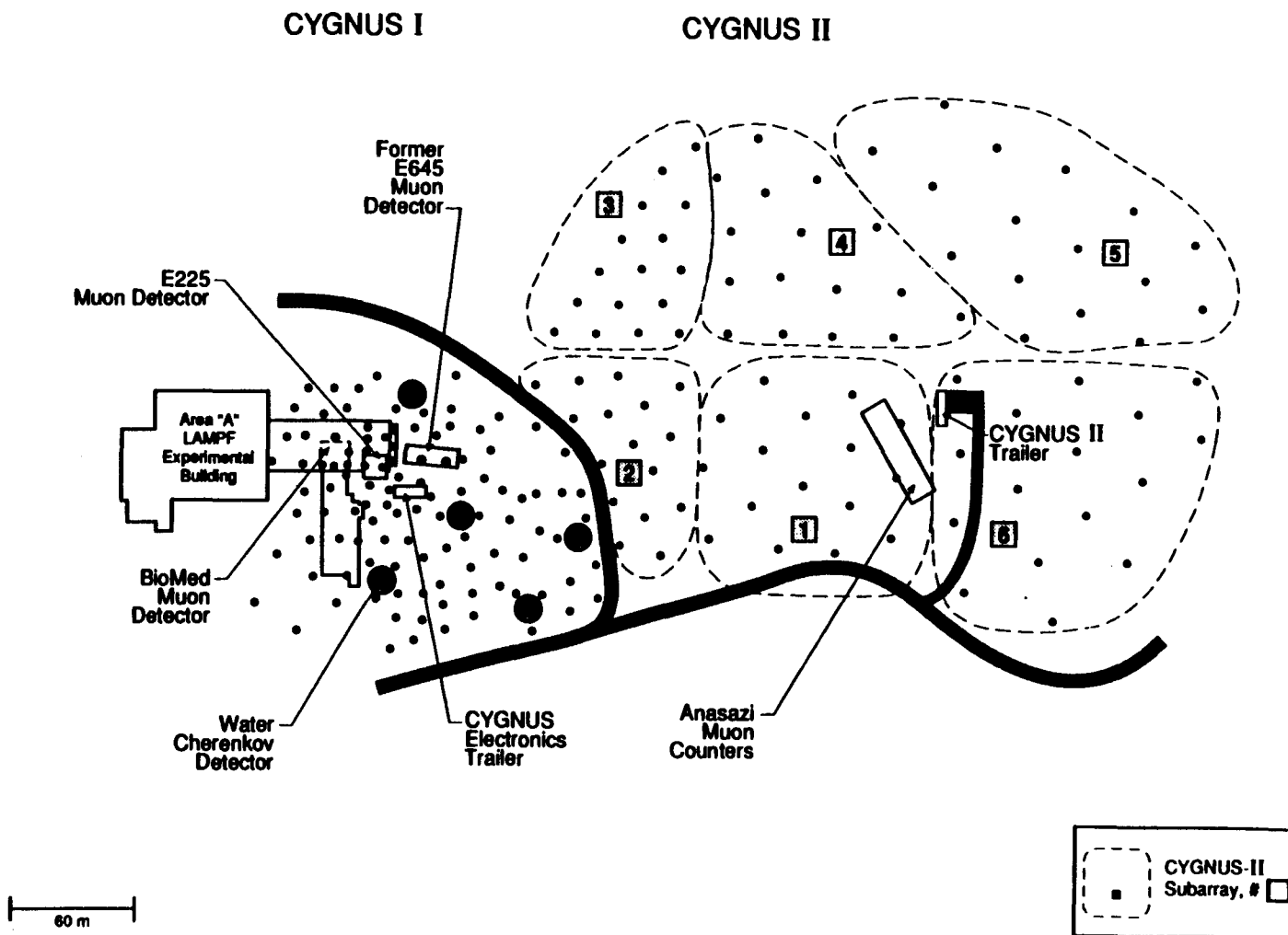
Chapter 3

The CYGNUS Experiment

3.1 Introduction

The CYGNUS extensive air-shower experiment [117] is located at Los Alamos National Laboratory, around the accelerator beam stop of the Los Alamos Meson Physics Facility (LAMPF), in northern New Mexico, USA. It is at a longitude of 106.3° W, a latitude of 35.9° N, and an elevation of 2134 m above sea level, which corresponds to about 800 g/cm^2 atmospheric overburden. It has been upgraded and expanded several times. It currently consists of an Extensive Air-Shower (EAS) array, consisting of the CYGNUS scintillation-counter array and the JASA water-Cherenkov array, and 3 muon detectors. The scintillation-counter array can be further separated into two subarrays: CYGNUS-I and CYGNUS-II. The CYGNUS-II array is in the east of the CYGNUS-I array. Two muon detectors are located in the CYGNUS-I area while the third one is located in the CYGNUS-II area. The JASA array consists of five backyard style pools and they are distributed within the CYGNUS-I area. The locations of the array and the muon detectors are shown in Fig. 3.1.

Figure 3.1: Current configuration of the CYGNUS experiment.



Only the data acquired by the CYGNUS-I array and the E-225 muon detector and by the JASA array are used in this analysis. The CYGNUS-I array are described in the following sections. The JASA array will be described in a separate chapter.

3.2 The Scintillation EAS Array

The CYGNUS-I EAS array began operation on April 2, 1986, originally with 50 scintillation counters and one muon detector. It has undergone several upgrades to its present size of 108 counters. These counters are deployed around the E-225 detector, which is being used as one of the muon detectors (see Section 3.5), and are scattered around the LAMPF buildings and hills at different altitudes. The region they cover is $\sim 22,000 \text{ m}^2$ in size.

Each scintillation counter contains a $\sim 1\text{-m}$ diameter piece of $\sim 10 \text{ cm}$ thick plastic scintillator sealed in a light-tight, cone-shaped, fiberglass enclosure. The scintillator is viewed from the top by a single photomultiplier tube (PMT). A schematic is given in Fig. 3.2. The fiberglass container is white on the outside to reduce the effect of temperature fluctuations and is white on the inside to maximize the light collection by the PMT. The distance between the PMT and the scintillator is $\sim 0.7 \text{ m}$ to reduce the scintillation light collection time spread. Amperex 2262 PMTs, with a 2-inch diameter and a risetime of $< 2 \text{ ns}$, are used.

The spacing of the detectors ranges from 7 m near the center of the array to 20 m near the edges. The spacing of the counters is graded so that the counters can trigger on relatively small air-showers near the center of the array and still have a large collection area for large showers. The trigger is a simple multiplicity

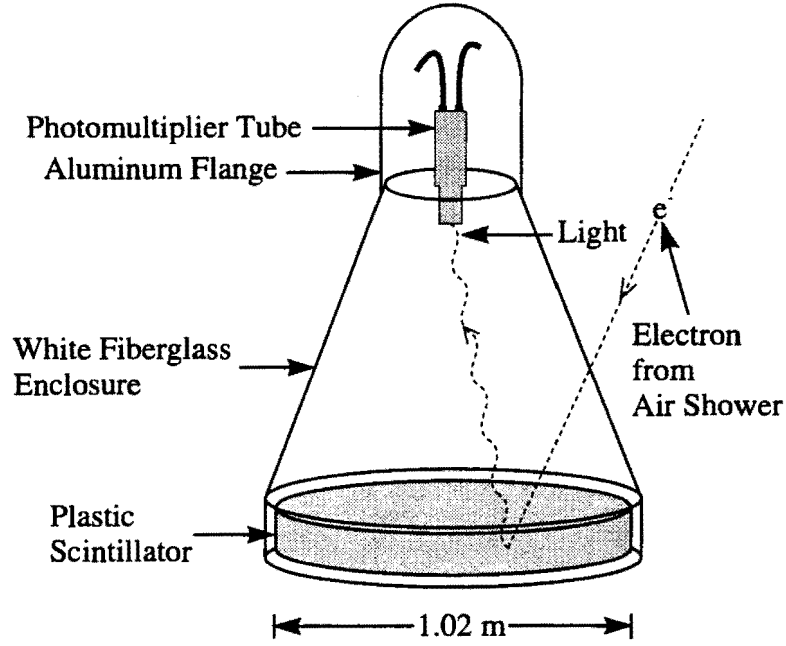


Figure 3.2: Schematic view of a CYGNUS scintillation counter.

requiring ≥ 20 counters firing in a 300 ns time window. The long coincidence window is needed to allow for the showerfront of a large-angle (relative to the zenith) shower event to propagate across the whole array.

A 0.25 cm thick lead sheet was placed on the outside of each scintillation counter in June 1989. The lead sheet is at about 60° to the horizontal, whose thickness corresponds to ~ 1 radiation length for a vertical particle. The shower γ -rays are converted in the lead into e^- and e^+ pairs that will register a signal in the scintillator, thus increasing the sensitivity to the detection of showers.

The median detected proton energies can be determined from Monte Carlo simulation and are found to be ~ 100 TeV for CYGNUS-I assuming that the energy spectrum of the protons is the same as that of the cosmic rays (integral

spectrum index $\alpha = 1.7$). The angular resolution is $\sim 0.7^\circ$; it can be determined by looking at the shadowing effect of the ultrahigh-energy cosmic rays blocked by the Moon and the Sun [118]. The current trigger rate is ~ 3.5 Hz for CYGNUS-I; approximately $\sim 5 \times 10^8$ CYGNUS-I air-shower events have been accumulated to date. See Table 3.1 for a summary of the CYGNUS experiment.

An electronic trailer is located at the middle of the CYGNUS-I array. All CYGNUS-I counters are connected through RG-58A cables (about 70–150 m long) to the trailer. The data acquisition system in the trailer automatically processes the signals from each counter and store the data on the computer disks and magnetic tapes.

3.3 Data Acquisition System

NIM and CAMAC systems are used in the Data Acquisition System (DAQ). The counter output signal is passively split into 1/7th and 6/7th of the original input. The 1/7th signal is delayed and fed to a CAMAC 10-bit analog-to-digital converter (ADC). The 6/7th part is amplified 10 times and directed to a discriminator. The discriminator is set at a low threshold of ~ 0.1 minimum ionizing through-particle in the scintillator. The low trigger threshold reduces the time slewing due to different pulse heights and shapes. One of the two discriminator outputs is delayed and goes to a CAMAC 11-bit time-to-digital converter (TDC) stop input, while the other goes directly to a multiplicity logic unit (MLU). The MLU output is discriminated at a level of ≥ 20 CYGNUS-I counters in coincidence. A trigger signal generates a start signal for the TDC modules and the ADC gates and starts the event read-out by the DAQ. Fig. 3.3 shows a simplified diagram of the electronics system. The

CYGNUS EXPERIMENT

Location: Los Alamos, NM (106.3° W, 35.9° N)
 Elevation: 2134 m (800 g/cm²)

	<u>CYGNUS-I</u>	<u>CYGNUS-II</u>
Number of Detectors:	108 (1 m ² scintillators) + 5 water pools (42 m ² each)	96
Area of Array:	22,000 m ² (Graded spacing)	63,000 m ² (Graded spacing)
Muon Detector Area:	90 m ²	70 m ²
Event Rate:	~ 3.5 Hz	~ 1.8 Hz
Median Detected		
Proton Energy:	100 TeV	240 TeV
Angular Resolution:		~ 0.7°
Period of Operation:	4/86 – Present	3/90 – Present
# of Events Acquired:	~ 5 × 10 ⁸	~ 2 × 10 ⁸

Table 3.1: Summary of the CYGNUS experiment.

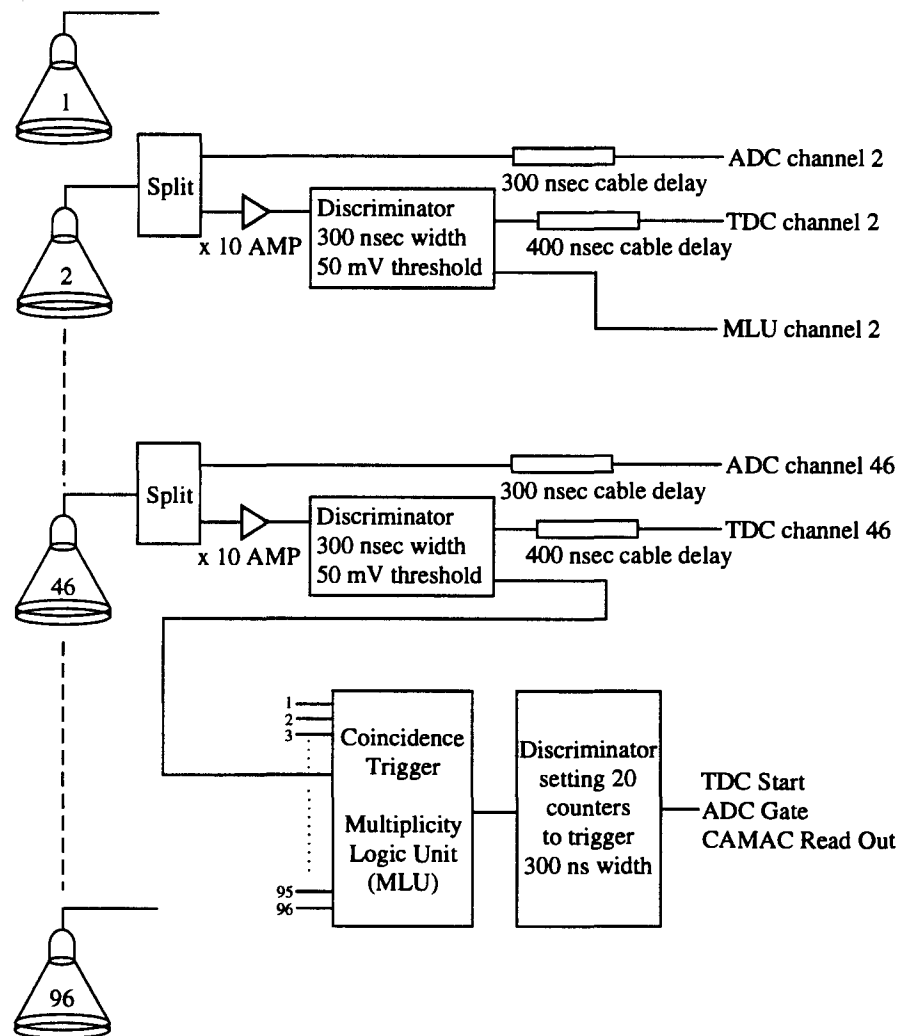


Figure 3.3: Simplified diagram of the data acquisition system.

ADCs and TDCs then start digitizing the charges and times for each counter and they are recorded at the end.

The event times are registered by two clock systems — the WWV clock and the Global Positioning System (GPS) clock. The GPS clock is latched whenever there is an event trigger, while the DAQ reads out the WWV clock after the event has been processed by the electronics. The WWV uses the radio signal transmitted from the station at the National Bureau of Standards in Boulder, Co., USA. Its absolute timing accuracy is ~ 0.5 ms. The GPS is a world-wide navigation system using a constellation of orbiting geosynchronous satellites. Four satellites can be viewed from any place on earth. They transmit time and orbital position data from which the receiver's 3-dimensional position can be obtained. Once the user's geodesic location is determined, tracking only one satellite is sufficient for a full-accuracy time measurement. The GPS clock system has an accuracy up to 500 ns.

The pulse-height and timing information from the CAMAC system are read out by a DEC microVAX-II computer. The deadtime is $\sim 10\%$. The output data are collected in *runs*. A run usually lasts for a few hours. The run change is avoided when a potential source (e.g., CYGNUS X-3) is near the zenith so the point source can be observed without interruption.

The data are written out to 8-mm tapes when a run is completed. They are also “replayed” by a separate computer into useful information and stored in different file formats. For example, a DAT format file has the pulse heights (in particle numbers) and arrival times (in nanoseconds) of all the counters and the processed information such as the *core* location (the location of the primary particle

on the ground if there had been no interaction with the atmosphere), the event time, the incident direction of the shower, the number of muons, etc. The CMP format file stores the replayed information except that of individual counters. There are also SUN/MOON data files which have the same information as DAT files, but the SUN/MOON files only keep the events coming from near the SUN/MOON directions for use with angular resolution studies. The replayed data files are also stored on 8-mm tapes. Only the CMP files are stored on the hard disks for handy analysis.

There is also an online monitoring system which generates histograms such as the frequency of each detector being hit, the ADC and TDC distributions, the event rate, the number of counters fired, the pressure, the temperature, etc., to monitor the performance of individual detectors and electronic channels and to detect any anomalies.

3.4 Calibration

The reconstruction of the shower plane requires subtracting the ADC (TDC) pedestals (timing offsets) from the ADC (TDC) counts and converting the ADC (TDC) values into the number of equivalent minimum ionizing through particles (nanoseconds). Therefore, every counter needs to be calibrated to determine its pedestal and conversion factor. The calibration uses two overlapping scintillators, each $20\text{ cm} \times 20\text{ cm}$. Each scintillator is viewed by a PMT through a light pipe. The two scintillators are optically isolated from each other and are configured together as a single paddle. Using two scintillators allows coincidences to be used to register through-going muons with only a small accidental contribution.

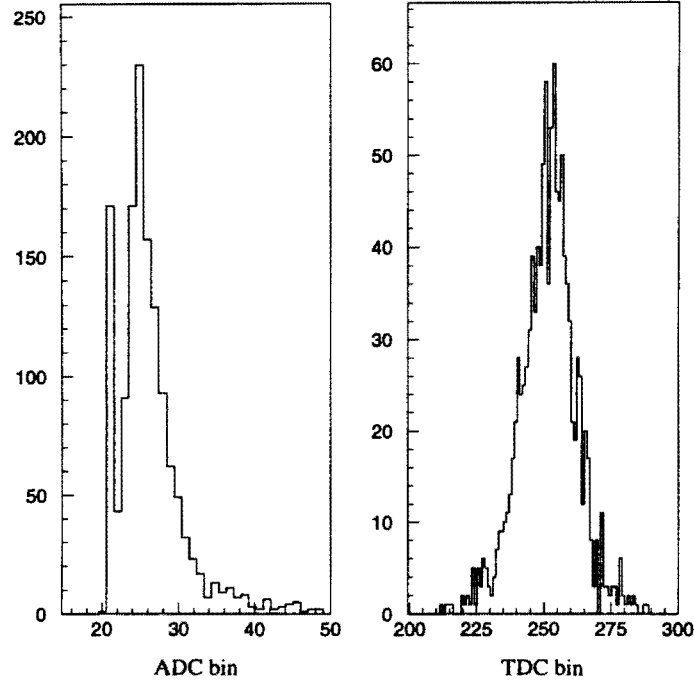


Figure 3.4: Sample ADC and TDC histograms.

The paddle is put under each array counter in turn during the calibration process. When a charged particle (most likely a muon) penetrates the counter and traverses the paddle, the coincidence of the two paddle scintillators produces a trigger signal to start collecting the ADC and TDC values for the array counters. Sample ADC and TDC distributions are shown in Fig. 3.4. One can clearly see the pedestal and single-particle peak in the ADC histogram. One particle typically corresponds to ~ 5 ADC counts. The ADC pedestal is also obtained from triggers randomly generated by the computer at the beginning of each run. Because of the timing drift caused by the temperature change during a day, the paddle is periodically cross-checked with some reference counters.

The drifts introduced by the conversion electronics, changes in the temperature, changes in the lengths of the cables, replacement of a electronic channel, etc., suggest that calibrations be taken a few times a year. The ADC pedestals (APEDs), ADC conversion factors (ACONs) and TDC conversion factors (TCONs) are quite stable from calibration to calibration, provided that the electronics channels and the high voltage settings are kept unchanged. The TDC timing offsets (TPEDs) from the current calibration values are compared with those from the previous calibration values to check the timing stability. The calibration values of the TPEDs drift ~ 1.5 ns (rms) in the course of ~ 6 months between calibrations. Once the ADC and TDC offsets and conversion factors are determined, they are stored on the disk and they are used to reconstruct a shower event. See Sec. 3.6 for more detailed description.

The TPEDs are also adjusted by the “pre-play” process in the beginning of each run. In the run, 60000 events of the first 240000 events (in increment of 4 events) are processed using the latest calibration values to fit the shower plane for each event. The averaged timing deviation of each counter from the fitted plane is added to its calibrated TPED. Then the new TPEDs are used to fit all the event in that run.

3.5 Muon Detectors

UHE γ -ray initiated air-showers are expected to have much fewer muons than hadron induced showers. Thus a muon detector can discriminate the background (hadronic) showers from the signal (γ -ray) showers by looking at the muon content in the showers. Since muons are much more penetrating than electrons, photons

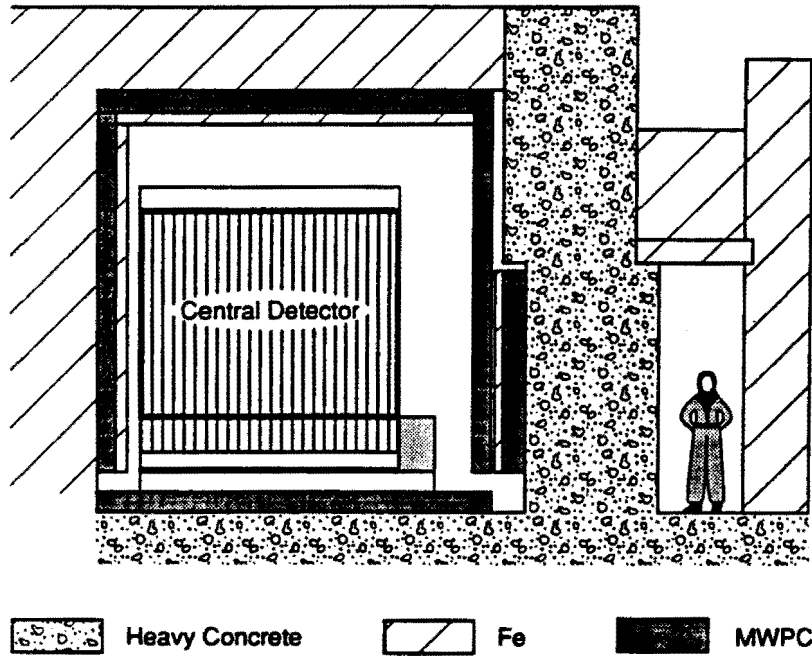


Figure 3.5: A side view of the CYGNUS E-225 muon detector.

and hadrons, a heavy shield material is needed on the outside of the muon detector to stop the soft component in a shower.

The E-225 muon detectors formerly served as an anticoincidence shield for the LAMPF E-225 neutrino experiment [119, 120]. It is located at the center of the CYGNUS-I array. Fig. 3.5 gives a sketch of the E-225 detector. The central detector consisted of multiple layers of scintillator and flash chambers in a room of $3\text{ m} \times 3\text{ m} \times 3.6\text{ m}$.

The central detector was operated for both the CYGNUS experiment and for the E-225 experiment at the early stage of the CYGNUS experiment, and for the CYGNUS experiment alone after the termination of E-225 until it was

dismantled in February 1988. Layers of multiwire-proportional counters (MWPCs, each typically 20 cm wide, 2.5 cm thick and 5.4 m long), forming a cube of 6 m on each side, was used by the E-225 experiment as the veto shield. The MWPCs have been operated continuously by the CYGNUS experiment to estimate the number of muons in an air-shower. The muon detection area is roughly 44 m^2 for muons incident with the zenith angle distribution measured for EAS showers. Iron and concrete shielding is placed on the outside of the entire system, with at least 800 g/cm^2 of material on all sides. The lowest energy for a muon to penetrate the walls from any direction is roughly 2 GeV. The muon data are read out for each CYGNUS trigger.

3.6 Shower Reconstruction

An EAS array does not directly measure the primary particle. The information about the primary can only be inferred from the measurements of the shower properties, namely the location of the shower core, the incoming shower direction, the shower size and age, and the muon content. The recorded pulse-height and timing data, together with the aid of Monte Carlo simulations, are used to calculate the above quantities.

The location of the shower core is obtained by fitting the registered charges of all the struck counters to a 2-dimensional Gaussian distribution. Another way to get the core position involves fitting the measured electron lateral distribution to the Nishimura-Kamata-Greisen (NKG) function [121] with 4 parameters (the x position of the core, the y position of the core, the shower size, and the shower age) [122]. However, performing a 4-parameter fit to the NKG formula requires

extensive use of the computer CPU time. Although the Gaussian fitter has larger core-location error than the NKG fitter, Monte Carlo simulations indicate no noticeable difference in the average angular resolution if the better core location is used [122].

The core fitting algorithm does not always successfully find the core location, in most cases because the distribution of counter pulse areas is flat. If the core fitter fails to find an acceptable core position ($\sim 8\%$ of the CYGNUS events), the core position is assigned to the location of the hottest (largest pulse-area) counter. Monte Carlo studies reveal that the fitted core location agrees with the true core location to less than 5 m when the core lies near the center of the array and less than 8 m when the core lies close to the boundary of the array. The error is larger when the core is located outside the array ($\sim 16\%$ of the triggered events).

The most important aspect of searching for the directional excess from a point source is how precise we can reconstruct the direction of the incident primary particle. The direction is found from the arrival times of the shower particles at the individual detectors. The angular resolution is limited by the intrinsic statistical fluctuations developed in the showering process when the primary hits the atmosphere and creates the secondary particles. The measured timing deviates more from the shower plane as the distance gets farther away from the core axis, due to the increasing thickness of the shower plane and the decreasing density of the secondaries.

The shower plane is slightly curved. Data and Monte Carlo results show that the average time delay of the particles from the showerfront can be parameterized according to the pulse height and the distance from the shower core [122].

Detectors	“Slewing” (ns)	“Sampling” (ns)
CYGNUS-I without lead	$\frac{2.2}{\sqrt{N}} + 1.8e^{-0.05N}$	$0.12R_m N^{-0.25}$
CYGNUS-I with lead	$\frac{2.2}{\sqrt{N}} + 1.8e^{-0.05N}$	$0.10R_m N^{-0.28}$
CYGNUS-II with lead	$\frac{2.2}{\sqrt{N}} + 2.4e^{-0.05N}$	$0.10R_m N^{-0.28}$
SIMULATION CYGNUS-I without lead	0	$0.15R_m N^{-0.32}$

Table 3.2: Parameterizations of the showerfront curvature correction, where N is the pulse height of the counter in terms of particle number and R_m is the distance of the counter from the shower core in meters [122].

The parameterizations are given in Table 3.2. The first portion of the curvature correction is believed to be due to electronic slewing which only depends on the pulse height, and the second part is believed to be due to sampling and the “true” showerfront curvature. Both terms are subtracted from the measured arrival time to get a flat showerfront.

The thickness of the shower plane can also be parameterized [122] in a similar manner (see Table 3.3). The radius-independent term corresponds to some intrinsic minimum width that is partially dependent on the PMT, the showerfront sampling and shower fluctuations, and the radius-dependent term accounts for the increasing thickness from the shower core. The thickness is given in terms of σ (ns), which represents 68% of the timing measurements. The addition of both terms gives the σ , and therefore the weight ($= 1/\sigma^2$), used to fit the curvature-corrected showerfront.

A χ^2 -minimization method is used to fit the arrival direction (normal to the

Detectors	Radius-Independent (ns)	Radius-Dependent (ns)
CYGNUS-I without lead	$0.95 + 2.3e^{-0.62N}$	$(0.0064 + \frac{0.022}{\sqrt{N}})R_m$
CYGNUS-I with lead	$0.54 + 2.64e^{-0.75N}$	$(0.016 + \frac{0.013}{\sqrt{N}})R_m$
CYGNUS-II with lead	$0.89 + 5.5e^{-0.81N}$	$0.018R_m$
SIMULATION CYGNUS-I without lead	$0.80 + 2.8e^{-0.70N}$	$(0.0083 + \frac{0.024}{\sqrt{N}})R_m$

Table 3.3: Parameterizations of the showerfront thickness, where N is the pulse height of the counter in terms of particle number and R_m is the distance of the counter from the shower core in meters [122].

shower plane) of the shower. The χ^2 function is given by

$$\chi^2 = \sum_n w_n (c(t_n - t_0) + \hat{i}x_n + \hat{j}y_n + \hat{k}z_n)^2, \quad (3.1)$$

where \hat{i} , \hat{j} , and \hat{k} are the three components of a unit vector normal to the shower plane, w_n is the weight assigned to the n th counter, c is the velocity of light, t_n is the corrected time of the n th counter, t_0 is the absolute arrival time of the shower, and (x_n, y_n, z_n) is the location of the n th counter. The sum is performed over all struck counters.

The weights $w_n = 1/\sigma^2$ used in the timing fit take into account the larger timing fluctuations for counters with a small number of particles passing through them and for counters far away from the core.

Chapter 4

JASA Water-Čerenkov Array

As described earlier, when an ultra-relativistic charged particle travels through a medium, it generates cones of Čerenkov photons along the track if its speed exceeds the local speed of light in that medium. Therefore, the shower particles may be detected by means of their Čerenkov radiation. The material used for the detection medium can be any material that is transparent to the Čerenkov light, yet it should be affordable. Water is a good medium for this purpose. The motivation for incorporating the water-Čerenkov detectors is that they have a large sensitive surface area to the shower particles such as electrons, positrons, muons and high-energy photons (see Sec. 4.3), and the γ -rays should have better showerfront timing than the other shower particles because of the larger amount of γ -rays. Therefore, they can improve the angular resolution (by a factor ~ 2 as predicted by Monte Carlo simulations) of the CYGNUS experiment. Furthermore, the water-Čerenkov detectors will not be affected by the weather conditions, just like the air-shower detectors, and can be operated simultaneously with the scintillator array at all times.

4.1 Installation

A prototype of the backyard-style swimming pool was installed near the CYGNUS-I trailer in the summer of 1990. Ten PMTs (8-inch Hamamatsu PMTs, model R1408) were placed on the bottom of the pool for testing. In summer 1991, four more pools were built around the existing one. Seven 10.4-inch PMTs (model BURLE C83061E, a 12-stage Quantacon PMT with a transit time spread of < 2.3 ns (FWHM) at the single photoelectron (PE) level [123]) were placed on the bottom of each new pool. Six of the PMTs were arranged in a hexagon surrounding a central PMT. The existing prototype pool was also equipped with the same PMTs and with the same arrangement. Each pool is ~ 2.3 m deep (~ 2 m of water above the top of the PMT) and 7.3 m across (~ 42 m² surface area). The diagram of the configuration of a pool is given in Fig. 4.1. Also see Fig. 3.1 for the pool positions in the EAS array. The pools are separated by ~ 60 m from each other. They are denoted as Center, North, East, South and West pools according to their relative geographic locations.

Black covers and insulation were put on the top and the outside of each pool to eliminate light leaks and to keep the water from freezing in the winter. Black liners were also used on the inside of the pools to reduce the light reflecting from the walls and bottoms for better showerfront timing.

4.2 Water Purification

The water in each pool is continuously filtered by a sand trap (filled with charcoal) to filter out the chlorine and by a $0.5\text{ }\mu\text{m}$ filter (except in the Center pool,

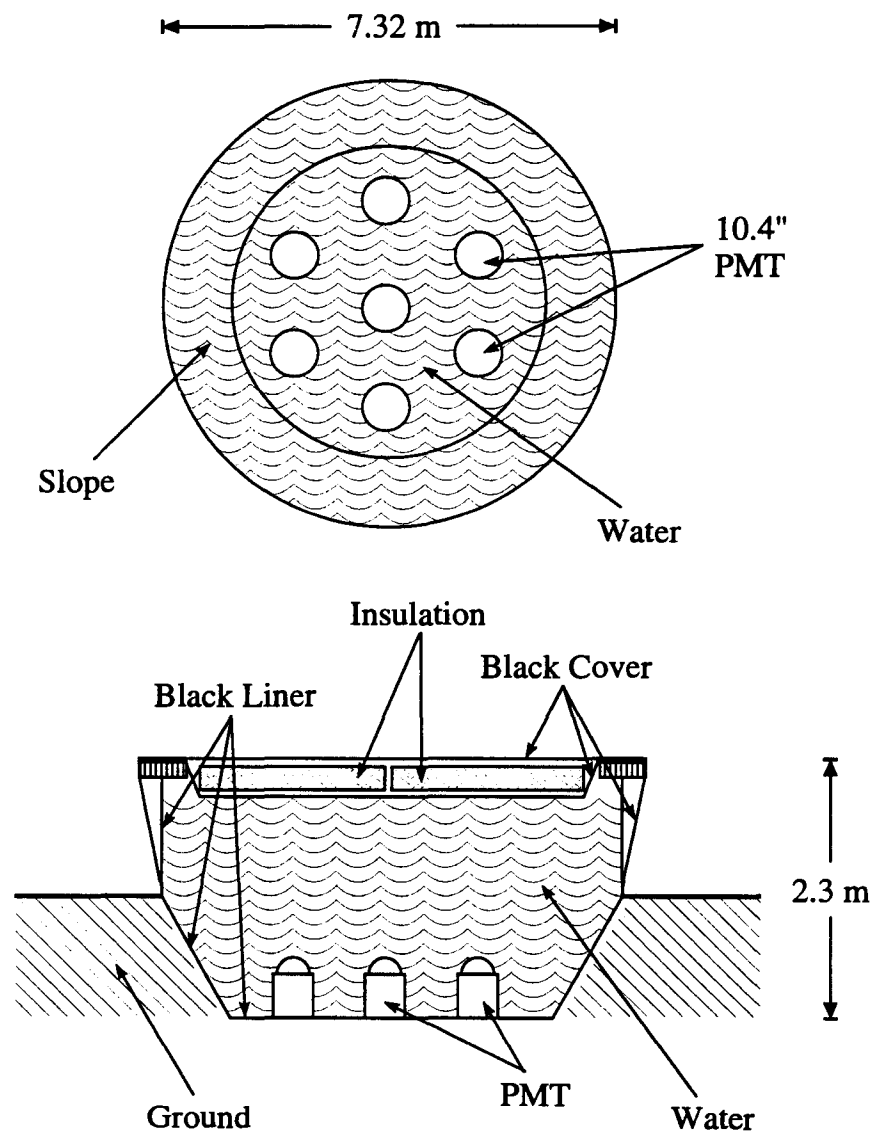


Figure 4.1: Schematic diagram of a water-Cherenkov detector and the arrangement of the PMTs.

which is filtered by an additional filter). The Center pool uses UV light to kill the organisms growing in water while the other four pools use ozonators. The water is also periodically tested to ensure the transparency to the Čerenkov light. A spectrophotometer is used to measure the absorptivity of the pool water. First the purified (filtered and de-ionized) water is filled in a 10-cm long cylindrical crystal cell to calibrate the absorptivity with the purified water in another crystal cell. A beam at a pre-set wavelength passes through the center of each cell and the difference in absorptivity is zeroed. The beam continuously scans from about 300 to 900 nm. After the calibration process is finished, one can measure the absorptivities at certain wavelengths. The absorptivities of the purified water to purified water at different wavelengths are first taken. Then one of the cell is replaced with the sample pool water and the absorptivities are measured at the same wavelengths. Finally the sample water is replaced with the purified water and the absorptivities are again measured. The two measurements for the purified water to purified water at a given wavelength are averaged to reduce the uncertainty caused by the electronics drift. The difference of measured absorptivities between the sample water and the purified water has the following relation with the intensity of the beam:

$$I = I_0 \times 10^{-X_{abs}}, \quad (4.1)$$

where I_0 is the original intensity of the beam and X_{abs} is the difference of measured absorptivities at a given wavelength. The attenuated intensity can also be expressed as

$$I = I_0 \times e^{-L_{cell}/L_{att}}, \quad (4.2)$$

where L_{cell} is the length of the cell and L_{att} is the attenuation length of the water sample. Equating Eqs. 4.1 and 4.2 one yields

$$L_{att} = \frac{L_{cell}}{X_{abs} \ln 10}. \quad (4.3)$$

Given $L_{cell} = 0.1$ m, the attenuation length is then

$$L_{att} = \frac{4.343 \times 10^{-2}}{X_{abs}} \text{ m}. \quad (4.4)$$

By differentiating Eq. 4.3 with respect to X_{abs} one can show that the error of the attenuation length is

$$\Delta L_{att} = -\frac{\Delta X_{abs} L_{cell}}{X_{abs}^2 \ln 10}. \quad (4.5)$$

The precision of the absorptivity measurement is $\Delta X_{abs} = 0.001$, therefore,

$$\Delta L_{att} = \frac{4.343 \times 10^{-5}}{X_{abs}^2} \text{ m}. \quad (4.6)$$

A sample plot of the attenuation length as a function of wavelength is shown in Fig. 4.2.

4.3 Detection of Shower Particles

Incoming γ -rays undergo either Compton scattering or pair production in the water. The resultant electrons (and positrons), as well as the other incident charged particles, undergo multiple scattering as they propagate through the pool. The average Čerenkov photon number emitted per track length of the charged particle is calculated to be 57 PEs/cm (see Appendix A), convoluted with the quantum efficiency of the PMT.

Most shower particles do not hit the BURLE PMTs directly, as the area occupied by the PMTs amounts to only about 1% of the surface area. However,

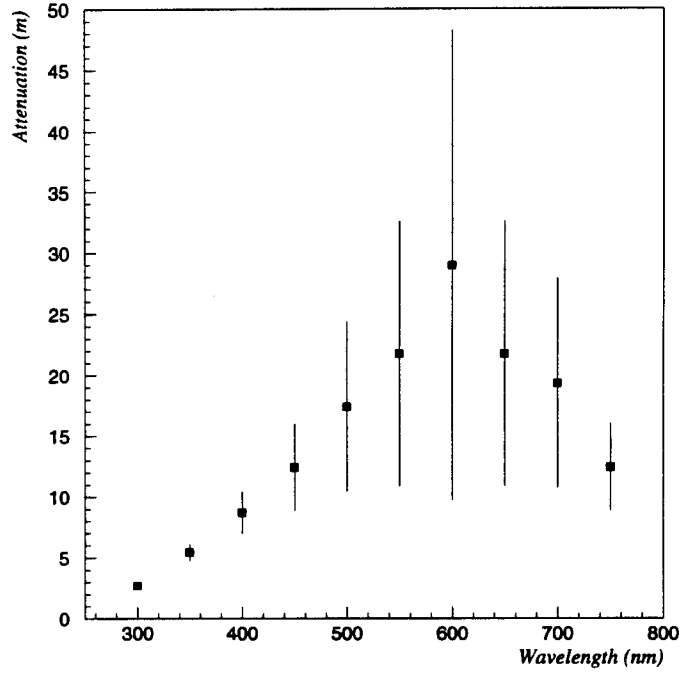


Figure 4.2: A sample test result of the attenuation length vs. photon wavelength for the water of the Center pool.

because the large number of the secondary Čerenkov photons produced by a shower particle along its track and because the Čerenkov angle ($\theta_c = 41.2^\circ$ in water for $\beta \simeq 1$) and the multiple scattering help spread out the light, it is likely that more than one PMT in the pool is hit by the Čerenkov photons of the shower particle. Fig. 4.3 shows the frequency of hits per tube versus the number of tubes hit for a sample run.

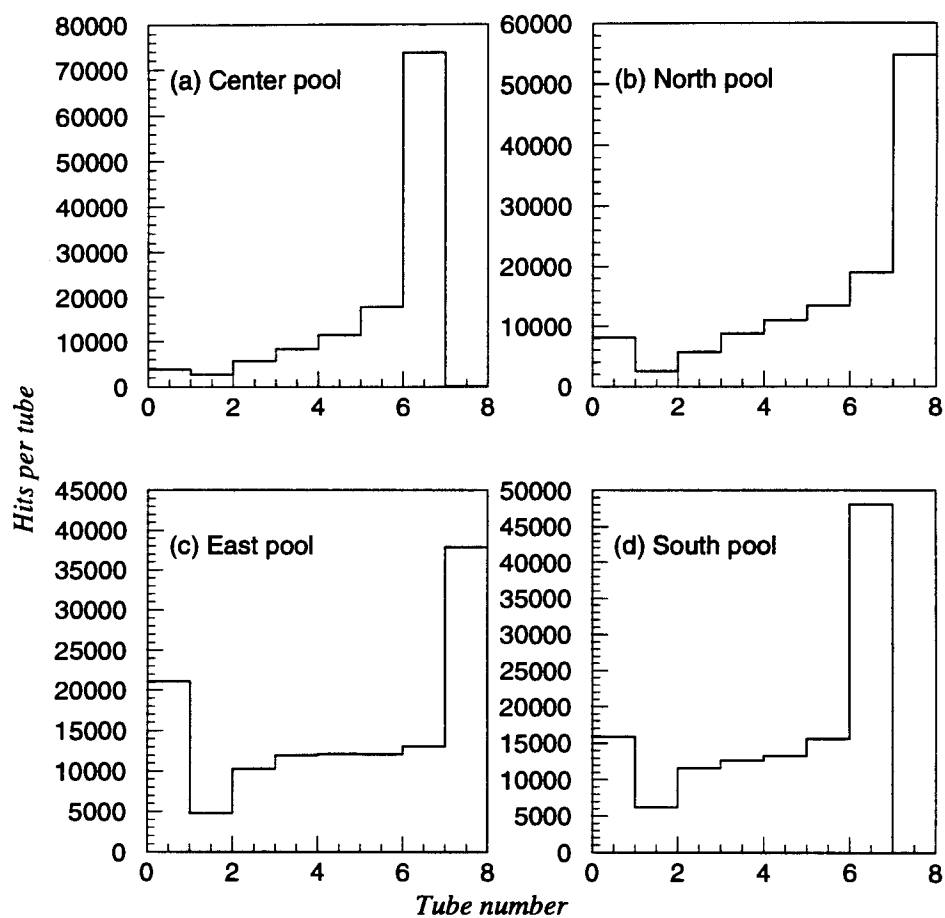


Figure 4.3: PMT multiplicity spectrum for pools. One PMT is off or dead in the Center pool and in the South pool, and the West pool is off for the sample runs.

4.4 Electronics

The electronics for the pool is similar to the CYGNUS electronics. However, the pools do not participate in the trigger determination, therefore, the energy threshold of the CYGNUS experiment remains the same. Fig. 4.4 shows a simplified layout of the pool electronics. The Argonne Pulse Laundry has one 1:1 output, one 1:1/10 output and one discriminator output for each input pulse. The pools have their own ADC gates (150 ns wide) because most BURLE PMT pulses will integrate to zero over the time window of the CYGNUS ADC gate. This is because that the anode of the PMT is positively charged, and a capacitor is necessary to block the high voltage at the signal pick-up. If the time window is large, it will integrate over the pulse area and the overshoot area and the net result will be zero. The PMT pulses are discriminated at 1.5 mV (~ 0.1 PE) and the singles rates are ~ 10 KHz. A Pool is only read out when the scintillation-counter array triggers and when there are at least 2 PEs (sum of the 7 tubes) registered in the PMTs.

4.5 Calibration

No hardware calibration has been carried out for the time being. A software calibration is employed instead. The ADC pedestals (APEDs) and conversion factors (ACONs) are directly obtained from the histograms of the ADC counts (similar to the ADC histogram in Fig. 3.4). For determining the timing offsets (TPEDs), the shower plane is first fitted using the scintillation counters only. Then the TPEDs of the PMTs are taken as their timing residuals from the fitted shower plane.

4.6 Curvature and Sampling Corrections

The showerfront and the width of the shower plane measured by the water-Čerenkov detectors which detect the secondary Čerenkov photons are different from that measured by the scintillation counters which directly sample the shower particles. This is due to the fact that the γ -rays produce electron-positron pairs with the pair opening angles, the charged particles experience multiple scattering in water, and the Čerenkov photons are produced at characteristic angles. To get the corrections, the showerfront is first fitted by the scintillator array. Only showers coming from near the zenith are selected to minimize any fitting errors. The timing differences between the showerfront and the arrival times with the pool PMTs are recorded and divided into radial bins from the core. In each radial bin, the timing differences are further separated into different pulse-height bins. Therefore, the averaged timing differences as a function of radius and pulse height are represented by a 2-dimensional array. It is then fitted to an appropriate form. The curvature timing correction is parameterized as [124]

$$T(R_m, N_{\text{PE}}) = 8.35 + 0.0475R_m^{1.214} - (1.878 + 0.0024R_m^{1.475}) \times \ln N_{\text{PE}} \text{ ns}, \quad (4.7)$$

where R_m and N_{PE} are the distance (in meters) from the shower core and the pulse height (in PEs), respectively. The thickness (in ns) of the shower plane is parameterized as [125]

$$\sigma = \begin{cases} 0.8 + \frac{3.24}{\sqrt{N_{\text{PE}}}} - 6.56 \times 10^{-3}R_m + 1.916 \times 10^{-4}R_m^2 & \text{if } N_{\text{PE}} \leq 30 \\ 1.3 - 6.56 \times 10^{-3}R_m + 1.916 \times 10^{-4}R_m^2 & \text{otherwise} \end{cases} \quad (4.8)$$

4.7 Shower Reconstruction

The reconstruction of the shower direction with the pool data is similar to the CYGNUS procedure. First the shower core location is found using the scintillation counter array, as described in Sec. 3.6. Then the TPEDs are subtracted from the TDC values of the pool tubes, and the pool's curvature and sampling corrections are applied to the pool data. The fitting procedure is similar to that described in Sec. 3.6.

4.8 Angular Resolution

Moon shadows are studied to find the angular resolution of the water-Čerenkov array. The preliminary result gives an angular resolution of 0.42° [126]. (The CYGNUS array has an angular resolution of $\sim 0.7^\circ$.) If a cut which requires a minimum of 15 PMTs distributed among at least 3 pools is applied to the same MOON data, the angular resolution improves to 0.32° [126].

4.9 Pool Simulation

A Monte Carlo simulation program has been developed to simulate the pool conditions. The JASA simulation (POOLSIM) is an extension of the CYGNUS simulation (CYGSIM) [122] which in turn uses the EAS showers generated by SHOWERSIM [127]. A detailed description of CYGSIM can be found in Biller [122]. The brief description of POOLSIM is described as follows.

POOLSIM is called after the EAS showers trigger the CYGNUS-I array in

CYGSIM. The shower particles from CYGSIM are thrown on the top of the JASA pools. Five pools and seven PMTs in each pool are distributed according to their surveyed locations. For each pool, the surface is divided into several grids in which the shower particles are randomly distributed. The number of particles hitting a given grid is determined for each particle type by interpolating the particle density \times grid area, as obtained from CYGSIM. In water, a photon undergoes either pair production to produce electron-positron pairs or Compton scattering and subject to further pair production or Compton scattering, while the charged particles all undergo multiple scattering. The Čerenkov photons are emitted with respect to the track in a cone whose half-angle is described according to Eq. 1.2. The number of Čerenkov photons per track length is calculated to be 57 photons/cm when the quantum efficiency of the PMTs is included in the integration of Eq. A.4. The quantum efficiency (QE) of the PMTs is a function of wavelength and is about 27% at 380 nm, as given by the manufacturer's specifications. The energy loss rate of the particles and the attenuation length of water are taken to be 1.8 MeV/g cm⁻² and 6 m, respectively. There is no reflection on the inner walls and bottoms of the pools in the program. After all the particles have produced their Čerenkov photons, the number of photoelectrons in each PMT is randomized according to the Poisson distribution. The earliest time recorded by the PMT is also saved. The resulting lateral distribution of PEs is about twice higher than the real distribution. Although the reflection of the PMT glass is not included in the program, it is estimated to be only less than 1%. The reasons which cause the discrepancy can be due to (1) the real QE is less than the specifications, or (2) the earth's magnetic field lowers the PMT's sensitivity. The effect of the magnetic field

relates to the orientation of the dynode structure with respect to the field itself. The PMT performance can drop down to as low as 50% at 250 mG and to as low as 10% at 500 mG, with respect to the situation without magnetic field [128]. This is partly due to the effect of the magnetic field in enhancing the number of secondary electrons skipping some stages of the multiplier chains and partly to the photoelectrons which do not impinge on the first dynode. Hence it is reasonable to assume that the performance of each PMT is degraded by about half to be in accord with the observation. The resulting PE lateral distribution is shown in Fig. 4.5.

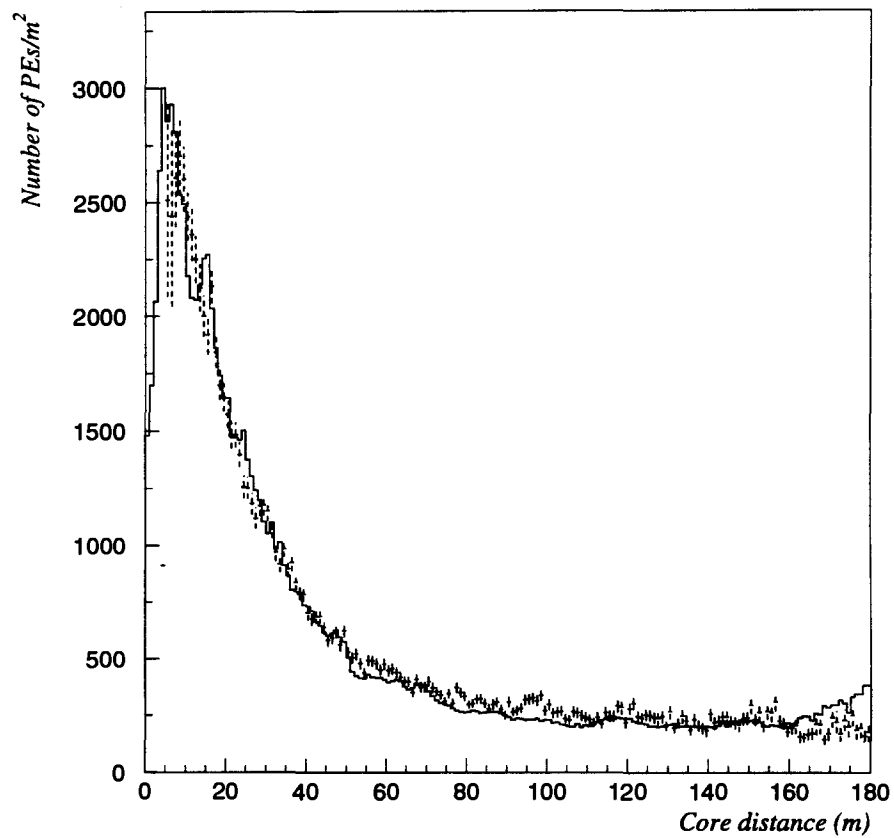


Figure 4.5: The PE lateral distributions from Monte Carlo simulations and the real data, after the performance of each PMT is lowered by about half. The points with error bars represent the Monte Carlo data and the histogram represents the real data.

Chapter 5

Techniques of Searching for Directional Excess

5.1 Optimal Bin Size

Signal events should come from a specific direction while cosmic-ray background events are isotropic. The significance ($Signal/\sqrt{Background}$) of a signal strength depends upon the size of the bin that includes the point source. The number of background events falling in the source bin is proportional to the given bin area while the signal events falling in the same source bin depend upon the intrinsic angular resolution, defined by the standard deviation (σ) of a 2-dimensional Gaussian distribution, of the experiment. Therefore, one must make an *a priori* choice of the optimal angular bin size to maximize the significance of a true signal based upon the predicted number of events falling in that bin. The signal is assumed to follow the 2-dimensional Gaussian distribution.

Biller [122] has done Monte Carlo studies to determine the optimal bin sizes for different statistical tests of event excess (Poisson distributed) and periodicity

Test	Radius of Optimal Bin (units of σ)
Poisson	$1.6 + 0.7e^{-0.88N^{0.36}}$
Rayleigh	$1.6 + 7.4e^{-2.29N^{0.14}}$
Protheroe	$1.6 + 3.9e^{-1.76N^{0.19}}$

Table 5.1: Optimal bin radii for various tests [122].

studies (usually the Rayleigh or Protheroe test). The results are reproduced in Table 5.1. In the table, N is the number of background events expected to fall within a circle with a radius of one unit of angular resolution which is defined by the standard deviation (σ) of the 2-dimensional Gaussian distribution. Note that all the values are asymptotically approaching 1.6σ at large N . The use of an equal-sided (in angular units) bin (as is sometimes more convenient) in celestial coordinates, equal in area to the optimal circular bin, only results in a slight reduction in the estimate of significance. When expressed as the number of standard deviations from the Gaussian distribution mean, it decreases the number of standard deviations of a signal detection by about 1.5% on average.

5.2 Background Estimation

A correct estimation of the background is important to determine the significance of a weak signal present in a large isotropic background. The background bin with the same area as the source bin (centered on the point source) should transverse the same region of the sky with the same exposure time as the source bin. The

local parameters θ , the zenith angle, ϕ , the azimuthal angle, and t , the time of detection, of each air-shower event are transformed to celestial coordinates (α, δ) , where α is the right ascension and δ is the declination. Events that fall within the source bin are counted as the on-source events. Various methods can be used to estimate the background (see, e.g., Alexandreas [129]).

The *background map method* is chosen for the data analysis presented in this dissertation. In this method, ten fake events are generated for each detected event by associating the hour angle of the detected event with the times of ten other events randomly chosen from a time buffer which typically accumulates about 2 hours of data. Hence the original θ and ϕ and the new randomly selected time assigned to the fake event give new celestial coordinates α and δ . The fake events that fall within the source bin are counted as the background (off-source) events. The advantage of this method is that it automatically takes into account the distributions of times and local coordinates of the real events.

5.3 Significance Assessment

When the numbers of source events and background events are obtained, the chance probability of an excess (or deficit) beyond expectation must then be assessed. The prescription of Li and Ma [130] is widely adopted in UHE astronomy. Based on their analysis, if all counts come from the background and the numbers of on-source events and off-source events are not too small, the maximum likelihood ratio is

$$\lambda = \left[\frac{\alpha}{1 + \alpha} \left(\frac{N_{\text{on}} + N_{\text{off}}}{N_{\text{on}}} \right) \right]^{N_{\text{on}}} \left[\frac{1}{1 + \alpha} \left(\frac{N_{\text{on}} + N_{\text{off}}}{N_{\text{off}}} \right) \right]^{N_{\text{off}}}, \quad (5.1)$$

where α is the ratio of the on-source time to the off-source time, N_{on} is the number of counts in the source bin, and N_{off} is the number of counts in the background bin. Then the quantity $-2 \ln \lambda$ will approximately follow a χ^2 distribution with one degree of freedom. Therefore, the significance, S , of the observed result is

$$\begin{aligned} S &= \sqrt{-2 \ln \lambda} \\ &= \sqrt{2} \left\{ N_{\text{on}} \ln \left[\frac{1 + \alpha}{\alpha} \left(\frac{N_{\text{on}}}{N_{\text{on}} + N_{\text{off}}} \right) \right] \right. \\ &\quad \left. + N_{\text{off}} \ln \left[(1 + \alpha) \left(\frac{N_{\text{off}}}{N_{\text{on}} + N_{\text{off}}} \right) \right] \right\}^{1/2}. \end{aligned} \quad (5.2)$$

One alternative method that is still valid in the limit of a small number of events calculates the probability of observing N_s on-source events or more, given each possible Poisson fluctuation in the total number of N_b background events [129]:

$$P(\geq N_s, N_b, \alpha) = \sum_{n_s=N_s}^{\infty} \int_{b=0}^{\infty} db \mathcal{P}(b, N_b) \mathcal{P}(b\alpha, n_s), \quad (5.3)$$

where α is the ratio of the number of source bins to that of background bins, and b is the true number of total background events. $\mathcal{P}(N_1, N_2)$ is the probability of observing N_2 events given a Poisson distribution with mean N_1 . Replacing the expressions with the Poisson probability and performing the integration yields

$$P(\geq N_s, N_b, \alpha) = \sum_{n_s=N_s}^{\infty} \frac{\alpha^{n_s}}{(1 + \alpha)^{N_b + n_s + 1}} \frac{(N_b + n_s)!}{N_b! n_s!} \quad (5.4)$$

$$= 1 - \sum_{n_s=0}^{N_s-1} \frac{\alpha^{n_s}}{(1 + \alpha)^{N_b + n_s + 1}} \frac{(N_b + n_s)!}{N_b! n_s!}. \quad (5.5)$$

5.4 Flux Upper Limit

If no statistically significant result is found, the observed number of on-source events and the expected number of background events can be used to derive an

upper limit for the number of signal events [131, 132]. The γ -ray flux upper limit for UHE emission is [133]

$$\phi_\gamma(> E) = \frac{f_{90} \phi_{\text{CR}}(> E) \Omega}{\epsilon R_\gamma}, \quad (5.6)$$

where

$$\phi_{\text{CR}}(> E) = (1.8 \pm 0.5) \times 10^{-5} (E/\text{TeV})^{-1.76 \pm 0.09} \text{ cm}^{-2} \text{ s}^{-1} \text{ sr}^{-1} \quad (5.7)$$

is the measured all-particle cosmic-ray flux above energy E in TeV [134, 135], Ω is the solid angle subtended by the source bin, ϵ is the fraction of the signal that is expected to be contained in the source bin ($\epsilon = 0.72$ for a bin of radius 1.6σ), and R_γ is the ratio of the detection efficiency for γ -rays to that for cosmic rays. The quantity f_{90} is defined as the number of excess source events relative to the number of cosmic-ray events in the source bin at the 90% confidence level (CL):

$$f_{90} = \frac{N_{\text{lim}}}{N_{\text{cr}}}, \quad (5.8)$$

where N_{lim} is the 90% CL upper limit on the excess number of events above the cosmic ray background and N_{cr} is the number of background events. The values of R_γ are determined from Monte Carlo simulations.

5.5 Timing Analyses

In pulsar analysis, the arrival times of γ -rays from the source direction are used to search for the periodicity. The arrival times measured at the earth's surface are affected by the motion of the earth, the motion of the source itself, and the gravitational potential at the earth. The motion of the earth introduces a variable

time delay to the observed times, which can be removed by correcting the times to an inertial reference frame. The motion of the source, including the proper motion and, if present, the orbital motion, also changes the measured source period. The proper motion of the source is usually small enough to be neglected. The gravitational potential at the earth differs from the potential at a large distance from the sun; furthermore, it varies annually due to the elliptical shape of the earth orbit. General Relativity predicts a small effect on the earth-bound clock rate. The annual variation of an atomic clock on the surface of the earth as it follows its elliptical orbit around the sun can be corrected to an identical clock at an infinite distance from the sun. A full discussion of this relativistic effect in pulsar timing is presented by Backer and Hellings [136].

5.5.1 Solar-System Barycentering Correction

The series of pulse arrival times observed on earth need to be corrected to an inertial frame with respect to the pulsar. In practice, the expected arrival times are computed using the source position and an ephemeris giving the vector distance \mathbf{r}_{ob} from the observer to the solar system barycenter (SSB). This vector distance can be expressed as the sum of three vectors \mathbf{r}_{oc} , from the observer to the center of the earth, \mathbf{r}_{cs} , from the center of the earth to the center of the sun, and \mathbf{r}_{sb} , from the center of the sun to the SSB:

$$\mathbf{r}_{\text{ob}} = \mathbf{r}_{\text{oc}} + \mathbf{r}_{\text{cs}} + \mathbf{r}_{\text{sb}}. \quad (5.9)$$

The determination of the vector \mathbf{r}_{cs} may require the combination of two ephemerides that give respectively the motion of the barycenter of the earth-moon system and the motion of the earth within that system. The time t_c to be added to the observed

arrival time to give a barycentric time is then

$$t_c = -\frac{1}{c} \mathbf{r}_{\text{ob}} \cdot \hat{\mathbf{s}}, \quad (5.10)$$

where $\hat{\mathbf{s}}$ is the position unit vector from the observer to the source. The two ephemerides commonly implemented are the MIT (PEP311) ephemeris [137] and the JPL (DE200) ephemeris [138]. However, the MIT ephemeris only covers the dates up to February 1990.

5.5.2 Pulse Arrival-Time Correction for Binaries

The orbital motion of the pulsar in a binary system gives rise to a sinusoidal effect on the intrinsic pulse period. After the event times have been corrected to the SSB and the relativistic effect has been removed, the orbital time correction can be obtained with the orbital parameters. The time affected by the eccentric orbit can be represented by a form [139]

$$\Delta t_{\text{orb}} = \frac{a \sin i}{c} (1 - e^2) \frac{\sin(v + \omega)}{1 + e \cos v}, \quad (5.11)$$

where $a \sin i$ is the projected semimajor axis of the pulsar orbiting with an inclination angle i in the binary system, e is the eccentricity, v is the true anomaly, and ω is the longitude of periastron. The true anomaly, v , can be calculated from the observed mean anomaly, θ [$\theta = 2\pi(t - \tau)/P_{\text{orb}}$; τ = the time of periastron passage, P_{orb} = the orbital period], using the relations

$$\tan \frac{v}{2} = \left(\frac{1 + e}{1 - e} \right)^{1/2} \tan \frac{E}{2} \quad (5.12)$$

and

$$E - e \sin E = \theta. \quad (5.13)$$

If the orbit is nearly circular, then Eq. 5.11 can be simplified to

$$\Delta t_{orb} = \frac{a \sin i}{c} \sin(v + \omega). \quad (5.14)$$

The amount of Δt_{orb} should be subtracted from the SSB-corrected pulse arrival times to obtain the times of emission.

5.6 Epoch Folding

5.6.1 Phase Calculation

A convenient way to search for the periodicity of a potential source is to fold the arrival times into phases. The expected phase, ϕ , starting at an arbitrary time t_0 with initial phase ϕ_0 , is calculated using the provided period, P , and its derivatives, \dot{P} and \ddot{P} , or, more conveniently, using the frequency, ν , and its derivatives, $\dot{\nu}$ and $\ddot{\nu}$:

$$\phi = \text{MOD}(\phi_0 + \nu(t - t_0) + \frac{1}{2}\dot{\nu}(t - t_0)^2 + \frac{1}{6}\ddot{\nu}(t - t_0)^3, 1), \quad (5.15)$$

where t is the corrected arrival time.

5.6.2 Rayleigh Test

The Rayleigh test is useful for searching for a single-peak light curve. The power, R_p , is defined as [140]

$$R_p = N\overline{R}^2 = N(\overline{C}^2 + \overline{S}^2), \quad (5.16)$$

where

$$\overline{C} = \frac{1}{N} \sum_{i=1}^N \cos(2\pi\phi_i),$$

$$\begin{aligned}\bar{S} &= \frac{1}{N} \sum_{i=1}^N \sin(2\pi\phi_i), \\ N &= \text{number of events,} \\ \phi_i &= \text{phase of the } i\text{th event.}\end{aligned}$$

The distribution of $2N\bar{R}^2$ is a χ^2 distribution with 2 degrees of freedom [141]. The probability level for $N \gtrsim 100$ is, assuming a flat light curve for the null hypothesis,

$$P(> R_p) = e^{-R_p}. \quad (5.17)$$

For values of $N \gtrsim 20$, the probability can be approximated as [122]

$$\begin{aligned}P(> R_p) &= e^{-R_p} \left[1 + \frac{1}{2N} \left(R_p - \frac{R_p^2}{2!} \right) + \frac{1}{12N^2} \left(-R_p + \frac{11R_p^2}{2!} - \frac{19R_p^3}{3!} + \frac{9R_p^4}{4!} \right) + \right. \\ &\quad \left. \frac{1}{24N^3} \left(-2R_p - \frac{4R_p^2}{2!} + \frac{69R_p^3}{3!} - \frac{163R_p^4}{4!} + \frac{145R_p^5}{5!} - \frac{45R_p^6}{6!} \right) \right]. \quad (5.18)\end{aligned}$$

For smaller values of N , the Monte Carlo method can be used to assess the significance level for phase alignment. Table D.2 of Biller [122] gives the chance probability levels for some critical values of the Rayleigh power. The Rayleigh test is sensitive to broad peaks and sinusoids [141].

5.6.3 Z_n^2 Test

The Z_n^2 test is the extension of the Rayleigh test obtained by summing the powers in the first n harmonics of the period tested. It can be used to investigate the uniformity of the folded data for multiple peaks. The Z_n^2 statistic is given by the power

$$Z_n^2 = \frac{2}{N} \sum_{k=1}^n \left\{ \left(\sum_{i=1}^N \cos 2k\pi\phi_i \right)^2 + \left(\sum_{i=1}^N \sin 2k\pi\phi_i \right)^2 \right\}, \quad (5.19)$$

where the sums are performed over the first n harmonics and over the total number of events, N . For uniformly distributed data and a large number of events

($N \gtrsim 100$), Z_n^2 asymptotically approaches the χ^2 distribution with $2n$ degrees of freedom (χ_{2n}^2). For $N \lesssim 20$, the probability may be assessed, again, using the Monte Carlo method. For N between ~ 20 and ~ 100 , the distribution of Z_n^2 can be determined as follows [141]: Let the Rayleigh power of the l th harmonic be

$$N\overline{R}_l^2 = N(\overline{C}_l^2 + \overline{S}_l^2) = K_l, \quad (5.20)$$

where

$$\begin{aligned} \overline{C}_l &= \frac{1}{N} \sum_{i=1}^N \cos(2l\pi\phi_i), \\ \overline{S}_l &= \frac{1}{N} \sum_{i=1}^N \sin(2l\pi\phi_i). \end{aligned}$$

Then the chance probability level for each harmonic l can be calculated from Eq. 5.18 and, under the null hypothesis, the statistic $-2 \ln (\prod_{l=1}^n P_l(> K_l))$ follows χ_{2n}^2 [141, 142].

5.7 Combination of Probabilities

In some cases one needs to combine two or more probabilities to obtain the overall probability. For the combination of two independent probabilities P_1 and P_2 , the combined probability can be expressed as [142]

$$P_{\text{comb}} = P_1 P_2 (1 - \ln(P_1 P_2)), \quad (5.21)$$

where the combined probability, P_{comb} , is derived by integrating the shaded area below the curve shown in Fig. 5.1. For combining m (> 2) independent probabilities in this manner, the overall probability is obtained from the quantity $-2 \ln (\prod_{i=1}^m P_i)$ which is distributed as χ_{2m}^2 under the null hypothesis [141, 142].

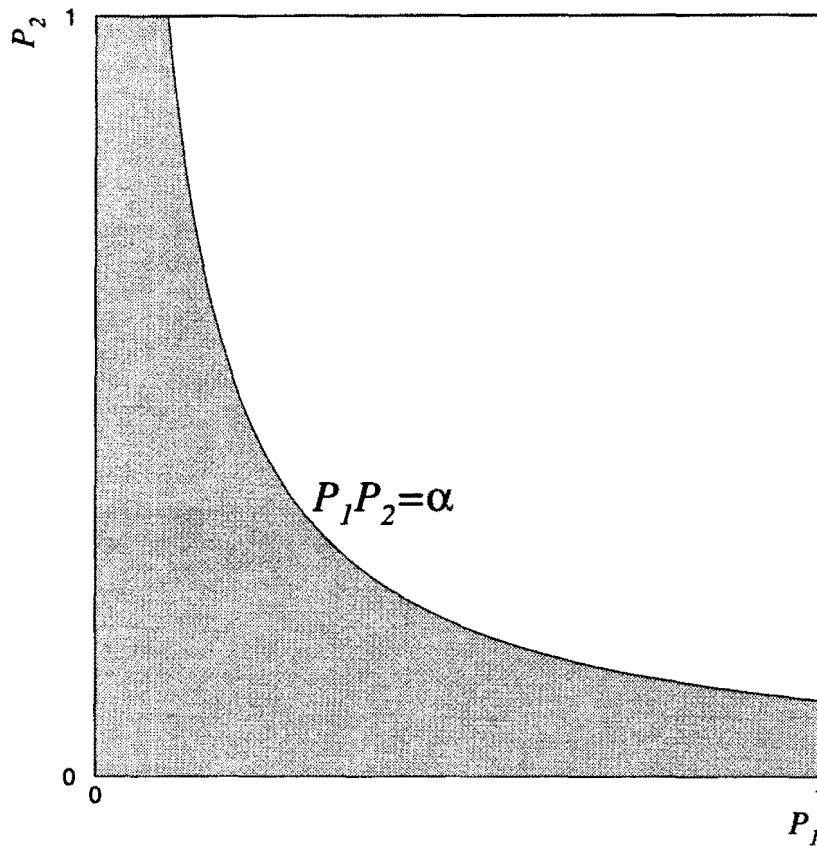


Figure 5.1: Range of probabilities bounded by the product of two probabilities P_1 and P_2 .

Chapter 6

Searches and Results

6.1 Data Selection

The analysis is performed with two datasets, namely the CYGNUS-I dataset and the JASA dataset. The JASA dataset is in a sense a subset of the CYGNUS-I dataset, with the difference being that the shower arrival directions are obtained from the pools using the method described in Sec. 4.7. Both datasets are individually analyzed for long-term (over the whole datasets) unpulsed and pulsed emissions and for episodic emissions on the time scale of one source day. A source day consists of 24 sidereal hours, centered at the source meridian transit. Each dataset is divided into categories of (1) all events and (2) muon-poor (no observed E225 muons) events.

The CYGNUS-I dataset covers the period from 1986 April 2 (JD 2446522.5; Run 62) through 1994 March 7 (JD 2449418.5; Run 6999). It contains a total of about 4.3×10^8 air showers, of which $\sim 2.4 \times 10^8$ air showers have no observed E225 muons. The JASA dataset covers the period from 1992 October 23 (JD 2448918.5; Run 5160) to 1993 October 23 (JD 2449283.5; Run 6491). Runs 5500–5599 (1993

January 27–1993 February 22; JD 2449014.5–JD 2449040.5) in the dataset are not used because during those days the JASA pools were used for other tests. Only showers where 15 or more JASA PMT signals were used in the reconstruction of the arrival direction are retained for the searches. This gives the JASA array an improved angular resolution of 0.32° [126]. About 3.6×10^7 air showers, or $\sim 68\%$ of the number of CYGNUS events, survive this cut. The muon-poor (with zero observed E225 muons) data contain $\sim 1.7 \times 10^7$ air showers.

For the analysis of the pulsed emission (the “periodicity” search), runs before 2894 (1991 February 27; JD 2448314.5) are excluded because the event times are stored on the computer disks with the precision down to the millisecond level. For the purpose of searching for the fast pulsars, a precision down to a few hundreds of microseconds or less is necessary. During Runs 2894–4625 the event times in the data files stored on the computer disks differ from the correct event times by up to several milliseconds due to a software precision error. This portion of data has been corrected prior to the data analysis presented here.

6.2 Analysis

The bin sizes chosen in this analysis are determined from the angular resolutions and the expected number of background events (see Table 5.1) of the CYGNUS-I and the JASA arrays. For the CYGNUS-I dataset, a source bin size of 2° in DEC (δ) by $2^\circ/\cos \delta$ in RA (α), centered on the source is used in all searches. A 1° (in δ) \times $1^\circ/\cos \delta$ (in α) bin is used for the JASA dataset because of its better angular resolution. The corresponding solid angles subtended in the source bin are $\Omega = 1.2 \times 10^{-3}$ sr for CYGNUS-I and $\Omega = 3.0 \times 10^{-4}$ sr for JASA. The fraction

of signal, ϵ , expected to be contained in the source bin is 0.72 for both of the bin sizes chosen.

The trigger condition for both datasets is only determined by the CYGNUS-I array. The ratio of the detection efficiency for gamma rays to that for cosmic rays, R_γ , as determined from Monte Carlo simulations, for a given source in this analysis is found to be the same for both datasets. It is a function of declination [135] and also depends on the assumed source spectrum. The R_γ -values for the CYGNUS-I all-event (muon-poor) data for the Crab, PSR 1937+21, PSR 1951+32, PSR 1953+29 and PSR 1957+20 are 2.3 (4.1), 2.3 (4.1), 2.4 (4.3), 2.4 (4.3), and 2.3 (4.1), respectively [135], and the R_γ -values for the JASA all-event (muon-poor) data for the Crab, PSR 1937+21, PSR 1951+32, PSR 1953+29 and PSR 1957+20 are 2.3 (4.9), 2.3 (4.9), 2.4 (5.1), 2.4 (5.1), and 2.3 (4.9), respectively, when the integral spectral index of the source is assumed to be the same as that of the cosmic rays.

6.3 Search for Unpulsed Emission

Long-Term Results

Tables 6.1–6.2 give the search results of the long-term unpulsed emission. The significance (σ) is calculated using the Li and Ma formula (Eq. 5.1). The significance from both categories in both datasets ranges from -2.1σ to 2.3σ . The most significant event excess is the 2.3σ excess of PSR 1957+20 in its JASA all-event data, which corresponds to a pre-trials probability of 1% of being an accidental detection. It needs to account for the trials factors of selecting the most significant

result from the five pulsars and from the two categories in each of the two datasets. The trials factor for selecting from the five sources is 5. Since the all-event data and muon-poor event data are not totally independent, as is the same for the CYGNUS-I data and the JASA data, Monte Carlo simulations can be used to assess the trials factors. Two sets of a large number of background events are simulated. For example, one represents the CYGNUS-I data and the other represents the JASA data. Then one can ask exactly the same questions as was done in the original analysis and apply the same analysis on the simulated data. If the most significant pre-trials probability, P_{pre} , is picked from any of the two datasets, then a trials factor should be applied such that the post-trials probability

$$P_{\text{post}} = 1 - (1 - P_{\text{pre}})^{T_{\text{trials}}} \quad (6.1)$$

is uniformly distributed between 0 and 1. The trials factor for selecting the most significant event excess from the all-event and muon-poor data is found to be 1.3, while the trials factor for selecting from the CYGNUS-I and the JASA data is 1.9. Therefore, the final post-trials probability for the JASA all-event data of PSR1957+20 is

$$P = 1 - (1 - 0.01)^{5 \times 1.3 \times 1.9} = 1 - (1 - 0.01)^{12.35} = 11.7\%, \quad (6.2)$$

which is consistent with chance. The 90% CL flux upper limits (see Sec. 5.4) are also shown in Tables 6.1–6.2. For simplicity, all the upper limits are quoted at energies greater than the CYGNUS-I median energy $E_m = 100$ TeV, assuming the γ -ray spectral index is the same as the cosmic-ray spectral index.

The previous flux upper limits over 5 years for the Crab quoted above 40 TeV at 90% CL by Dion [66] are $2.9 \times 10^{-13} \text{ cm}^{-2} \text{ s}^{-1}$ for all-event data and 6.6×10^{-13}

(a) All events

Source	N_s	N_b	σ	f_{90}	ϕ_γ
Crab	92382	92153.8	0.7	0.0076	3.0
PSR 1937+21	93121	92978.6	0.4	0.0067	2.6
PSR 1951+32	120279	120671.5	-1.1	0.0035	1.3
PSR 1953+29	117686	118009.9	-0.9	0.0036	1.4
PSR 1957+20	90907	90632.0	0.9	0.0080	3.2

(b) μ -poor events

Source	N_s	N_b	σ	f_{90}	ϕ_γ
Crab	50627	50443.0	0.8	0.010	2.2
PSR 1937+21	50717	50788.7	-0.3	0.0069	1.5
PSR 1951+32	73256	73363.3	-0.4	0.0057	1.2
PSR 1953+29	68658	68963.1	-1.1	0.0046	0.9
PSR 1957+20	49487	49265.7	0.9	0.011	2.4

Table 6.1: The results of searching for long-term unpulsed emission in the CYGNUS-I data. (a) For all-event data. (b) For μ -poor-event data. The data shown are N_s , the number of events in the source bin, N_b , the expected background events, σ , the Li and Ma significance, f_{90} , the 90% confidence level upper limit for the number of excess source events relative to the number of detected cosmic-ray events in the source bin, and ϕ_γ , the 90% confidence level upper limit for the γ -ray flux above 100 TeV. The unit for the flux is $(\text{photons cm}^{-2} \text{ s}^{-1}) \times 10^{-14}$.

(a) All events

Source	N_s	N_b	σ	f_{90}	ϕ_γ
Crab	2217	2198.1	0.4	0.044	4.3
PSR 1937+21	2198	2197.8	0.0	0.038	3.7
PSR 1951+32	2492	2604.4	-2.1	0.018	1.7
PSR 1953+29	2583	2575.7	0.1	0.036	3.4
PSR 1957+20	2239	2125.7	2.3	0.085	8.4

(b) μ -poor events

Source	N_s	N_b	σ	f_{90}	ϕ_γ
Crab	915	893.8	0.7	0.077	3.6
PSR 1937+21	924	902.3	0.7	0.077	3.6
PSR 1951+32	1206	1250.8	-1.2	0.034	1.5
PSR 1953+29	1214	1154.8	1.6	0.094	4.2
PSR 1957+20	896	866.0	1.0	0.087	4.1

Table 6.2: The results of searching for long-term unpulsed emission in the JASA data. (a) For all-event data. (b) For μ -poor-event data. The data shown are N_s , the number of events in the source bin, N_b , the expected background events, σ , the Li and Ma significance, f_{90} , the 90% confidence level upper limit for the number of excess source events relative to the number of detected cosmic-ray events in the source bin, and ϕ_γ , the 90% confidence level upper limit for the γ -ray flux above 100 TeV. The unit for the flux is $(\text{photons cm}^{-2} \text{ s}^{-1}) \times 10^{-14}$.

$\text{cm}^{-2} \text{ s}^{-1}$ for muon-poor data. These, respectively, correspond to $6.1 \times 10^{-14} \text{ cm}^{-2} \text{ s}^{-1}$ and $1.4 \times 10^{-13} \text{ cm}^{-2} \text{ s}^{-1}$ above 100 TeV. These flux upper limits are about 2–3 times higher than the limits quoted in this work. The steady flux upper limits presented here for the Crab are compared with other experiments in Fig. 6.1. The crosses are the data points and the dashes with down arrows are the upper limits. The flux upper limits computed from the JASA results should be better than those computed from the CYGNUS-I results with the same observation time, because the JASA array has better angular resolution and, therefore, a smaller source bin size (see Eq. 5.6). However, the CYGNUS-I results have better flux upper limits than the JASA results due to the much longer observation window. Therefore, the lower upper limits from the CYGNUS-I results are quoted in the figure. The straight lines are the linear extrapolations of the measured energy spectrum for the Crab from the Whipple collaboration (for the old and new derivations) and the THEMISTOCLE collaboration. All the flux upper limits presented here are below the old and above the new Whipple spectrum.

Daily Results

The distributions of Li and Ma sigmas (σ 's) and the number of estimated background events are plotted for each source day in Figs. 6.2–6.21 for each source searched. The number of expected background events for JASA varies because when a PMT dies in a pool, all the PMTs in that pool must be turned off to open the cover to remove the PMT from the pool. The same thing happens when a repaired PMT is placed back in the pool. After the pool is opened and re-covered, the PMTs in that pool need to be left off for a while to “cool off” in order to

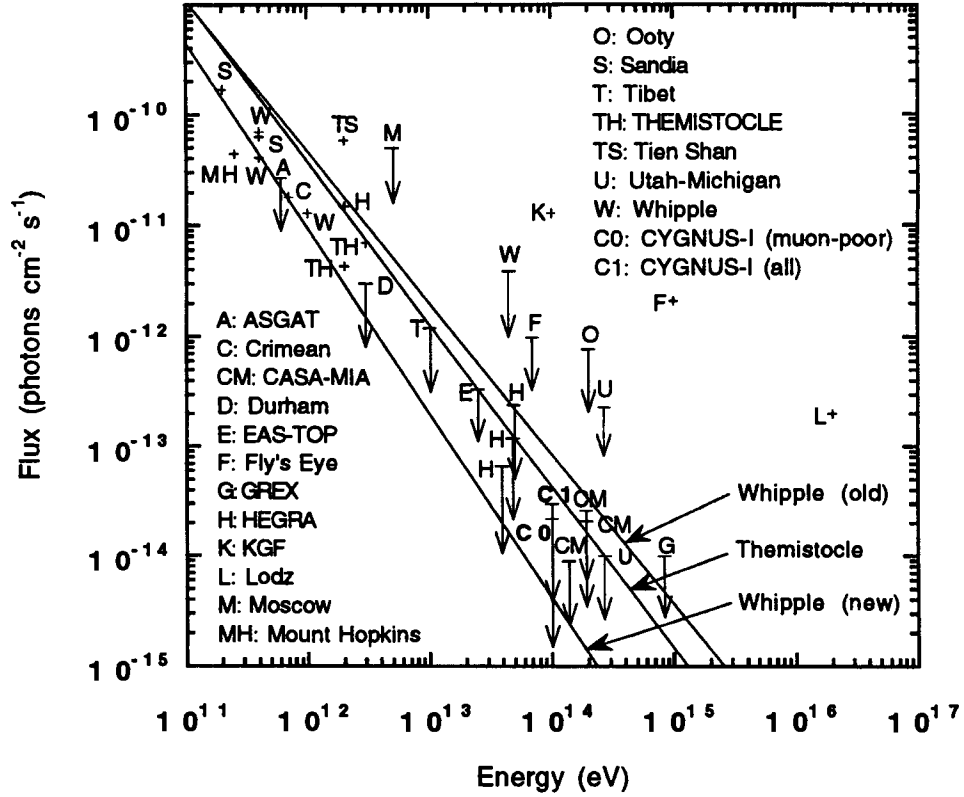


Figure 6.1: Measured steady fluxes and upper limits for the Crab from various experiments. The crosses are the observed fluxes and the dashes with down arrows are the upper limits. The 90% upper limits obtained from this work are denoted C0, C1. Also see Table 2.1 for reference.

reduce the noise. Sometimes a pool is off for several days due to hardware problems. One should also remember that JASA runs 5500–5599 are not used in the analysis, which corresponds to about 27 days of data, and the counts are averaged over 30-day intervals. For the estimation of the significance, the Li and Ma sigmas are fitted quite well by a Gaussian distribution for large N_b . The Li and Ma prescription is not a good representation of the statistical significance for deficits for small N_b , but it is still a good representation for positive excesses [129].

In this search there are about $N_d = 2500$ (300) source days in the CYGNUS-I (JASA) dataset. The chance probability for the *hottest* day with the lowest probability P_{\min} to be seen from any of the N_d days for a particular source is

$$P_{\text{ex}} = 1 - (1 - P_{\min})^{N_d}, \quad (6.3)$$

where P_{\min} is the pre-trials probability and P_{ex} is the post-trials probability for that source. For a very small P_{\min} , the post-trials probability can be approximated as $P_{\text{ex}} \approx N_d P_{\min}$. The most significant day for each source, its pre-trials probability, the number of source days and post-trials probability for that source are shown in Tables 6.3–6.4. The time for the most significant source day is given at the time of the source meridian transit over the telescope. A source day is one sidereal day long. The most significant result comes from the JASA muon-poor data of PSR 1937+21. It shows a post-trials chance probability of 8.9%. When the trials factor of 5 (for the choice from 5 sources) \times 1.3 (for the choice from the all-event data and the muon-poor data) \times 1.9 (for the choice from the CYGNUS-I data and the JASA data) = 12.35 is considered, this probability increases to 68.4%, which is consistent with the null hypothesis.

(a) All events

Source	T_{JD}	T_{sec}	P_{\min}	N_d	P_{ex}
Crab	7644	79762.8	7.2×10^{-5}	2493	0.16
PSR 1937+21	7676	36670.9	2.3×10^{-4}	2498	0.44
PSR 1951+32	7121	82250.7	4.8×10^{-4}	2510	0.70
PSR 1953+29	7015	21236.7	1.6×10^{-4}	2508	0.33
PSR 1957+20	8955	80795.1	2.3×10^{-4}	2496	0.44

(b) μ -poor events

Source	T_{JD}	T_{sec}	P_{\min}	N_d	P_{ex}
Crab	8481	54634.3	1.6×10^{-4}	2344	0.31
PSR 1937+21	7963	55128.9	6.9×10^{-4}	2375	0.81
PSR 1951+32	7092	2928.0	9.6×10^{-5}	2426	0.21
PSR 1953+29	7134	79327.5	4.8×10^{-4}	2417	0.69
PSR 1957+20	8347	51900.2	4.8×10^{-4}	2366	0.68

Table 6.3: Results of searching for episodic emission over a time scale of one source day using the CYGNUS-I dataset. (a) For all-event data. (b) For μ -poor-event data. Quantities shown are T_{JD} , the Julian Day – 2440000.5 of the most significant source day at the time of source meridian transit, T_{sec} , the UTC seconds of the most significant source day at the time of source meridian transit, P_{\min} , the pre-trials probability of the most significant day, N_d , the number of source days, and P_{ex} , the post-trials probability for that source.

(a) All events

Source	T_{JD}	T_{sec}	P_{\min}	N_d	P_{ex}
Crab	9013	15294.2	1.4×10^{-3}	304	0.35
PSR 1937+21	9234	13779.5	4.8×10^{-4}	296	0.13
PSR 1951+32	9227	16244.7	9.7×10^{-4}	299	0.25
PSR 1953+29	8984	73714.4	6.6×10^{-3}	300	0.86
PSR 1957+20	9189	25592.2	3.0×10^{-3}	294	0.59

(b) μ -poor events

Source	T_{JD}	T_{sec}	P_{\min}	N_d	P_{ex}
Crab	9228	50737.7	1.1×10^{-2}	279	0.95
PSR 1937+21	9045	58336.5	3.4×10^{-4}	273	0.089
PSR 1951+32	9227	16244.7	3.7×10^{-3}	293	0.66
PSR 1953+29	9127	39979.3	3.4×10^{-3}	293	0.63
PSR 1957+20	9133	38803.2	9.7×10^{-4}	277	0.24

Table 6.4: Results of searching for episodic emission over a time scale of one source day using the JASA dataset. (a) For all-event data. (b) For μ -poor-event data. Quantities shown are T_{JD} , the Julian Day – 2440000.5 of the most significant source day at the time of source meridian transit, T_{sec} , the UTC seconds of the most significant source day at the time of source meridian transit, P_{\min} , the pre-trials probability of the most significant day, N_d , the number of source days, and P_{ex} , the post-trials probability for that source.

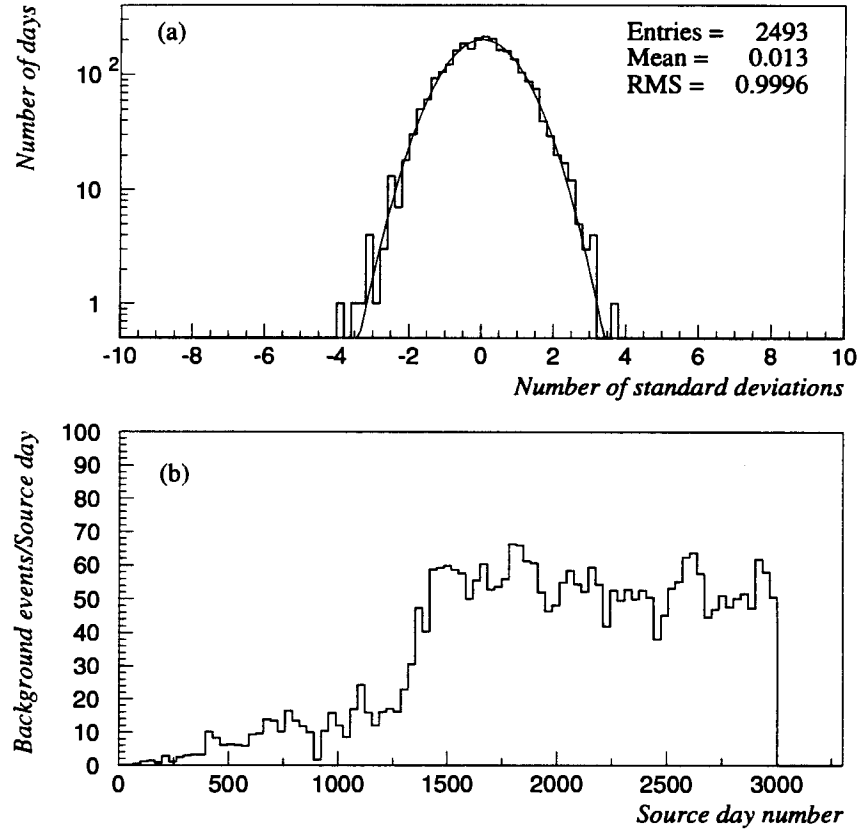


Figure 6.2: (a) Distribution of daily sigmas from the Crab using all events in CYGNUS-I dataset. The solid line is a best fit to a Gaussian distribution. (b) Number of calculated background events. The rise in the number of background events per source day represents the changes in experimental configurations, as described in Sec. 3.2. The counts have been averaged over 30-day intervals.

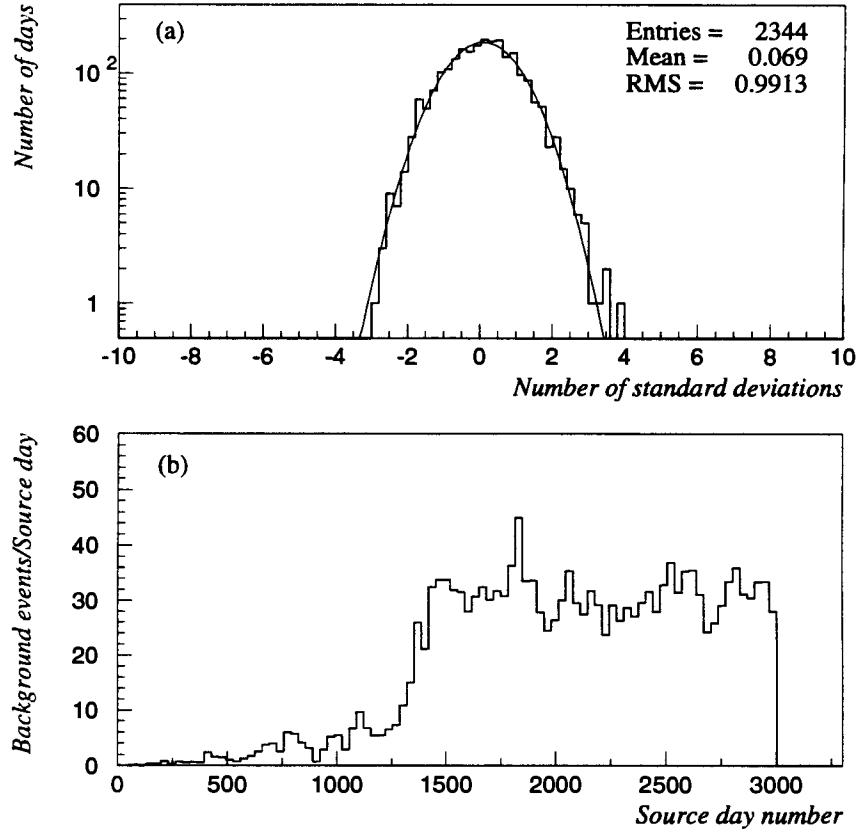


Figure 6.3: (a) Distribution of daily sigmas from the Crab using μ -poor events in the CYGNUS-I dataset. The solid line is a best fit to a Gaussian distribution. (b) Number of calculated background events. The rise in the number of background events per source day represents the changes in experimental configurations, as described in Sec. 3.2. The counts have been averaged over 30-day intervals.

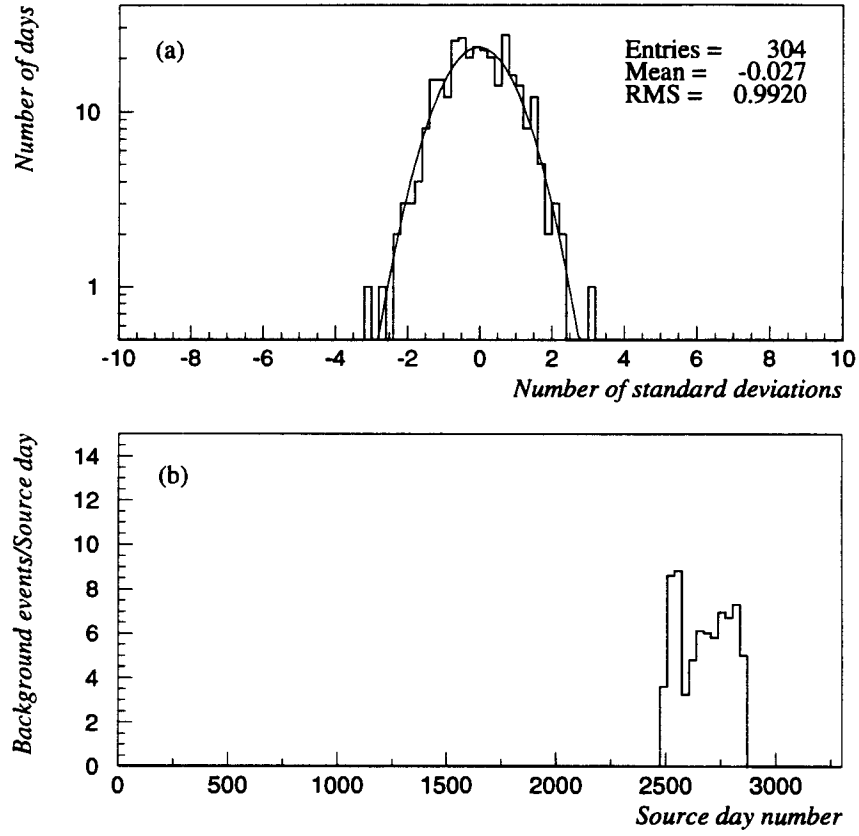


Figure 6.4: (a) Distribution of daily sigmas from the Crab using all events in JASA dataset. The solid line is a best fit to a Gaussian distribution. (b) Number of calculated background events. The counts have been averaged over 30-day intervals.

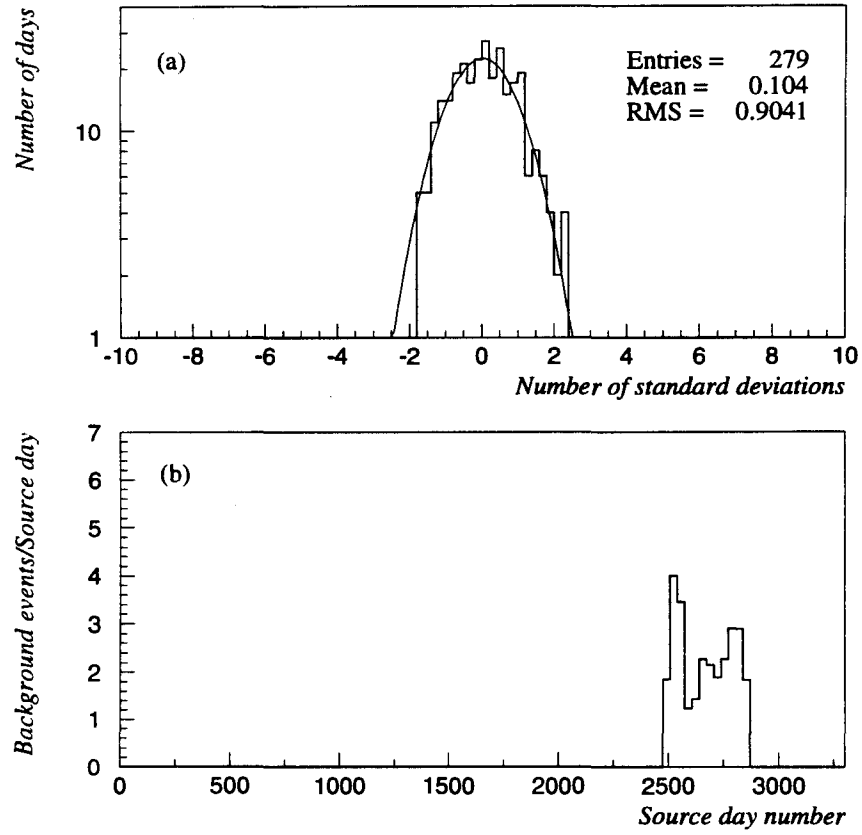


Figure 6.5: (a) Distribution of daily sigmas from the Crab using μ -poor events in JASA dataset. The solid line is a best fit to a Gaussian distribution. (b) Number of calculated background events. The counts have been averaged over 30-day intervals.

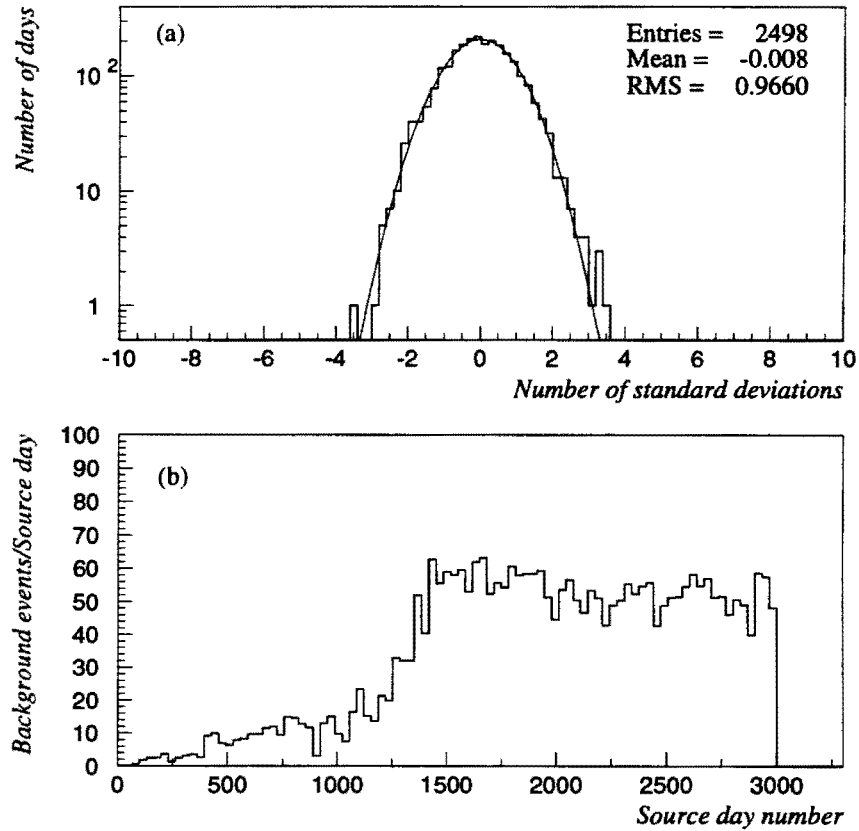


Figure 6.6: (a) Distribution of daily sigmas from PSR 1937+21 using all events in the CYGNUS-I dataset. The solid line is a best fit to a Gaussian distribution. (b) Number of calculated background events. The rise in the number of background events per source day represents the changes in experimental configurations, as described in Sec. 3.2. The counts have been averaged over 30-day intervals.

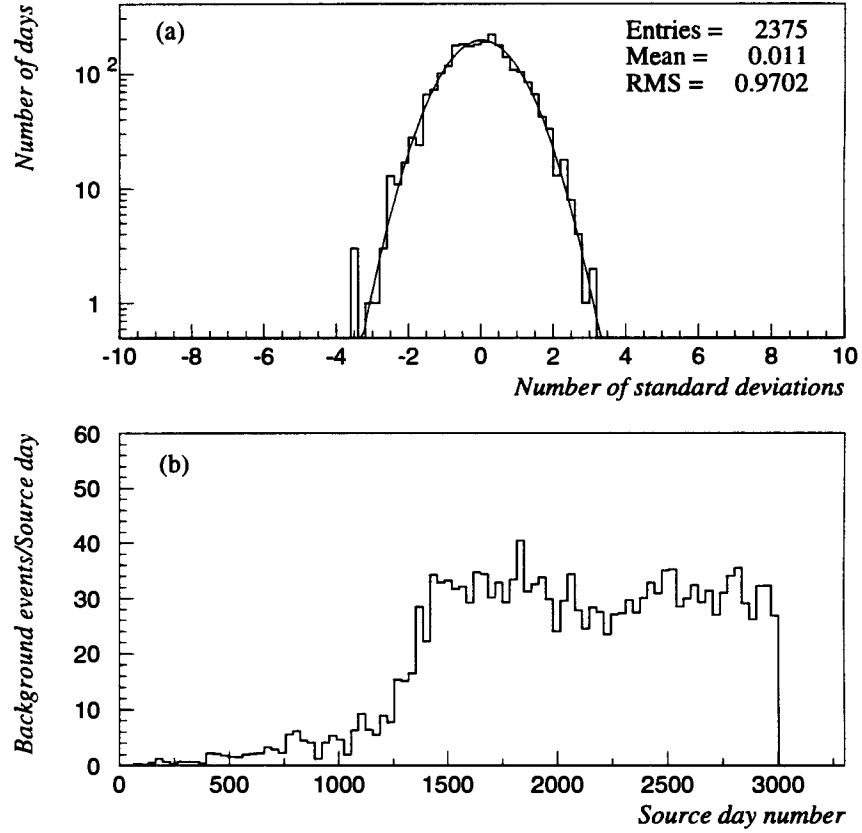


Figure 6.7: (a) Distribution of daily sigmas from PSR 1937+21 using μ -poor events in the CYGNUS-I dataset. The solid line is a best fit to a Gaussian distribution. (b) Number of calculated background events. The rise in the number of background events per source day represents the changes in experimental configurations, as described in Sec. 3.2. The counts have been averaged over 30-day intervals.

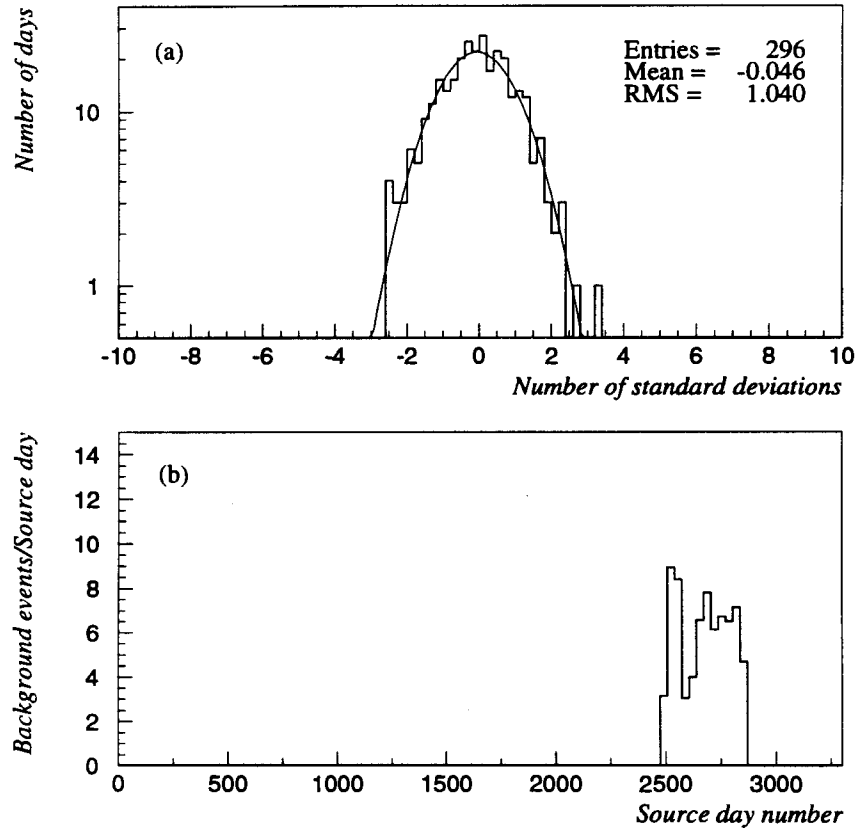


Figure 6.8: (a) Distribution of daily sigmas from PSR 1937+21 using all events in JASA dataset. The solid line is a best fit to a Gaussian distribution. (b) Number of calculated background events. The counts have been averaged over 30-day intervals.

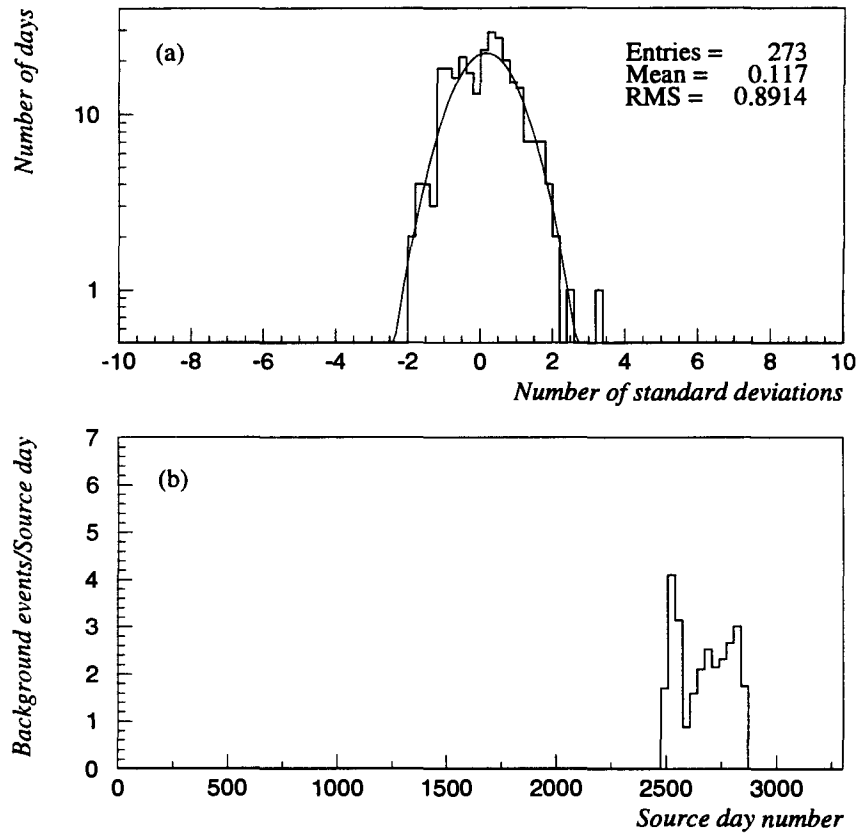


Figure 6.9: (a) Distribution of daily sigmas from PSR 1937+21 using μ -poor events in the JASA dataset. The solid line is a best fit to a Gaussian distribution. (b) Number of calculated background events. The counts have been averaged over 30-day intervals.

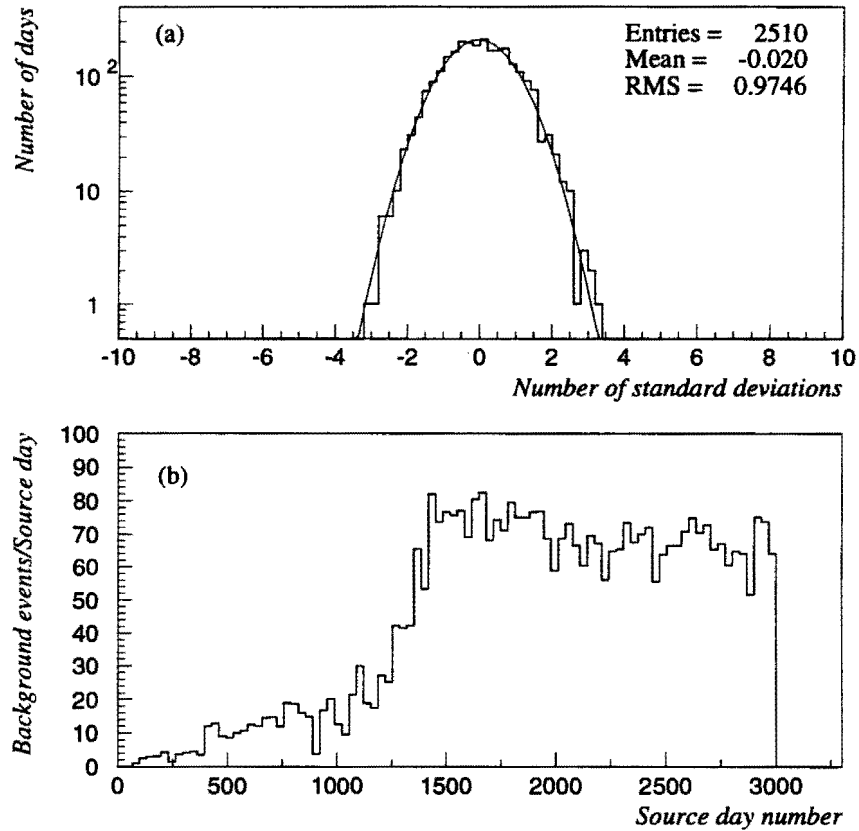


Figure 6.10: (a) Distribution of daily sigmas from PSR 1951+32 using all events in the CYGNUS-I dataset. The solid line is a best fit to a Gaussian distribution. (b) Number of calculated background events. The rise in the number of background events per source day represents the changes in experimental configurations, as described in Sec. 3.2. The counts have been averaged over 30-day intervals.

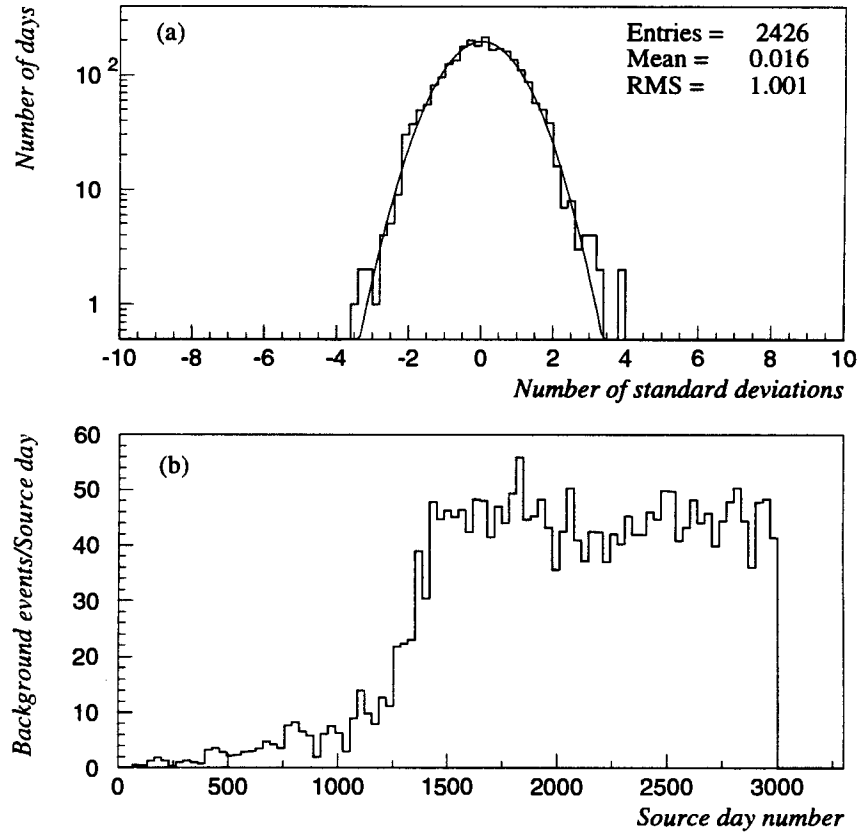


Figure 6.11: (a) Distribution of daily sigmas from PSR 1951+32 using μ -poor events in the CYGNUS-I dataset. The solid line is a best fit to a Gaussian distribution. (b) Number of calculated background events. The rise in the number of background events per source day represents the changes in experimental configurations, as described in Sec. 3.2. The counts have been averaged over 30-day intervals.

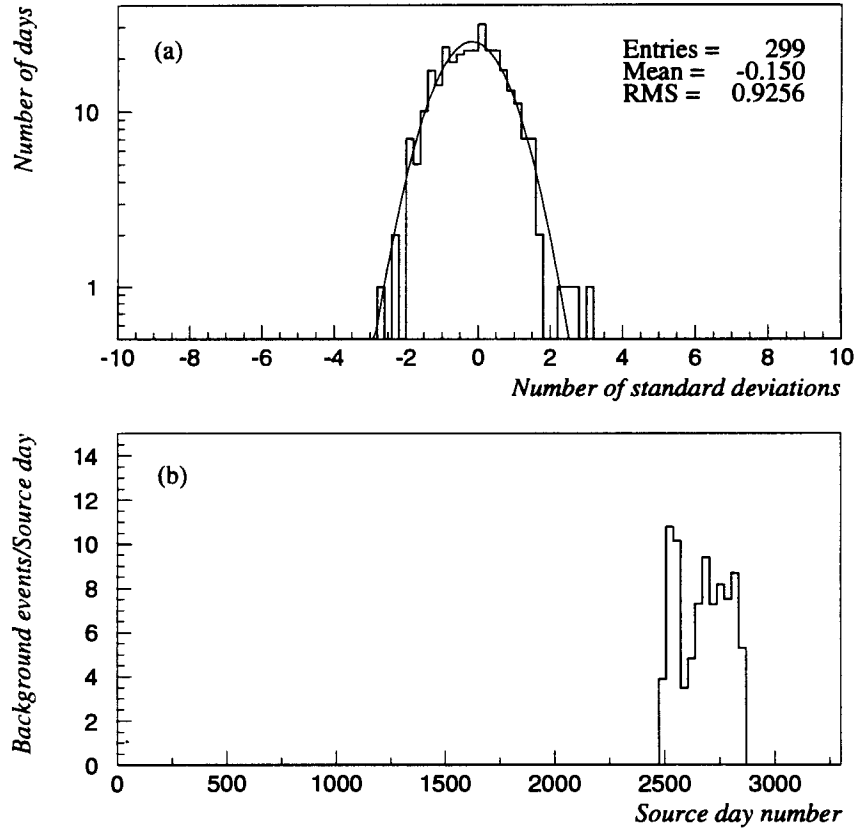


Figure 6.12: (a) Distribution of daily sigmas from PSR 1951+32 using all events in JASA dataset. The solid line is a best fit to a Gaussian distribution. (b) Number of calculated background events. The counts have been averaged over 30-day intervals.

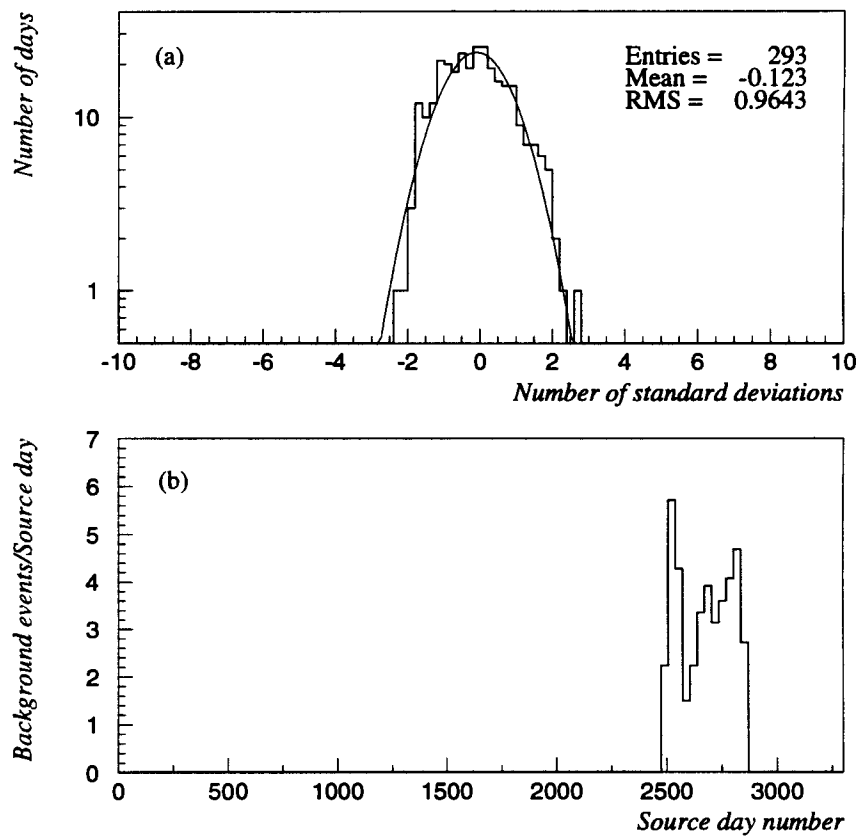


Figure 6.13: (a) Distribution of daily sigmas from PSR 1951+32 using μ -poor events in the JASA dataset. The solid line is a best fit to a Gaussian distribution. (b) Number of calculated background events. The counts have been averaged over 30-day intervals.

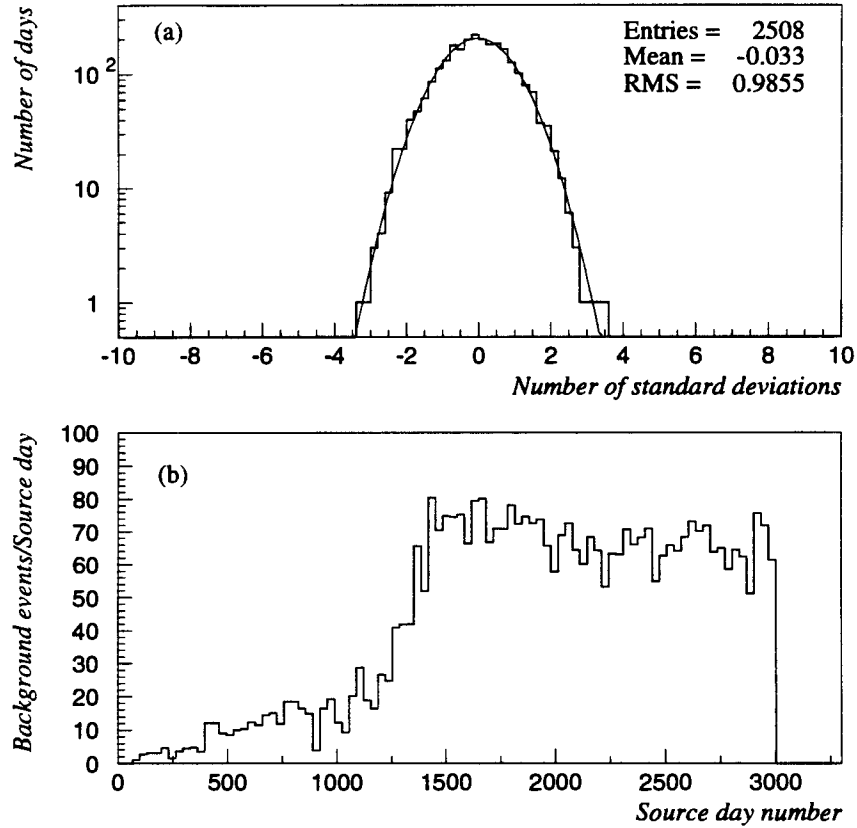


Figure 6.14: (a) Distribution of daily sigmas from PSR 1953+29 using all events in the CYGNUS-I dataset. The solid line is a best fit to a Gaussian distribution. (b) Number of calculated background events. The rise in the number of background events per source day represents the changes in experimental configurations, as described in Sec. 3.2. The counts have been averaged over 30-day intervals.

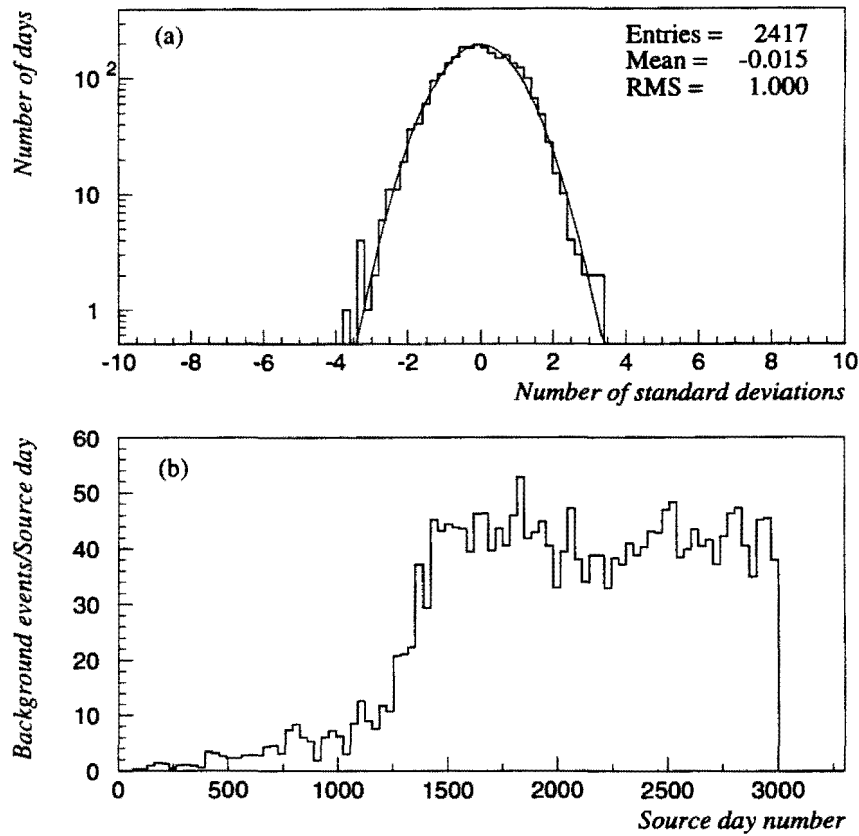


Figure 6.15: (a) Distribution of daily sigmas from PSR 1953+29 using μ -poor events in the CYGNUS-I dataset. The solid line is a best fit to a Gaussian distribution. (b) Number of calculated background events. The counts have been averaged over 30-day intervals.

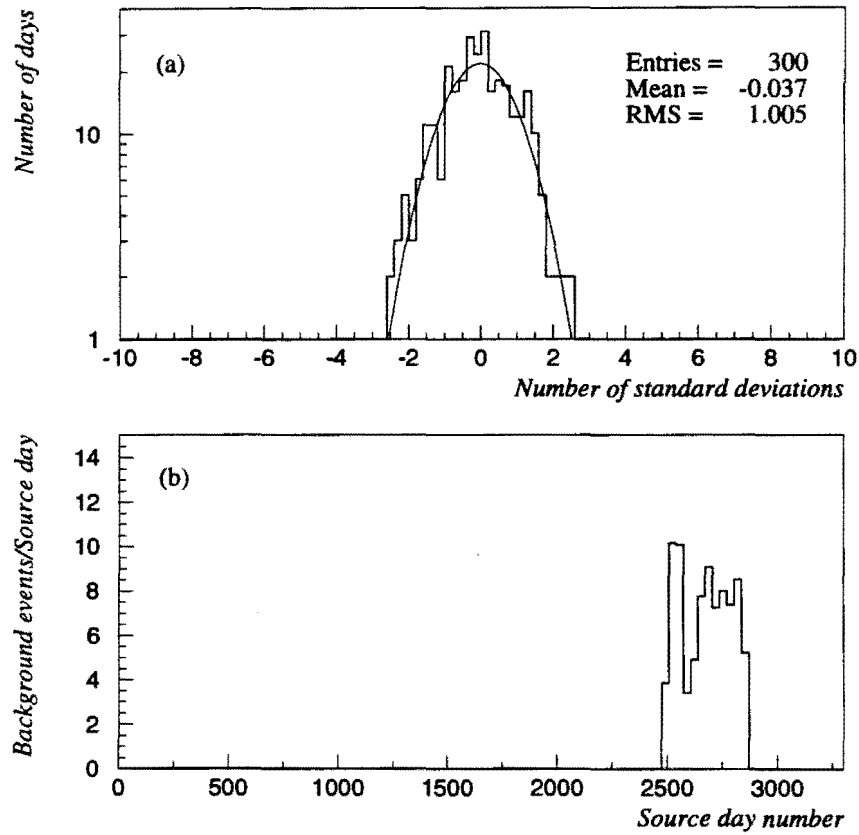


Figure 6.16: (a) Distribution of daily sigmas from PSR 1953+29 using all events in JASA dataset. The solid line is a best fit to a Gaussian distribution. (b) Number of calculated background events. The counts have been averaged over 30-day intervals.

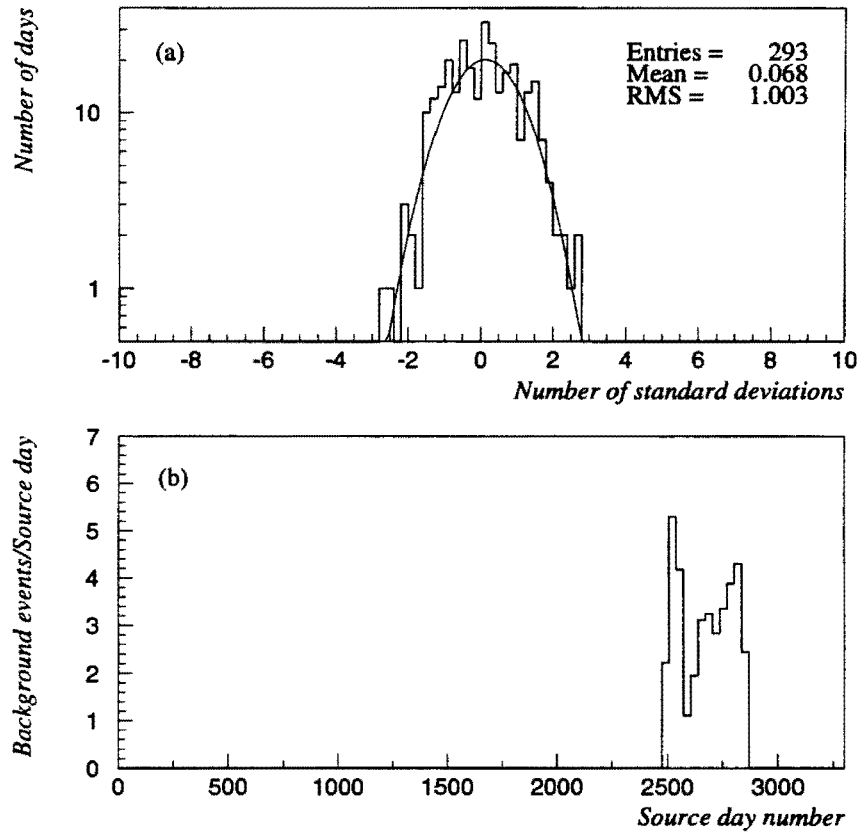


Figure 6.17: (a) Distribution of daily sigmas from PSR 1953+29 using μ -poor events in the JASA dataset. The solid line is a best fit to a Gaussian distribution. (b) Number of calculated background events. The counts have been averaged over 30-day intervals.

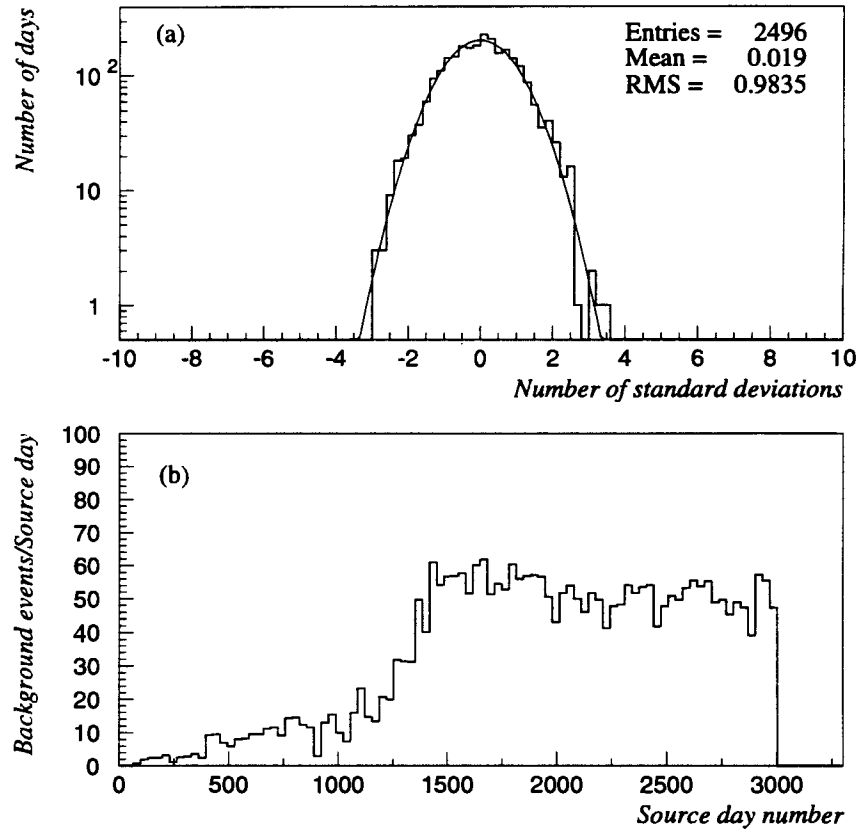


Figure 6.18: (a) Distribution of daily sigmas from PSR 1957+20 using all events in the CYGNUS-I dataset. The solid line is a best fit to a Gaussian distribution. (b) Number of calculated background events. The rise in the number of background events per source day represents the changes in experimental configurations, as described in Sec. 3.2. The counts have been averaged over 30-day intervals.

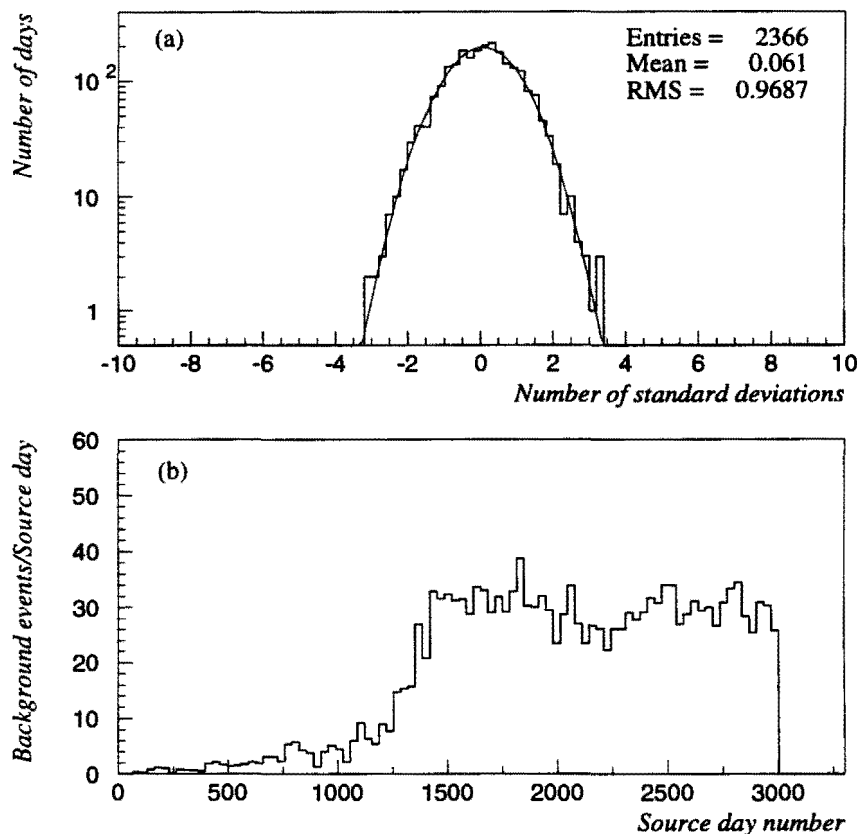


Figure 6.19: (a) Distribution of daily sigmas from PSR 1953+29 using μ -poor events in the CYGNUS-I dataset. The solid line is a best fit to a Gaussian distribution. (b) Number of calculated background events. The rise in the number of background events per source day represents the changes in experimental configurations, as described in Sec. 3.2. The counts have been averaged over 30-day intervals.

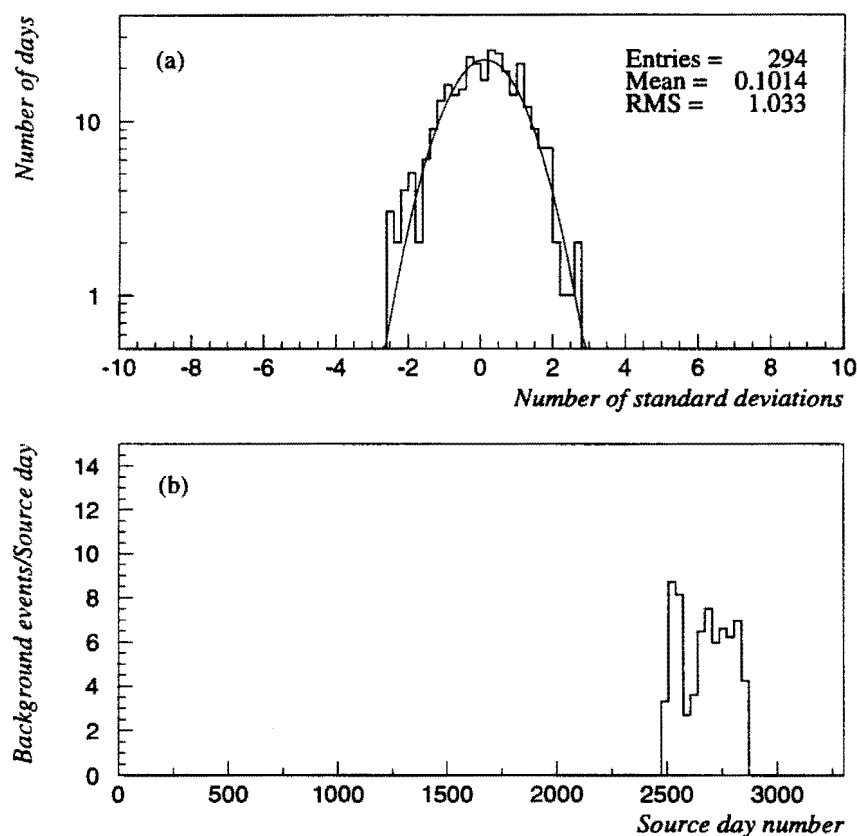


Figure 6.20: (a) Distribution of daily sigmas from PSR 1953+29 using all events in JASA dataset. The solid line is a best fit to a Gaussian distribution. (b) Number of calculated background events. The counts have been averaged over 30-day intervals.

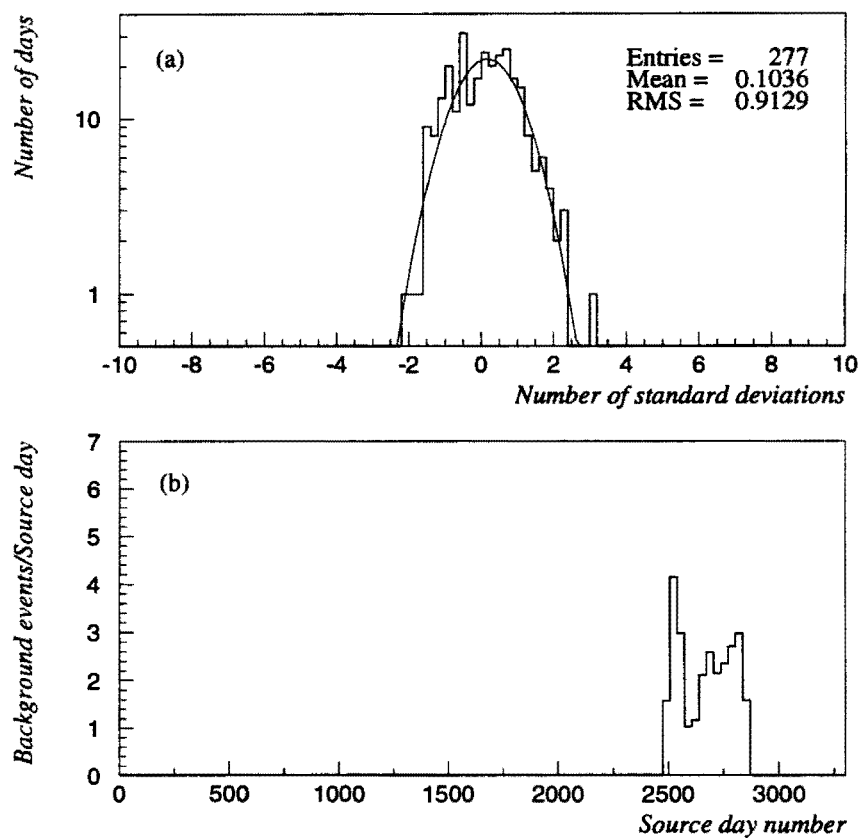


Figure 6.21: (a) Distribution of daily sigmas from PSR 1953+29 using μ -poor events in the JASA dataset. The solid line is a best fit to a Gaussian distribution. (b) Number of calculated background events. The counts have been averaged over 30-day intervals.

6.4 Search for Pulsed Emission

All the event arrival times are corrected to the SSB using the JPL DE200 ephemeris [138]. For binary systems, the shift of arrival times due to the orbital motion is also removed (see Sec. 5.5.2). The γ -ray light curves of the pulsars examined, except that of the Crab pulsar, are not well-known. Their radio light curves have narrow peaks and/or have multiple structures. The Z_{10}^2 test is therefore chosen to test the nature of narrow and multiple peaks for all the sources except the Crab.

The Crab pulsar has a main peak with a second peak 0.4 phase away in the light curves from radio to γ -rays. Monte Carlo simulations are used to determine the best statistic from Z_1^2 to Z_{10}^2 on a simulated dataset containing 9000 background events and the following light curves:

- a single peak ($\sim 2.5 \sigma$ above the background) with a width of 10%.
- a main peak ($\sim 2.5 \sigma$ above the background) with a width of 10% and a second peak ($\sim 2.5 \sigma$ on top of the background) 0.4 phase away with the same width.
- a main peak ($\sim 2.5 \sigma$ above the background) with a width of 10% and a second peak ($\sim 1 \sigma$ on top of the background) 0.4 phase away with the same width.

In all cases, the Z_5^2 test has the best sensitivity to emission. Hence the Z_5^2 test is selected to test the uniformity of the Crab data.

Long-Term Results

Due to the measurement errors of the pulsar ephemerides, the phase errors propagated over the time window of the searched events may amount to be large. The Crab pulsar is observed monthly by Jodrell Bank [78]; its maximum phase errors in a month are less than 0.01. The period of PSR 1937+21 is measured to a very precise level; its phase error amounts to less than four parts in ten thousand after propagating over the period of time of the CYGNUS-I data. Hence the Z_n^2 test are applied to the coherent sum of all the phases for these two pulsars. The other three pulsars have larger phase errors, ranging from 0.04 to 0.5, after propagating over the period of time of the CYGNUS-I data. Therefore, an incoherent sum of the phases is used to evaluate the chance probabilities of pulsed emission from these three pulsars. The method is described as follows: First, the data are segmented into source days. In each source day, the Z_n^2 test is applied if there are two or more EAS events coming from the source direction, and then the chance probability is calculated for that day. After the probabilities of all the qualified source days are accumulated, the overall probability can be obtained from the method described in Sec. 5.7.

Phasograms for the pulsars are shown in Figs. 6.22–6.31. The most significant chance probability level of the Z_n^2 tests from four categories of the five pulsars is 2.6%, from PSR 1953+29 in its JASA all-event data. The trials factor for picking up the more significant result from all-event and muon-poor data is found to be 1.6 using the Monte Carlo method, and the trials factor for choosing from the CYGNUS-I and the JASA data is 1.95. After the trials factor of $5 \times 1.6 \times 1.95 = 15.6$ is considered, the final post-trials probability becomes 33.7%.

One can see a peak at phase 0–0.2 in the JASA muon-poor data of PSR 1937+21 in Fig. 6.25 (b), which is a 3.66σ excess (pre-trials chance probability = 1.2×10^{-4}) if the background is taken as the average of the phases in all bins. The coherent sum of the phases for this pulsar is used in the Z_{10}^2 test. The trials factor, found by Monte Carlo simulations, for choosing the most significant peak from a 10-bin phasogram is ~ 14 , if one allows the bin width of the peak to vary. The above trials factor of 15.6 also needs to be applied. An additional trials factor of 2 has to be added to account for the fact that the result is tested by two different statistical tests. The final post-trials probability then increases to 5.1%, which is not statistically significant. Therefore, all the observational results indicate that the effects seen are consistent with the background fluctuations. The results are listed in Tables 6.5–6.6.

Single-Day Results

There are about 1100 (300) days in the CYGNUS-I (JASA) data for pulsed analysis. In order to reduce the trials penalty, the search for periodicity on the daily basis is only performed over the more probable days on which the unpulsed search shows an excess of 2σ or more. The *a priori* choice of 2σ is arbitrary. The search strategy is to pick the days with standard deviation $\sigma \geq 2$ from the results of unpulsed daily search, and then the Z_n^2 ($n = 5$ for the Crab pulsar and $n = 10$ for the other pulsars) test is applied on those days for each source. The pre-trials probability P_{pre} for each source will be assessed a trials factor N_D to account for the N_D days searched for periodicity to get the post-trials probability P_{post} for that source. The lowest probability P_{post} is 1.3%, coming from the CYGNUS-I muon-

poor data of PSR 1951+32. Additional trials factors should be assessed to account for the choice from five pulsars (trials factor = 5), for the choice from the all-event data and the muon-poor event data (trials factor = 1.6) and for the choice from the CYGNUS-I data and the JASA data (trials factor = 1.95). The final post-trials probability then becomes 18.5%. Therefore, no compelling evidence of single-day pulsed emissions has been found from any of the five pulsars in both datasets. Tables 6.7–6.8 give the results.

Source	All events			μ -poor events		
	N_D	S	P	N_D	S	P
Crab	–	3.04	0.98	–	5.27	0.86
PSR 1937+21	–	26.40	0.15	–	20.38	0.43
PSR 1951+32	1035	2031.5	0.72	1025	2067.6	0.39
PSR 1953+29	1031	2147.6	0.092	1017	2079.1	0.24
PSR 1957+20	1026	1959.7	0.93	1014	1962.1	0.85

Table 6.5: Results of searching for long-term pulsed emission using the CYGNUS-I dataset. N_D is the number of days with 2 or more events falling in the source region, S is the power of Z_n^2 test on all phases for the Crab and PSR 1937+21 or $S = -2 \ln(\prod_{i=1}^{N_D} P_i)$ for the remaining 3 pulsars, where P_i is the probability of the Z_n^2 test of the i th day ($n = 5$ for the Crab and $n = 10$ for the remaining sources), and P is the overall pre-trials probability as described in the text.

Source	All events			μ -poor events		
	N_D	S	P	N_D	S	P
Crab	–	15.38	0.12	–	7.64	0.66
PSR 1937+21	–	17.06	0.65	–	31.52	0.049
PSR 1951+32	293	591.0	0.43	262	518.4	0.56
PSR 1953+29	293	654.6	0.026	256	545.2	0.15
PSR 1957+20	289	561.3	0.68	230	485.2	0.20

Table 6.6: Results of searching for long-term pulsed emission using the JASA dataset. N_D is the number of days with 2 or more events falling in the source region, S is the power of Z_n^2 test on all phases for the Crab and PSR 1937+21 or $S = -2 \ln(\prod_{i=1}^{N_D} P_i)$ for the remaining 3 pulsars, where P_i is the probability of the Z_n^2 test of the i th day ($n = 5$ for the Crab and $n = 10$ for the remaining sources), and P is the overall pre-trials probability as described in the text.

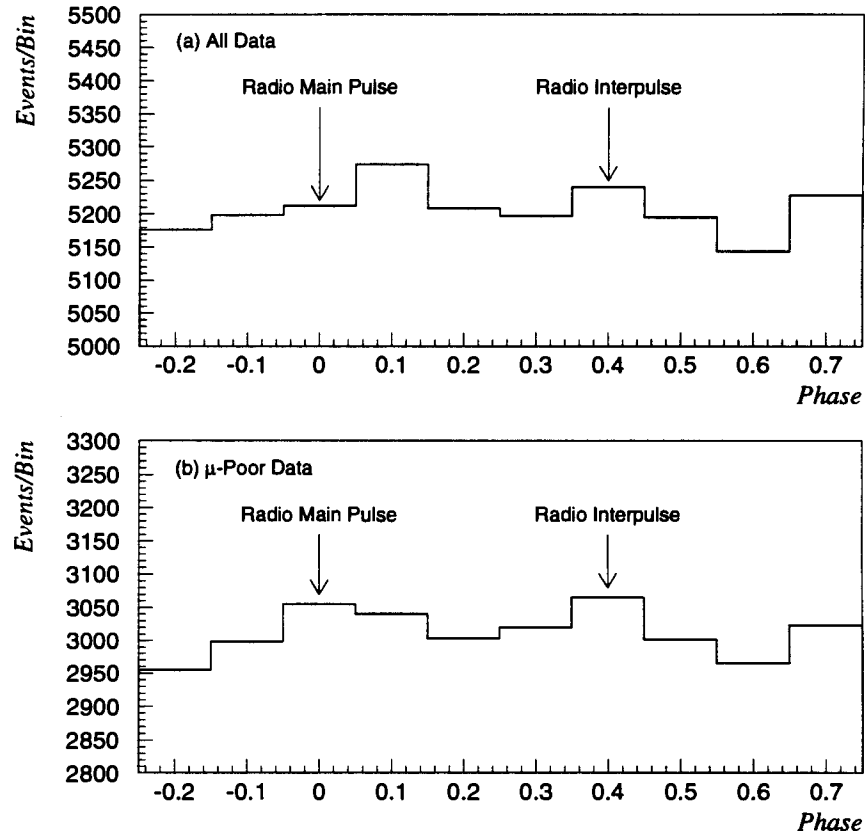


Figure 6.22: The Crab pulsar phasograms for long-term pulsed emission search using the CYGNUS-I dataset. (a) For all events. (b) For μ -poor events. The coherent sum of these phases is used in the Z_5^2 test.

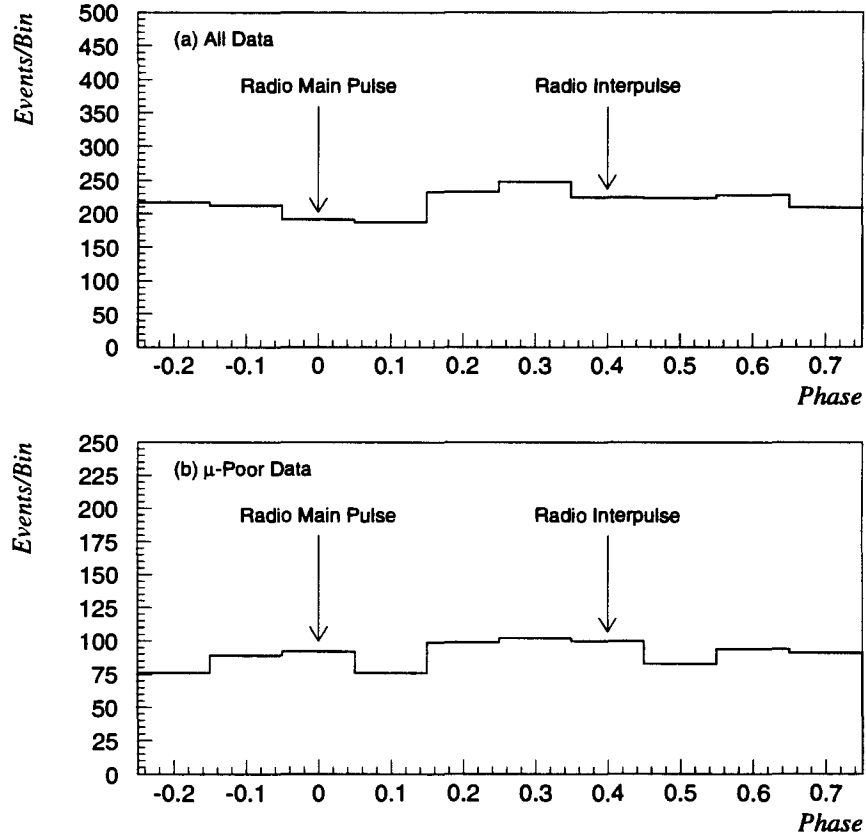


Figure 6.23: The Crab pulsar phasograms for long-term pulsed emission search using the JASA dataset. (a) For all events. (b) For μ -poor events. The coherent sum of these phases is used in the Z_5^2 test.

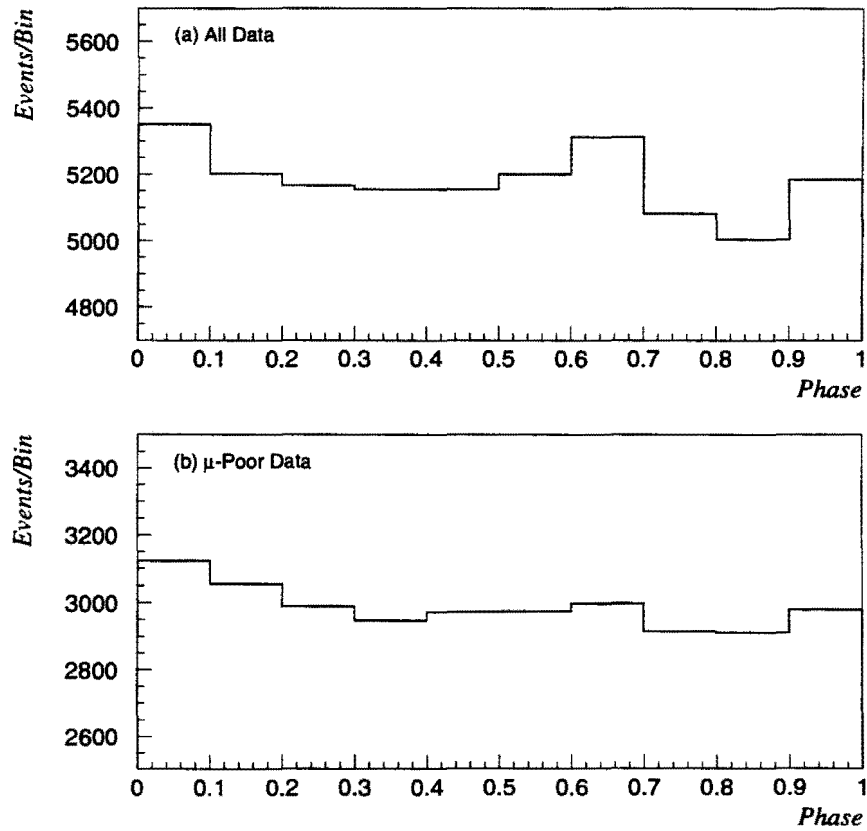


Figure 6.24: PSR 1937+21 phasograms for long-term pulsed emission search using the CYGNUS-I dataset. (a) For all events. (b) For μ -poor events. The coherent sum of these phases is used in the Z_{10}^2 test.

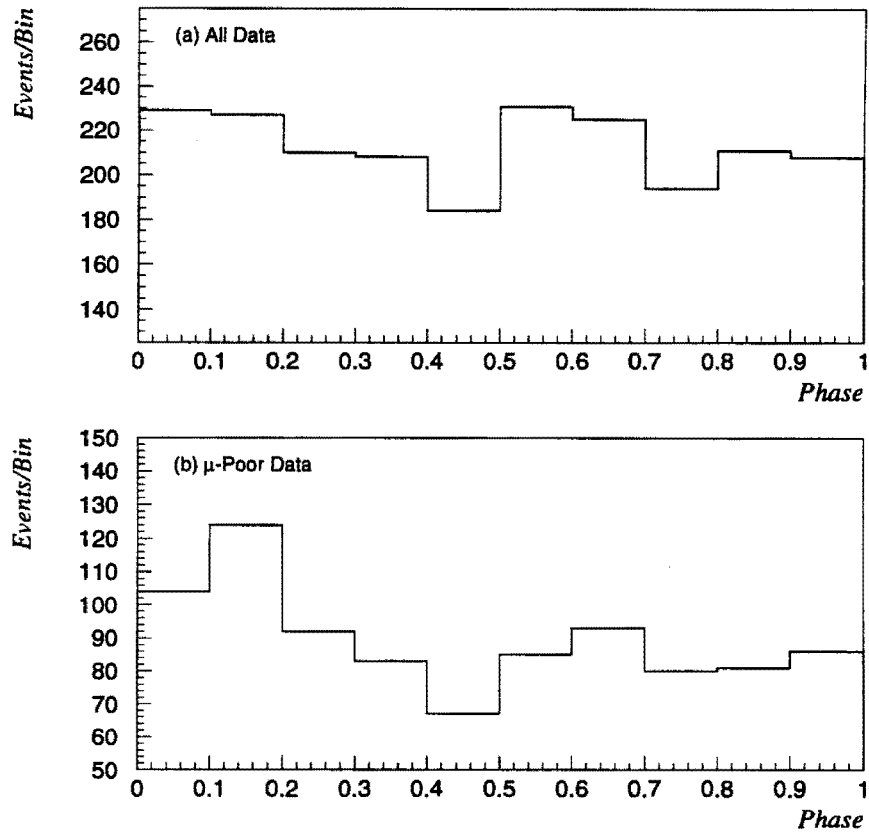


Figure 6.25: PSR 1937+21 phasograms for long-term pulsed emission search using the JASA dataset. (a) For all events. (b) For μ -poor events. The coherent sum of these phases is used in the Z_{10}^2 test.

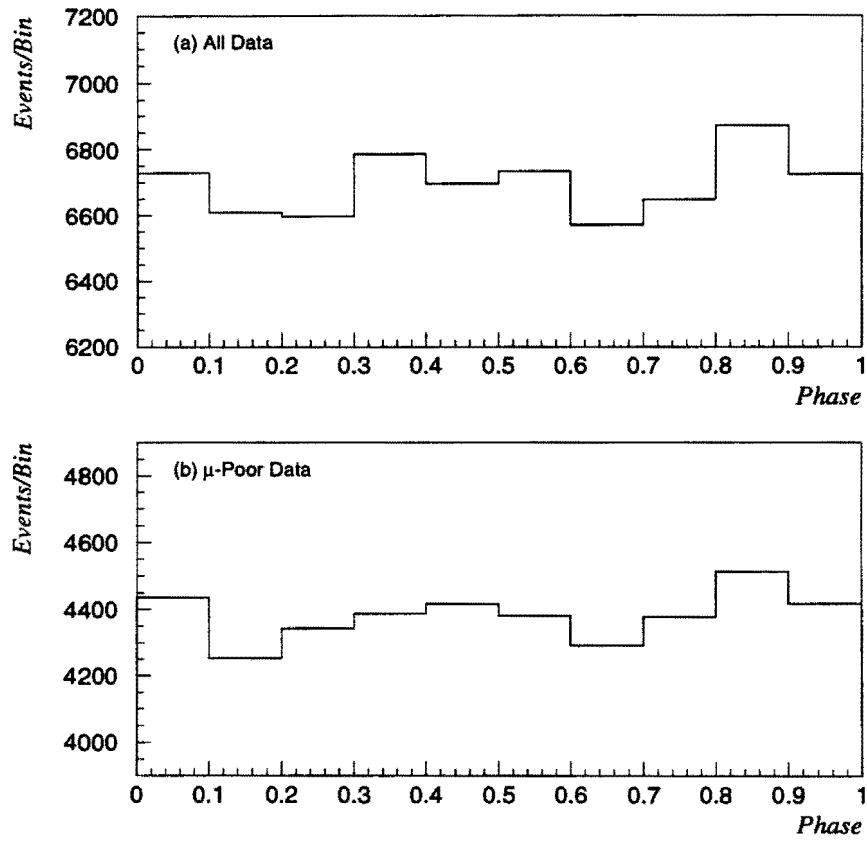


Figure 6.26: PSR 1951+32 phasograms for long-term pulsed emission search using the CYGNUS-I dataset. (a) For all events. (b) For μ -poor events. The incoherent sum of these phases is used in the Z_{10}^2 test.

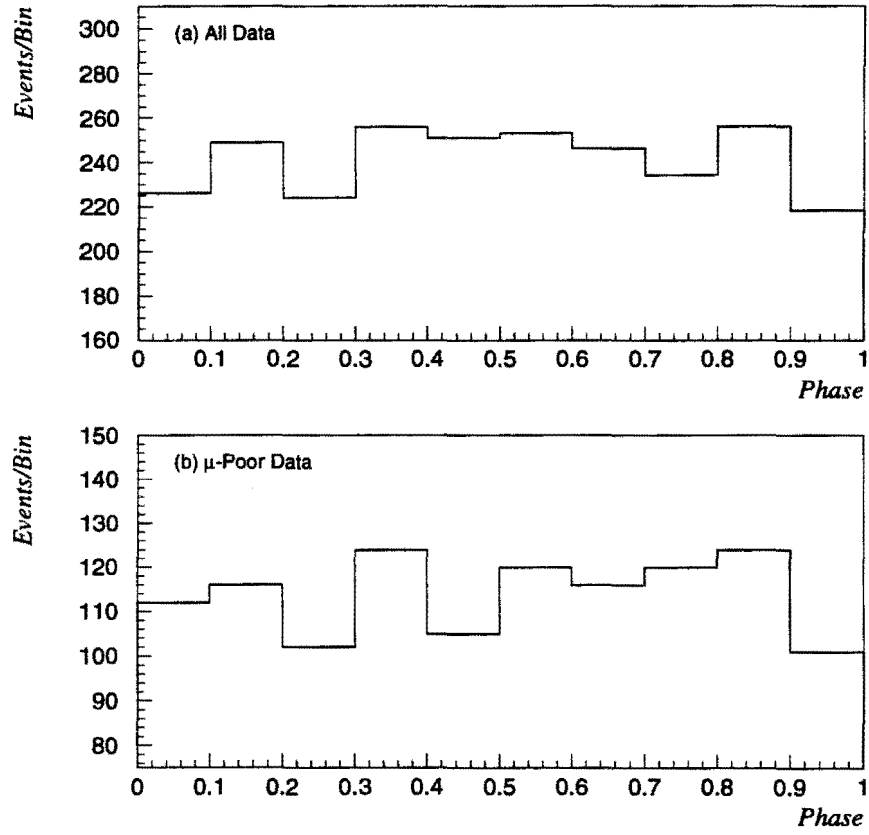


Figure 6.27: PSR 1951+32 phasograms for long-term pulsed emission search using the JASA dataset. (a) For all events. (b) For μ -poor events. The incoherent sum of these phases is used in the Z_{10}^2 test.

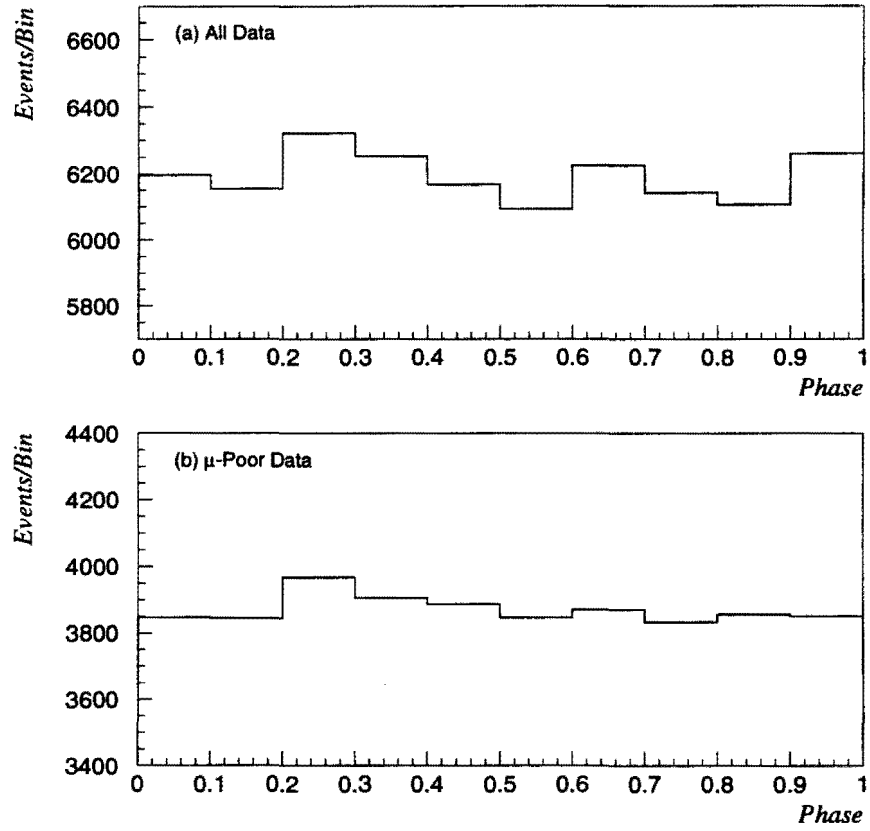


Figure 6.28: PSR 1953+29 phasograms for long-term pulsed emission search using the CYGNUS-I dataset. (a) For all events. (b) For μ -poor events. The incoherent sum of these phases is used in the Z_{10}^2 test.

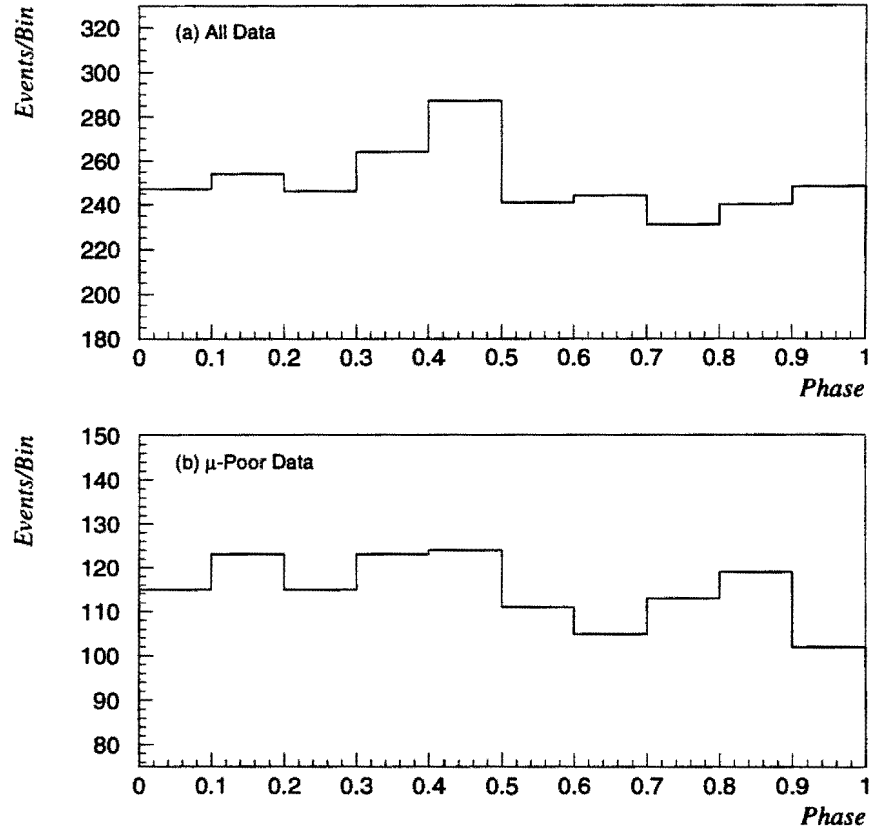


Figure 6.29: PSR 1953+29 phasograms for long-term pulsed emission search using the JASA dataset. (a) For all events. (b) For μ -poor events. The incoherent sum of these phases is used in the Z_{10}^2 test.

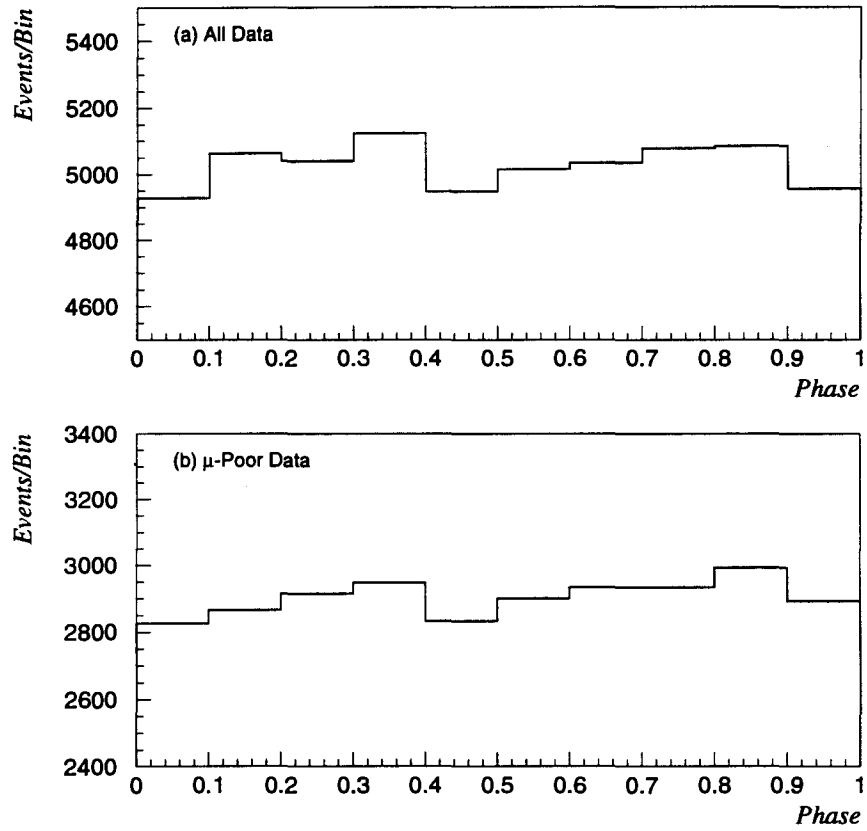


Figure 6.30: PSR 1957+20 phasograms for long-term pulsed emission search using the CYGNUS-I dataset. (a) For all events. (b) For μ -poor events. The incoherent sum of these phases is used in the Z_{10}^2 test.

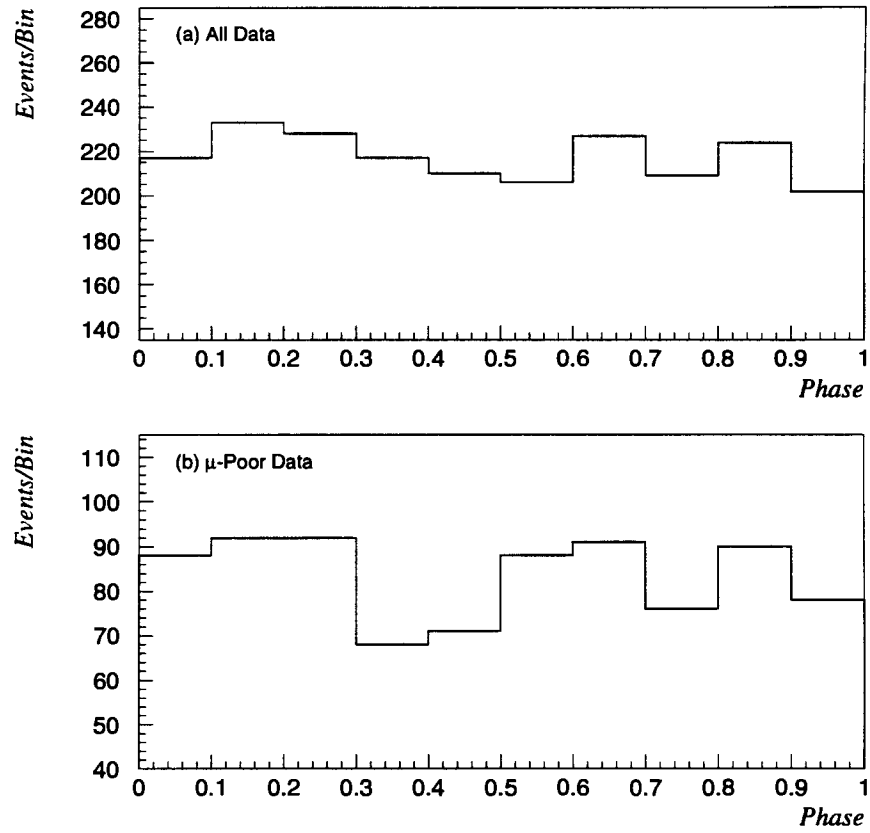


Figure 6.31: PSR 1957+20 phasograms for long-term pulsed emission search using the JASA dataset. (a) For all events. (b) For μ -poor events. The incoherent sum of these phases is used in the Z_{10}^2 test.

(a) All events

Source	N_s	Z_n^2	P_{pre}	N_D	P_{post}
Crab	73	19.65	0.032	8	0.23
PSR 1937+21	80	29.35	0.081	5	0.34
PSR 1951+32	67	16.41	0.69	1	0.69
PSR 1953+29	94	27.74	0.12	3	0.31
PSR 1957+20	62	26.41	0.15	6	0.62

(b) μ -poor events

Source	N_s	Z_n^2	P_{pre}	N_D	P_{post}
Crab	49	13.17	0.21	6	0.76
PSR 1937+21	44	26.55	0.15	4	0.47
PSR 1951+32	42	40.96	0.0033	4	0.013
PSR 1953+29	60	21.87	0.35	4	0.82
PSR 1957+20	44	23.80	0.25	5	0.76

Table 6.7: Results of searching for the single-day pulsed emission for the most significant day using the CYGNUS-I dataset. Quoted are N_s , the number of events within the source bin, Z_n^2 , the power of Z_n^2 test where $n = 5$ for the Crab and $n = 10$ for the rest, P_{pre} , the pre-trials probability before any trials factor is assessed, N_D , the number of days searched for periodicity, and P_{post} , the post-trials probability after N_D days for that source have been considered. Only days with standard deviation $\sigma \geq 2$ from the unpulsed daily results are searched.

(a) All events

Source	N_s	Z_n^2	P_{pre}	N_D	P_{post}
Crab	13	14.46	0.14	6	0.60
PSR 1937+21	15	37.25	0.012	7	0.081
PSR 1951+32	14	26.40	0.14	4	0.45
PSR 1953+29	21	33.83	0.025	6	0.14
PSR 1957+20	9	24.61	0.19	6	0.72

(b) μ -poor events

Source	N_s	Z_n^2	P_{pre}	N_D	P_{post}
Crab	8	19.97	0.025	6	0.14
PSR 1937+21	12	16.50	0.70	4	0.99
PSR 1951+32	9	26.40	0.13	4	0.43
PSR 1953+29	10	25.69	0.16	7	0.70
PSR 1957+20	10	26.96	0.12	6	0.54

Table 6.8: Results of searching for the single-day pulsed emission for the most significant day using the JASA dataset. Quoted are N_s , the number of events within the source bin, Z_n^2 , the power of Z_n^2 test where $n = 5$ for the Crab and $n = 10$ for the rest, P_{pre} , the pre-trials probability before any trials factor is assessed, N_D , the number of days searched for periodicity, and P_{post} , the post-trials probability after N_D days for that source have been considered. Only days with standard deviation $\sigma \geq 2$ from the unpulsed daily results are searched.

6.5 Summary

The CYGNUS-I and the JASA datasets from the CYGNUS extensive air-shower experiment have been searched for unpulsed and pulsed emissions from the directions of the Crab, PSR 1937+21, PSR 1951+32, PSR 1953+29 and PSR 1957+20. The CYGNUS-I data cover the dates from 1986 April 2 to 1994 March 7 and the JASA data cover the period from 1991 February 27 through 1993 October 23.

For the search for long-term unpulsed emission, the most significant result of 2.3σ comes from the JASA all-event data of PSR 1957+20. This corresponds to a chance probability of 11.7% after accounting for all degrees of freedom, and we are unable to reject the null hypothesis. The daily search for unpulsed emissions from this source gives a 68.4% post-trials probability, also consistent with the null hypothesis. Therefore, no statistically significant excesses for long-term unpulsed emission or sporadic emission on the time scale of one source day are found in any of the datasets examined from the directions of the five fast pulsars. Flux upper limits for steady flux from each source are calculated at the 90% CL above the medium energy $E = 100$ TeV of the CYGNUS experiment. The steady flux upper limits from the CYGNUS-I all-event (muon-poor) results are 3.0 (2.2), 2.6 (1.5), 1.3 (1.2), 1.4 (0.9), and $3.2 (2.4) \times 10^{-14}$ photons $\text{cm}^{-2} \text{s}^{-1}$ for the Crab, PSR 1937+21, PSR 1951+32, PSR 1953+29, and PSR 1957+20, respectively.

The above quoted limits are taken from the CYGNUS-I data because the observational window of the CYGNUS-I dataset is much longer than that of the JASA dataset. The limit will closely depend on the number of observed source events and the number of expected background events, i.e. on the observed excess or deficit. If the same number of standard deviations from the same length datasets

are compared, the JASA array has a sensitivity to point source emission that is ~ 1.4 times better than the CYGNUS-I array if the all-event data or the muon-poor data are used. If the true signal (γ -ray) events were observed, the standard deviation obtained from the JASA data would be 2 times higher than that obtained from the CYGNUS-I data, due to the better angular resolution of the JASA array. The use of the water-Čerenkov array definitely helps improve the sensitivity of the CYGNUS experiment.

For the long-term periodicity search, a 33.7% post-trials probability is observed from the JASA all-event data of PSR 1953+29. It is not statistically significant and, therefore, is consistent with the background fluctuations. Days showing 2σ or more excess in the unpulsed search are examined for the periodicity on the time scale of one source day. The 18.5% post-trials chance probability from the CYGNUS-I muon-poor data of PSR 1951+32 is too high to reject the null hypothesis. Hence no strong evidence for long-term or single-day periodic signals is found at the radio period in any of the datasets for the five pulsars examined in this work.

When the measured integral Crab spectra are linearly extrapolated to 100 TeV (see Eq. 2.7–2.9), the flux upper limits given for the Crab in this work are below the old Whipple’s spectrum and the THEMISTOCLE’s spectrum, but above the new Whipple’s spectrum. If the old Whipple’s spectrum or the THEMISTOCLE’s spectrum is correct, then the Crab flux should be detectable by the CYGNUS experiment, unless there is a flux cutoff at about 10 TeV. If the new Whipple’s spectrum is correct, then the CYGNUS experiment is unable to see the Crab.

The flux upper limits given for PSR 1937+21 in this analysis are lower, if compared with the same confidence level and assuming an integral spectral index

of -1.7 , than the upper limits of EAS-TOP ($= 2.2 \times 10^{-13}$ photons $\text{cm}^{-2} \text{s}^{-1}$ at the 95% CL and $E > 150$ TeV), Plateau Rose Station ($= 6.3 \times 10^{-12}$ photons $\text{cm}^{-2} \text{s}^{-1}$ at the 95% CL and $E > 30$ TeV), HEGRA ($= 1.9 \times 10^{-13}$ photons $\text{cm}^{-2} \text{s}^{-1}$ at the 90% CL and $E > 70$ TeV) and BASA ($= 1.5 \times 10^{-13}$ photons $\text{cm}^{-2} \text{s}^{-1}$ at the 90% CL and $E > 200$ TeV), as described in Sec. 2.4.2. The pulsed emission detected at the radio period of PSR 1937+21 by the Durham group [89] is not observed by the CYGNUS experiment. The Durham observation was made during 1984, which is outside the range of the CYGNUS data, hence the emission could be sporadic. Since the detection was at the 10^{-4} chance probability level above 1 TeV, it did not rule out the possibility that the result was entirely due to the background fluctuation.

If one naively extrapolates the pulsed energy spectrum of PSR 1951+32 measured by EGRET [101] to 100 TeV, the integral pulsed flux of 6×10^{-12} photons $\text{cm}^{-2} \text{s}^{-1}$ at $E \geq 100$ TeV is certainly within the detection range of the CYGNUS experiment. Here, the differential spectral index measured by EGRET is -1.74 . However, the source spectral index at TeV energy range is typically steeper than that at MeV range. Therefore, PSR 1951+32 can be out of the detection range of the CYGNUS experiment.

The flux upper limits given for PSR 1953+29 in this analysis is lower, if compared with the same confidence level and assuming an integral spectral index of -1.7 , than the upper limits of EAS-TOP ($= 2.2 \times 10^{-13}$ photons $\text{cm}^{-2} \text{s}^{-1}$ at the 95% CL and $E > 150$ TeV), Plateau Rose Station ($= 4.8 \times 10^{-12}$ photons $\text{cm}^{-2} \text{s}^{-1}$ at the 95% CL and $E > 30$ TeV), HEGRA ($= 2.2 \times 10^{-13}$ photons $\text{cm}^{-2} \text{s}^{-1}$ at the 90% CL and $E > 60$ TeV) and BASA ($= 1.2 \times 10^{-13}$ photons $\text{cm}^{-2} \text{s}^{-1}$ at the 90%

CL and $E > 200$ TeV), as described in Sec. 2.4.4. The detection of pulsed TeV γ -rays at the radio period from PSR 1953+29, at the 5.4σ level as reported by the Durham group [90], is not seen in the CYGNUS data. Their observation was made during 1983–1984, which is outside the range of the CYGNUS observation window. If one assumes the source spectral index is the same as the cosmic-ray spectral index (integral spectral index = -1.7), the reported flux (> 2 TeV) of 3×10^{-11} photons $\text{cm}^{-2} \text{s}^{-1}$ is calculated to be 3.9×10^{-14} photons $\text{cm}^{-2} \text{s}^{-1}$ at $E > 100$ TeV. This flux is too weak to be observable by the CYGNUS experiment.

The flux upper limits given for PSR 1957+20 in this analysis is lower, if compared with the same confidence level and assuming an integral spectral index of -1.7 , than the upper limits of HEGRA ($= 8.4 \times 10^{-14}$ photons $\text{cm}^{-2} \text{s}^{-1}$ at the 90% CL and $E > 70$ TeV) and Ooty ($= 4 \times 10^{-13}$ photons $\text{cm}^{-2} \text{s}^{-1}$ at the 99% CL and $E > 100$ TeV), as described in Sec. 2.4.5. The Durham group showed a possible periodic emission at the radio period from PSR 1957+20 [110]. The chance probability level was 4.1×10^{-3} and they are not able to claim a firm detection. The CYGNUS data does not show any evidence of pulsed signal from PSR 1957+20. Therefore, the observed periodicity was highly possible to emerge from the background fluctuation.

In conclusion, the analysis does not show a compelling evidence of unpulsed or pulsed emissions from any of the sources examined. This can be due to any of the following causes, or their combinations: 1) The sources do not have any emissions during the time period searched; 2) The signals at the CYGNUS energy range are too weak to be detected; 3) The past positive observations of TeV emissions were not true; 4) The past observations of significance were true but due to background

fluctuations; 5) The past detections were true, but there is probably a signal cutoff at about 10 TeV, which is beyond the sensitivity of the CYGNUS experiment. Therefore, this work does not find and confirm the signal detections claimed by other experiments.

Bibliography

- [1] Lewis, D. A., et al., Proc. 23rd Inter. Cosmic Ray Conf. (Calgary) **1**, 279 (1993).
- [2] Haines, T. J., Proc. 23rd Inter. Cosmic Ray Conf., Invited, Rapporteur & Highlight Papers (Calgary), p. 341 (1994).
- [3] Nagle, D. E., et al., Ann. Rev. Nucl. Part. Sci. **38**, 609 (1988).
- [4] Coteus, P., and de Grand, T., Phys. Rev. D **33**, 3279 (1986).
- [5] Stanev, T., et al., Phys. Lett. **158B**, 75 (1985).
- [6] Stanev, T., et al., Phys. Rev. D **32**, 1244 (1985).
- [7] Edwards, T., et al., J. Phys. G **11**, L101 (1985).
- [8] Fegan, D. J., Proc. 21st Inter. Cosmic Ray Conf. (Adelaide) **11**, 23 (1990).
- [9] Chadwick, P. M., et al., J. Phys. G: Nucl. Part. Phys. **16**, 1773 (1990).
- [10] Weekes, T. C., Space Sci. Rev. **59**, 315 (1992).
- [11] Alexeenko, V. V., et al., Proc. Inter. Workshop on VHE and UHE Gamma Ray Astronomy (Crimea, USSR), p. 187 (1989).
- [12] Sinha, S., et al., Proc. 21st Inter. Cosmic Ray Conf. (Adelaide) **2**, 366 (1990).
- [13] Aglietta, M., et al., Proc. Inter. Workshop on VHE and UHE Gamma Ray Astronomy (Crimea, USSR), p. 60 (1989).
- [14] Baillon, P., et al., Proc. 23rd Inter. Cosmic Ray Conf. (Calgary) **1**, 271 (1993).
- [15] Dingus, B. L., et al., Phys. Rev. Lett. **61**, 1906 (1988).

- [16] Lamb, R. C., et al., *Ap. J. Lett.* **328**, L13 (1988).
- [17] Resvanis, L. K., et al., *Ap. J. Lett.* **328**, L9 (1988).
- [18] Gupta, S. K., et al., *Ap. J. Lett.* **354**, L13 (1990).
- [19] Weekes, T. C., et al., *Ap. J.* **342**, 379 (1989).
- [20] Vacanti, G., et al., *Ap. J.* **377**, 467 (1991).
- [21] Reynolds, P. T., *Ap. J.* **404**, 206 (1993).
- [22] Hewish, A., et al., *Nature* **217**, 709 (1968).
- [23] Taylor, J. H., et al., *Ap. J. Suppl. Series* **88**, 529 (1993).
- [24] Kundt, W., *Neutron Stars and Their Birth Events*, ed. by W. Kundt, Dordrecht: Kluwer Academic Publishers, p. 1 (1990).
- [25] Lyne, A. G., and Graham-Smith, F., *Pulsar Astronomy*. Cambridge: Cambridge University Press (1990).
- [26] Shapiro, S. L. and Teukolsky, S. A., *Black Holes, White Dwarfs, and Neutron Stars. The Physics of Compact Objects*. New York: Wiley (1983).
- [27] Alpar, M. A., Anderson, P. W., Pines, D., and Shaham, J., *Ap. J.* **276**, 325 (1984).
- [28] Alpar, M. A., Anderson, P. W., Pines, D., and Shaham, J., *Ap. J.* **278**, 791 (1984).
- [29] Seward, F. D. and Wang, Z.-R., *Ap. J.* **332**, 199 (1988).
- [30] Manchester, R. N., and Taylor J. H., *Pulsars*. San Francisco: W. H. Freeman and Company (1977).
- [31] Abt, H. A., *Ann. Rev. Astron. Astrophys.* **21**, 343 (1983).
- [32] Boriakoff, V., et al., *Green Bank Workshop on Millisecond Pulsars*, ed. S. P. Reynolds, D. R. Stinebring, pp. 271–275. Green Bank WV: Natl. Radio Astron. Obs. (1984).
- [33] Damashek, M., et al., *Ap. J. Lett.* **253**, L57 (1982).
- [34] Hulse, R. A., and Taylor J. H., *Ap. J. Lett.* **195**, L51 (1975).
- [35] Manchester, R. N., et al., *MNRAS* **185**, 409 (1978).

- [36] Stokes, G. H., et al., *Ap. J. Lett.* **294**, L21 (1985).
- [37] Lang, K. R., *Astrophysical Formulae*. Berlin: Springer-Verlag (1974).
- [38] Alpar, M. A., et al., *Nature* **300**, 728 (1982).
- [39] Beskin, V. S., et al., *Physics of the Pulsar Magnetosphere*. Cambridge: Cambridge University Press (1993).
- [40] Sorrell, W. H., *Neutron Stars and Their Birth Events*, ed. by W. Kundt, Dordrecht: Kluwer Academic Publishers, pp. 121–126 (1990).
- [41] Fazio, G. G., et al., *Ap. J. Lett.* **175**, L117 (1972).
- [42] Ramana Murthy, P. V., and Wolfendale, A. W., *Gamma-Ray Astronomy*, 2nd ed. Cambridge: Cambridge University Press (1993).
- [43] Akerlof, C. W., et al., *Proc. GRO Science Workshop (Goddard)*, ed. W. N. Johnson, pp. 4–49 (1989).
- [44] Chudakov, A. E., et al., *Trans. Consultants Bureau* **26**, 99 (1965).
- [45] Mukanov, J. B., *Izv. Krymsk. Astrofiz. Obs.* **67**, 55 (1983).
- [46] Tümer, O. T., et al., *Nucl. Phys. B (Proc. Suppl.)* **14A**, 176 (1990).
- [47] Dzikowski, T., et al., *J. Phys. G* **9**, 459 (1983).
- [48] Boone, J., et al., *Ap. J.* **285**, 264 (1984).
- [49] Ko, S., et al., *Proc. 21st Inter. Cosmic Ray Conf. (Adelaide)* **2**, 131 (1990).
- [50] Gillanders, G. H., et al., *Proc. 21st Inter. Cosmic Ray Conf. (Adelaide)* **2**, 23 (1990).
- [51] Gupta, S. K., et al., *Ap. J.* **245**, 141 (1991).
- [52] Corbato, S. C., et al., *Proc. 21st Inter. Cosmic Ray Conf. (Adelaide)* **2**, 159 (1990).
- [53] Archarya, B. S., et al., *Nature* **347**, 364 (1990).
- [54] The THEMISTOCLE collaboration, *Proc. 24th Inter. Cosmic Ray Conf. (Roma)* **2**, 315 (1995).
- [55] Krennrich, F., et al., *Proc. 23rd Inter. Cosmic Ray Conf. (Calgary)* **1**, 251 (1993).

- [56] Merck, M., et al., Proc. 23rd Inter. Cosmic Ray Conf. (Calgary) **1**, 290 (1993).
- [57] Willmer, M., et al., Proc. 24th Inter. Cosmic Ray Conf. (Roma) **2**, 409 (1995).
- [58] Borione, A., et al., Proc. 23rd Inter. Cosmic Ray Conf. (Calgary) **1**, 286 (1993).
- [59] Borione, A., et al., Proc. 24th Inter. Cosmic Ray Conf. (Roma) **2**, 350 (1995).
- [60] Bowden, C. C. G., et al., Proc. 23rd Inter. Cosmic Ray Conf. (Calgary) **1**, 294 (1993).
- [61] Blake, P. R., et al., Proc. 24th Inter. Cosmic Ray Conf. (Roma) **2**, 413 (1995).
- [62] The EASTOP Collaboration, Proc. 24th Inter. Cosmic Ray Conf. (Roma) **2**, 421 (1995).
- [63] Amenomori, M., et al., Phys. Rev. Lett. **69**, 2468 (1992).
- [64] Goret, P., et al., Astron. Astrophys. **270**, 401 (1993).
- [65] Stepanian, A. A., Nucl. Phys. B (Proc. Suppl.) **39A**, 207 (1995).
- [66] Dion, G. M. Ph.D. Dissertation, University of California, Irvine (1992).
- [67] Biller, S. D. Private communication.
- [68] Baillon, P., et al., Proc. 23rd Inter. Cosmic Ray Conf. (Calgary) **1**, 267 (1993).
- [69] Weekes, T. C., Phys. Rep. **160**, 1 (1988).
- [70] Gupta, S. K., et al., Ap. J. **221**, 268 (1978).
- [71] Gupta, S. K., Ph.D. Dissertation. Unpublished (1983).
- [72] Bhat, P. N., et al., Nature **319**, 127 (1986).
- [73] Gibson, A. I., et al., Nature **296**, 833 (1982).
- [74] Dowthwaite, J. C., Ap. J. Lett. **286**, L35 (1984).
- [75] Tümer, O. T., et al., Proc. 19th Inter. Cosmic Ray Conf. (La Jolla) **1**, 139 (1985).

- [76] Bhat, P. N., et al., Proc. 21st Inter. Cosmic Ray Conf. (Adelaide) **2**, 148 (1990).
- [77] Acharya, B. S., Astron. Astrophys. **258**, 412 (1992).
- [78] Lyne, A. G., and Pritchard, R. S., Jodrell Bank Crab Pulsar Timing Results, Monthly Ephemeris (1994).
- [79] Wilson, R. B., and Fishman, G. J., Ap. J. **269**, 273 (1983).
- [80] Ruderman, M. A., and Shaham, J., Nature **304**, 425 (1983).
- [81] Ruderman, M. A., and Shaham, J., Ap. J. **289**, 244 (1985).
- [82] Jeffrey, L. C., Nature **319**, 384 (1986).
- [83] Blondin, J. M., and Freese K., Nature **323**, 30 (1986).
- [84] Foster, R. S., et al., Ap. J. **378**, 687 (1991).
- [85] Cordes, J. M., and Stinebring, D. R., Ap. J. Lett. **277**, L53 (1984).
- [86] Cordes, J. M., et al., Ap. J. **356**, 243 (1990).
- [87] Kaspi, V. M., et al., Ap. J. **428**, 713 (1994).
- [88] Rawley, L. A., et al., Ap. J. **326**, 947 (1988).
- [89] Bowden, C. C. G., et al., AIP Conference Proc. 220, High-Energy Gamma-Ray Astronomy, ed. J. Matthews. New York: AIP, p. 75 (1991).
- [90] Chadwick, P. M., et al., Nature **317**, 236 (1985).
- [91] Aglietta, M., et al., Proc. 21th Inter. Cosmic Ray Conf. (Adelaide) **2**, 345 (1990).
- [92] Morello, C., et al., Proc. 21th Inter. Cosmic Ray Conf. (Adelaide) **2**, 349 (1990).
- [93] Merck, M., et al., Proc. 23rd Inter. Cosmic Ray Conf. (Calgary) **1**, 361 (1993).
- [94] Alexeenko, V. V., et al., Proc. 23rd Inter. Cosmic Ray Conf. (Calgary) **1**, 369 (1993).
- [95] Storm, R. G., Ap. J. Lett. **319**, L103 (1987).
- [96] Kulkarni, S. R., et al., Nature **331**, 50 (1988).

- [97] Foster, R. S., et al., *Ap. J.* **356**, 243 (1990).
- [98] Ögelman, H., and Buccheri, R., *Astron. Astrophys.* **186**, L17 (1987).
- [99] Li, T. P., et al., *IAUC*, No. 4492 (1987).
- [100] Kulkarni, S. R., *Physics of Neutron Stars and Black Holes*. Universal Academy Press (1988).
- [101] Ramana Murthy, P. V., et al., *Ap. J. Lett.*, in press (1995).
- [102] Boriakoff, V., et al., *Nature* **304**, 417 (1983).
- [103] Fruchter, A. S., et al., *Nature* **333**, 237 (1988).
- [104] Phinney, E. S., et al., *Nature* **333**, 832 (1988).
- [105] Ryba, M. F., and Taylor, J. H., *Ap. J.* **380**, 557 (1991).
- [106] Shapiro, S. L., and Teukolsky, S. A., *Nature*, **333**, 684 (1988).
- [107] Brink, C., et al., *Ap. J. Lett.* **364**, L37 (1990).
- [108] Gupta, S. K., et al., *Astron. Astrophys.* **241**, L21 (1991).
- [109] Sinha, S., et al., *Proc. 21th Inter. Cosmic Ray Conf. (Adelaide)* **2**, 370 (1990).
- [110] Brazier, K. T. S., et al., *Proc. 21th Inter. Cosmic Ray Conf. (Adelaide)* **2**, 304 (1990).
- [111] Cheng, K. S., Ho, C., and Ruderman, M., *Ap. J.* **300**, 500 (1986).
- [112] Cheng, K. S., Ho, C., and Ruderman, M., *Ap. J.* **300**, 522 (1986).
- [113] Kwok, P. W., Cheng, K. S., and Lau, M. M., *Ap. J.* **379**, 653 (1991).
- [114] Cheng, K. S., and Ruderman, M., *Ap. J. Lett.* **337**, L77 (1989).
- [115] Cheng, K. S., and Ruderman, M., *Ap. J.* **373**, 187 (1991).
- [116] Cheng, K. S., et al., *Ap. J.* **379**, 290 (1991).
- [117] Alexandreas, D. E., et al., *Nucl. Instr. Meth.* **A311**, 350 (1992).
- [118] Alexandreas, D. E., et al., *Phys. Rev. D* **43**, 1735 (1991).
- [119] Allen, R. C., et al., *Nucl. Instr. Meth.* **A269**, 177 (1988).
- [120] Allen, R. C., et al., *Nucl. Instr. Meth.* **A311**, 368 (1992).

- [121] Greisen, K., *Ann. Rev. Nucl. Sci.* **10**, 63 (1960).
- [122] Biller, S. D., Ph.D. Dissertation, University of California, Irvine, Los Alamos National Laboratory report LA-UR-93-1428 (1992).
- [123] Sandberg, V. D., et al., *Nucl. Phys. B (Proc. Suppl.)* **14A**, 313 (1990).
- [124] Sinnis, C., Pool Status Report, CYGNUS internal memo (1992).
- [125] Dion, C. L., Pool Analysis Update, CYGNUS internal memo (1992).
- [126] Dion, C. L., Graduate student, Physics Department, University of Maryland, College Park. Private communication.
- [127] Wrotniak, J. A, SHOWERSIM/85, Department of Physics, University of Maryland, College Park.
- [128] Ranucci, G., et al., *Nucl. Instr. Meth.* **A320**, 574 (1992).
- [129] Alexandreas, D. E., et al., *Nucl. Instr. Meth.* **A328**, 570 (1993).
- [130] Li, T.-P., and Ma Y.-Q., *Ap. J.* **272**, 317 (1983).
- [131] Helene, O., *Nucl. Instr. Mech.* **212**, 319 (1983).
- [132] Protheroe, R. J., *Astron. Express* **1**, 33 (1984).
- [133] Alexandreas, D. E., et al., *Ap. J. Lett.* **383**, L53 (1991).
- [134] Burnett, T. H., et al., *Ap. J. Lett.* **349**, L25 (1990).
- [135] Alexandreas, D. E., et al., *Ap. J.* **405**, 353 (1993).
- [136] Backer, D. C., and Hellings, R. W., *Annu. Rev. Astron. Astrophys.* **24**, 537 (1986).
- [137] Ash, M. E., et al., *Ap. J.* **72**, 338 (1967).
- [138] Standish, M., *Astron. Astrophys.* **114**, 297 (1982).
- [139] Nagase, F., *Publ. Astron. Soc. Japan* **41**, 1 (1989).
- [140] Mardia, K. V., *Statistics of Directional Data*. London: Academic (1972).
- [141] De Jager, O. C., Ph.D. Dissertation, Potchefstroom University, South Africa (1987).

- [142] Eadie, W. T., et al., Statistical Methods in Experimental Physics. Amsterdam: North Holland, pp. 282–283 (1971).
- [143] Lewis, D. A., Astron. Astrophys. **219**, 352 (1989).
- [144] Jelley, J. V., Čerenkov Radiation and Its Applications, New York: Pergamon Press, (1958).
- [145] Jackson, J. D., Classical Electrodynamics, 2nd ed., New York: John Wiley & Sons, (1975).
- [146] Phys. Rev. D **50** (1994).

Appendix A

Čerenkov Radiation

A.1 Čerenkov Effect

Suppose a charged particle moves relatively slowly through a piece of transparent medium. Fig. A.1 [144] shows a portion of the medium in which the particle traverses. Track AB is the passage of the particle, and the circles represent the individual atoms of the medium. In the area far from the track of the particle, the atoms are roughly spherical and undistorted. However, in the vicinity of the passing particle at some instance, e.g., at the point P , the particle sets up an electric field which distorts the atoms so that opposite charges of these atoms are displaced to the opposite sides. Hence the medium becomes polarized about the point P . Each element of the medium is polarized in turn along the axis when the particle passes. These elements are symmetrically polarized about the particle, however, so there is no resultant dipole field at large distances and therefore no radiation.

If the particle travels at a velocity comparable to that of light in the medium, the symmetry is still preserved in the azimuthal plane. However, in the direction along the track, the symmetry will break down and there will be a resultant dipole

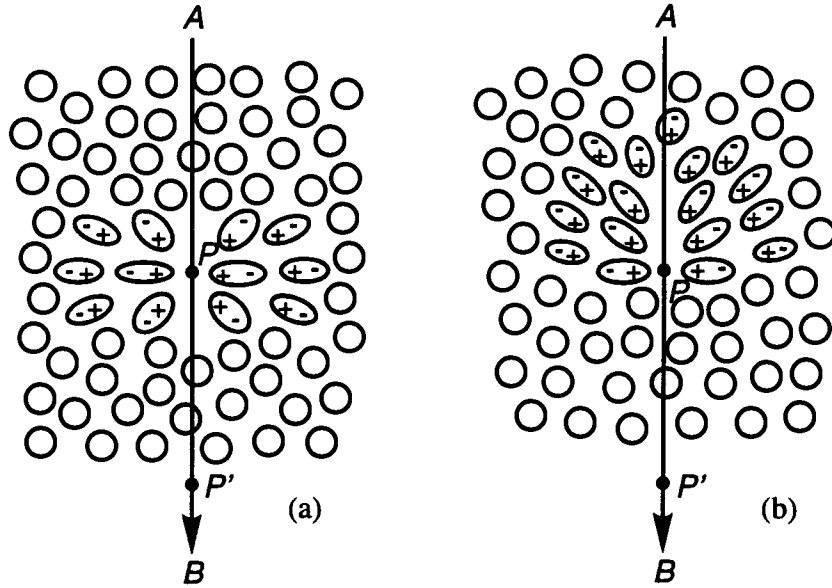


Figure A.1: The polarization induced by the passage of a charged particle. (a) At low velocity; (b) At high velocity. In this example, the particle is negatively charged [144].

field even at far distances. Generally, the radiations from all elements along the passage interfere destructively at a distant point, so that no resultant field will be seen at that point. If, however, the particle moves faster than the phase velocity of light in the medium, it is possible that all the radiated spherical wavelets from the atoms along the axis are in phase at a distant point. Therefore, an electromagnetic shock wave will appear at that point. See Fig. A.2 [145] for the wave propagation according to different velocities.

The Čerenkov angle can be calculated from Fig. A.2(b). If the velocity of

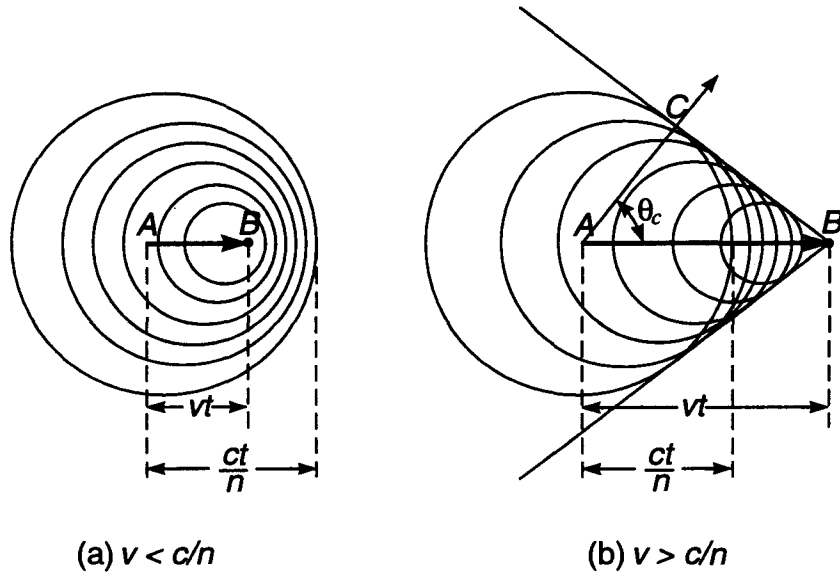


Figure A.2: Čerenkov radiation. Spherical wavelets of fields of a particle traveling (a) less than and (b) greater than the velocity of light in the medium. For $v > c/n$, an electromagnetic shock wave appears, moving in the direction given by the Čerenkov angle θ_c [145].

the particle is βc , where c is the velocity of light in vacuum, then the particle travels a distance $AB = \beta c \cdot t$ in a time t while the shock wavefront travels a distance $AC = (c/n) \cdot t$, where n is the index of refraction of the medium. Also, $AC = AB \cos \theta_c$. From these one yields

$$\cos \theta_c = \frac{1}{\beta n},$$

which is known as the “Čerenkov radiation.”

A.2 Characteristics

Čerenkov detectors exploit one or more features of the Čerenkov radiation. One can set an energy threshold for the particles being detected by tuning the refractive index of the radiator. Since it has to meet $\beta n > 1$, the velocity threshold β_{th} is $1/n$. The Lorentz factor $\gamma = 1/\sqrt{1-\beta^2} = E/m_0c^2$, where E is the charged particle's total energy and m_0c^2 is the particle's rest-mass energy. Therefore, the energy threshold is

$$E_{th} = m_0c^2 \sqrt{1 + \frac{1}{n^2 - 1}}. \quad (\text{A.1})$$

Given the electron's rest-mass energy of 0.511 MeV, Eq. A.1 shows that the electron's energy threshold to produce the Čerenkov light is $E_{th}^e \approx 0.775$ MeV.

The number of photons, N_{PE} , produced per unit path length (dx) of a particle with charge ze and per unit energy interval (dE) of the photons is [146, page 1257]

$$\frac{d^2 N_{PE}}{dE dx} = \frac{\alpha z^2}{\hbar c} \sin^2 \theta_c, \quad (\text{A.2})$$

or, equivalently,

$$\frac{d^2 N_{PE}}{dx d\lambda} = \frac{2\pi\alpha z^2}{\lambda^2} \sin^2 \theta_c, \quad (\text{A.3})$$

where α is the fine structure constant ($\approx 1/137$), \hbar is the reduced Plank constant, c is the speed of light in vacuum, and λ is the photon wavelength. In practice, Eq. A.3 must be multiplied by the efficiency, ϵ_{coll} , for collecting the Čerenkov light (e.g., the portion of the photons sampled), the quantum efficiency, ϵ_{qe} , of the transducer (e.g., the PMT), and the probability, P , of the photons getting to the transducer (e.g., the portion of photons survived from the attenuation by the radiator), and integrated over the range in which $\beta n > 1$. Hence, the number of PEs per unit

path length detected in a given device is [146, page 1261]

$$\frac{dN_{\text{PE}}}{dx} = 2\pi\alpha z^2 \int \epsilon_{\text{coll}}(\lambda)\epsilon_{qe}(\lambda)P(\lambda)\frac{\sin^2\theta_c(\lambda)}{\lambda^2}d\lambda. \quad (\text{A.4})$$

The quantities $\epsilon_{\text{coll}}(\lambda)$, $\epsilon_{qe}(\lambda)$, $P(\lambda)$ and θ_c are all functions of the photon wavelength λ , although in typical detectors θ_c is nearly constant over the useful range of photocathode sensitivity.